


Doctoral Dissertation
Doctoral Program in Metrology (31st cycle)

Tailored fabrication of nanostructured substrates for surface-enhanced Raman spectroscopy applications

Eleonora Cara

* * * * * *

Supervisors
Dr. Luca Boarino, Istituto Nazionale di Ricerca Metrologica, Supervisor
Prof. Giuseppe Spoto, Università degli studi di Torino, Co-Supervisor

Politecnico di Torino
9th May 2019

I hereby declare that, the contents and organisation of this dissertation constitute my own original work and does not compromise in any way the rights of third parties, including those relating to the security of personal data.

.....

Eleonora Cara

Turin, 9th May 2019

Summary

Surface-enhanced Raman spectroscopy (SERS) is a vibrational spectroscopic technique providing selective information for sensing of chemical and biological species. It is based on the amplification of the Raman signals of molecules due to their interaction with the surface of plasmonic metals. Since SERS discovery, the morphology of the metallic substrate was recognised as a fundamental feature to provide a significant enhancement of the Raman signal. The modern advancement of the nanotechnologies has boosted the research activity on nanostructured substrates, pushing forward the hot spots engineering and the capabilities of SERS in ultrasensitive sensing and molecular identification. State-of-the-art 3D SERS substrates are commonly realised by means of conventional top-down nanolithography and etching techniques. These methods lead to adequate performances but are limited by time-consuming processes, high costs and low throughput.

In this dissertation, nanospheres lithography (NSL), a bottom-up technique, is exploited for the realisation of SERS substrates requiring regular plasmonic nanostructures produced over large area in a timewise manner and with affordable materials and methods. Particularly, NSL was employed in combination with a deep wet etching technique, metal-assisted chemical etching (MACE), for the realisation of gold-coated silicon nanowires (SiNWs) with hexagonally close-packed (HCP) symmetry. The high-aspect-ratio nanostructures exhibited high flexibility and the possibility to form bundles upon the evaporation of water. The location of the hot spots was found at the tip-to-tip sites of the leaning nanowires where probe molecules were adsorbed profiting from extremely high enhancement. Moreover, a quantitative analysis of the degree of order of HCP crystals of nanospheres in NSL was conducted in terms of the correlation length parameter ξ to optimise the distribution and density of the hot spots across the substrate.

The substrate with the highest long-range order (ξ larger than 1 µm), and correspondingly largest SERS enhancement, was found to display noteworthy homogeneity with inter-maps RSD of 8% evaluated over 600×600 µm^2. Moreover, the characterisation of SERS substrates relies on the evaluation of the enhancement factor (EF). However, its practical computation is often affected by a significant uncertainty in the determination of the number of molecules contributing to the SERS signal. Geometrical considerations are often used for such estimate, leading

to artificial variations of the EF of two orders of magnitude or more. A study of the EF was conducted to propose the use of synchrotron-based reference-free X-ray fluorescence for an accurate quantitative determination of the amount of analyte. The EF of the long-range ordered substrate was found equal to $(3.5 \pm 0.8) \cdot 10^4$. In addition, the gold-coated silicon nanowires SERS substrate showed promising results for its application to analytical chemistry. It was tested for the detection of melamine, a food contaminant, demonstrating high sensitivity with a limit of detection of 2.3×10^{-7} mg l^{-1} and limit of quantification of 1.3×10^{-5} mg l^{-1} in the picomolar range of analyte concentration.

Finally, in order to expand the fabrication protocol of SERS substrates based on NSL, a study on the directed self-assembly (DSA) of nanospheres was conducted. Employing topographical templates to confine the nanospheres allowed to overcome some intrinsic limitation of NSL, concerning the formation of domains with irregular shape, size and orientation. The correlated HCP domains of nanoparticles were extended to the area of tens of micrometres corresponding to the confining structures and distributed in patterns with regular shape and uniform orientation over square centimetres areas. This was especially observed in the linear templates with depth 0.6 times the spheres diameter, where 96.2 % of the domains were aligned to the template in the range $-10°$ - $10°$. The use of micrometre-sized templates exhibited remarkable results allowing to extend the use of NSL to a variety of advanced applications including biological, pharmaceutical and environmental analyses.

Part of the work reported in this dissertation has been previously published in references S. A. Kara, et al. *"Fabrication of Flexible Silicon Nanowires by Self-Assembled Metal-Assisted Chemical Etching for Surface-Enhanced Raman Spectroscopy"*; RSC Advances, 6, 96, 93649-93659 (2016) and E. Cara et al. *"Influence of the long-range ordering of gold-coated Si nanowires on SERS"*; Scientific Reports, 8, 1130 5 (2018).

Contents

Acknowledgements

The research activity discussed in this dissertation has received fundings from the EMPIR projects MetVBadBugs (15HLT01) and AeroMet (16ENV07). The activity carried out at PTB Berlin has been funded by the EMPIR Researcher Mobility Grant 16ENV07-RMG1. The EMPIR programme co-financed by the Participating States and from the European Union's Horizon 2020 research and innovation programme.

I would like to acknowledge several people who worked with me and enriched my activity in the past three years:

- my supervisor Luca Boarino, and ad honorem co-supervisor Natascia De Leo, for the continuous support in my scientific growth;
- their research group, especially Matteo Fretto, Giulia Aprile, Masoud Dialameh and Irdi Murataj for the interesting discussions and the time spent in the lab;
- my co-supervisor Giuseppe Spoto for his interest and advices;
- the group of Burkhard Beckhoff in PTB, especially Philipp Hönicke and Yves Kayser and the other researchers and PhD students, for hosting me and supporting my activity with their expertise;
- Luisa Mandrile and Andrea Giovannozzi for the essential and constructive collaboration;
- Federico Ferrarese Lupi for the invaluable guidance and active contribution to this research.

Last but not least, I would like to thank my loved ones who are always by my side and make me the person I am.

List of Figures and Tables

List of Symbols and Acronyms

Symbols

α	acceleration
$\Delta(\frac{1}{\lambda})$	Raman shift
Kα	fluorescence line corresponding to the electronic transition from the L shell to the K shell
Kβ	fluorescence line corresponding to the electronic transition from the M shell to the K shell
ν_0	frequency of the incident photon
ν_s	frequency of the scattered photon
$\Omega/4\pi$	solid angle of detection of the fluorescence signal
ω	rotational speed
$\overrightarrow{F}_\mathrm{c}$	capillary force
$\overrightarrow{F}_\mathrm{d}$	hydrodynamic force
θ	angle of incidence formed between the sample surface and the incident X-ray beam
θ_0	offset angle
E_0	energy of incident X-ray beam
f_0	photon flux of the incident X-ray beam
h	Planck constant
J_s	convective flux
LT	SDD detector lifetime

D diameter of the nanospheres

H depth of the template for directed self-assembly

Acronyms

AEF analytical enhancement factor

AFM atomic force microscopy

BCP block copolymers

DDA discrete-dipole approximation method

DFT discrete Fourier transform

DI deionised

DLS dynamic light scattering

DLW direct laser writing

DSA directed self-assembly

EBL electron beam lithography

EF enhancement factor

EtOH ethanol

FCC face-centred cubic / cubic close-packing

FCM four-crystal monochromator

FEG field emission gun

FIB focused ion beam

FTDT finite difference time domain simulation method

HCP hexagonal close-packing / hexagonally close-packed

IDL interactive data language

IPA isopropyl alcohol

LOD limit of detection

LOQ limit of quantification

LSP(R) localised surface plasmon (resonance)

MACE metal-assisted chemical etching

NIL nanoimprint lithography

NIR near-infrared range of the electromagnetic spectrum

NMI national metrology institute

NSL nanospheres lithography

NSs nanospheres

NTP nanotransfer printing

NWs nanowires

PMMA poly(methyl methacrylate)

PS polystyrene

RH6G rhodamine 6G

RIE reactive ion etching

RSD relative standard deviation

SDD silicon drift detector

SEM scanning electron microscope / microscopy

SERS surface-enhanced Raman spectroscopy/scattering

SI international system of units

SiNWs silicon nanowires

SSEF SERS substrate enhancement factor

TASA template-assisted self-assembly

UHV ultra high vacuum

VIS visible range of the electromagnetic spectrum

XRF X-ray fluorescence

Introduction

The Bureau International des Poids et Measure (BIPM), the most renowned institution of its field, provides a definition of metrology.

> Metrology is the science of measurement, embracing both experimental and theoretical determinations at any level of uncertainty in any field of science and technology.

A significant part of such vast science is devoted to the achievement of effective and reliable physical and chemical measurement methodologies, which ultimately affect the quality of life in our society. Several joint research projects are dedicated to establishing novel metrological capabilities relying on an interdisciplinary approach and collaborative effort of different scientific communities.

In this context, the project MetVBadBugs addresses the need for metrological methods to study antibiotic-resistant bacteria and biofilms using several analytical techniques. Vibrational spectroscopies, and surface-enhanced Raman spectroscopy (SERS) among the others, are identified as possible candidates to efficiently measure the quantitative drug uptake of bacteria. SERS is a powerful vibrational spectroscopy method in which the Raman signal of a molecule is enhanced given that its location is close to a plasmonic metal nanostructured surface. The role of the substrate is primary in supporting the plasmonic enhancement, for this reason, metrology requires it to provide significant enhancement with good homogeneity over large area. In order to comply with such requisites, the effort of research is dedicated to push forward the ability to realise plasmonic structures with customised nanoscale features.

The contribution to this project given by the research activity discussed in this dissertation is focused on the design and realisation of efficient and stable nanostructured plasmonic platforms for SERS. To this goal, the development and optimisation of nanofabrication protocols were performed exploiting alternative nanofabrication techniques. The selected techniques were nanospheres lithography (NSL), based on the self-assembly of polymeric colloidal particles over large area, and metal-assisted chemical etching (MACE), based on metal-catalysed electroless etching of silicon. The flexible high-aspect-ratio silicon nanostructures, realised with fine control over the size and long-range order and coated with gold to support the

plasmonic enhancement, were tested with different model molecules to select the most stable and reproducible configuration. The attachment of the bacteria and the SERS-based drug susceptibility test are still underway and therefore excluded from this dissertation.

One of the key areas of investigation concerned the morphology of the 3D nanostructures. In particular, the morphological properties were optimised to locate the hot spots of the Raman signal enhancement and guarantee the adsorption of the analyte in those areas. Moreover, the process of self-assembly was investigated to the benefit of the long-range order of the nanostructures and to increase the density and improve the distribution of the hot spots over large area for effective and reproducible performance. The effectiveness of the fabrication procedure was evaluated in terms of the substrate performance regarding the homogeneity and the enhancement factor of the substrate. A complementary method for the evaluation of the enhancement factor, based on synchrotron-based reference-free X-ray fluorescence, was proposed for the quantification of the molecules contributing to the SERS signal. An additional evaluation of the SERS substrate performance concerned the detection and quantification limits for a probe molecule often used as food contaminant.

This work has been carried out at the Italian national metrology institute (NMI), INRiM. The author belongs to the group of micro and nanofabrication of the Nanoscience and Materials department and was in charge of the realisation of the SERS substrates as well as the morphological characterisation. This work has been conducted in collaboration with the group of optical spectroscopy of the Quality of Life department in charge of conducting the SERS measurements. Some of the results presented in this dissertation has been obtained through measurements performed by the author at the German NMI, PTB, with the support of the group of X-ray spectrometry.

This thesis includes an introduction on surface-enhanced Raman spectroscopy with a phenomenological description of the basic physical principles in chapter 1, which comprises a discussion on the most relevant properties of this technique with particular emphasis on the role of the substrate. Chapter 2 puts an accent on the relevant contribution of novel nanofabrication methods for the development of cutting-edge substrates for SERS applications and introduces the substrate of choice, constituted of gold-coated silicon nanowires. Following this introductory discourse, the technical details of the materials and methods adopted for the fabrication of the substrate are presented in chapter 3 as well as the methods for the morphological characterisation by scanning electron microscopy and atom force microscopy. In the same chapter, the details about the SERS measurements and X-ray fluorescence measurements are given. Chapter 4 presents the results on the morphological aspects of the substrates, i.e. the flexibility property of the gold-coated

nanowires and their order, together with their effect of the intensity of SERS signals. The following chapter reports the characterisation of the homogeneity of the substrate as well as the calculation of the enhancement factor and the characterisation by X-ray fluorescence. Moreover, chapter 5 includes the determination of the limits of the substrate in analytical chemistry. The last chapter 6 regards the development of confinement structures to increase the order and coherence of the nanostructures. Final remarks are given at page 101. The list of figures and tables is displayed on page x and the list of symbols and abbreviations is included at page xiii.

Part I

Theory

Chapter 1

Surface-sensitive vibrational spectroscopy

This chapter is intended to provide an introduction on surface-enhanced Raman spectroscopy concerning the main features of this spectroscopic technique, including basic principles of the Raman effect in section 1.1.1 and the mechanism of the signal enhancement in section 1.1.2. The following section 1.2 is dedicated to an essential feature of SERS: the substrate as a supporting platform for the measurement. A first introduction on the requirements for the SERS substrates is given, followed by a classification of the different types of substrates in section 1.2.1. Section 1.2.2 provides a general introduction on the most common fabrication techniques for nanostructured substrates. In the conclusive section 1.2.3, a general overview of the crucial probe-substrate interaction is presented.

1.1 Fundamentals of SERS

Surface-enhanced Raman spectroscopy is a robust vibrational spectroscopic technique used for chemical and biological sensing. The name itself emphasises the cornerstone of this technique: the amplification of the Raman signal of molecules due to their interaction with the surface of plasmonic metals. In order to underline the optical effect behind this analytical technique, the final S in the acronym SERS can also stand for *scattering*. In 1928, C. V. Raman reported the experimental observation of the inelastic scattering of a photon by a molecule, due to the excitation or relaxation of the vibrational modes of the molecule [1]. Each probe molecule has different vibrational energies associated with its functional groups so that the Raman energy spectrum contains specific information on the molecule and it is called Raman fingerprint. Despite offering high specificity in molecular identification, the applicability of Raman spectroscopy is hindered by poor detection of the feeble Raman signals [2]. In 1977, D. L. Jeanmaire and R. P. Van Duyne reported

that the intensity of the Raman scattering can be greatly enhanced when the probe molecule is in close proximity to a roughened noble-metal electrode [3]. The signal amplification is ascribed to two factors, i.e. the electromagnetic enhancement and the chemical one, the first is widely accepted to give the predominant contribution. The electromagnetic field is largely intensified when localised surface plasmon (LSP) are excited at the rough nano-scale features on the noble metal surface, consequently the intensity of the inelastic scattering can be increased by many orders of magnitude [4].

In the last decades, the technological advancement in laser, Raman-related instrumentation and nanotechnology has boosted the research activity on SERS. Significant evidence of the power of this technique lies in the ability to identify chemical species and structural information in a broad range of fields, from materials science to biomedicine. SERS has been employed in ultrasensitive sensing, ranging from the detection of pesticides for food safety [5, 6, 7] to the detection of explosives for homeland security [8] and the study of DNA mutation [9] in biomedicine. Other applications include identification of pigment in art history [10, 11] or oxidation states of molecules in spectroelectrochemistry [12].

In a nutshell, surface-enhanced Raman spectroscopy combines the advantages of selective chemical information and the strong enhancement of the otherwise weak Raman signals. An overview of SERS cannot disregard the discussion of the features playing a major role in this analytical technique, namely the characteristic Raman signals of the probe molecules and the enhancement of the latter.

1.1.1 Basic principles of Raman spectroscopy

The interaction of light with molecules can occur either through absorption, emission or scattering events. Depending on the physical process of such interaction, several spectroscopic techniques have been studied and developed. Raman spectroscopy deals with the analysis of the energy spectrum generated by inelastic or super-elastic scattering processes between the incident photon and the probed molecule. In the particle framework, a scattering process involves the simultaneous absorption of an incident photon and re-emission of the photon with the same or shifted energy as sketched in figure 1.1(a). When the scattered photon has the same energy of the incident photon, as in the green arrow in figure 1.1(a), the scattering process is called elastic and it is referred to as Rayleigh scattering. In the case of inelastic or super-elastic scattering, the scattered photon can have either lower or higher energy than the incident photon as shown by the red and blue arrows in figure 1.1(a), respectively.

In Raman scattering, the transition corresponding to the excitation of the molecule from the vibrational ground state to the first excited state is called *Stokes process*; the energy of the scattered photon is lower than that of the incoming one $h\nu_s = h(\nu_0 - \nu')$ corresponding to the energy difference between the excited state

and the ground state. On the other hand, when the molecule relaxes from an excited vibrational state to the ground state, the scattered photon gains an energy $h\nu_s = h(\nu_0 + \nu')$ and the event is called *anti-Stokes process*. Figure 1.1(b) reports a simplified diagram of the vibrational energy states, the absorption of the incoming photon corresponds to an electronic transition to an excited virtual state and simultaneously a recombination corresponds to the emission of a photon whose energy depends on the kind of scattering process. If the incident photon has enough energy to excite the electrons in a real energy state, the scattering process is said to be *resonant* and the phenomenon is referred to as resonant Raman scattering.

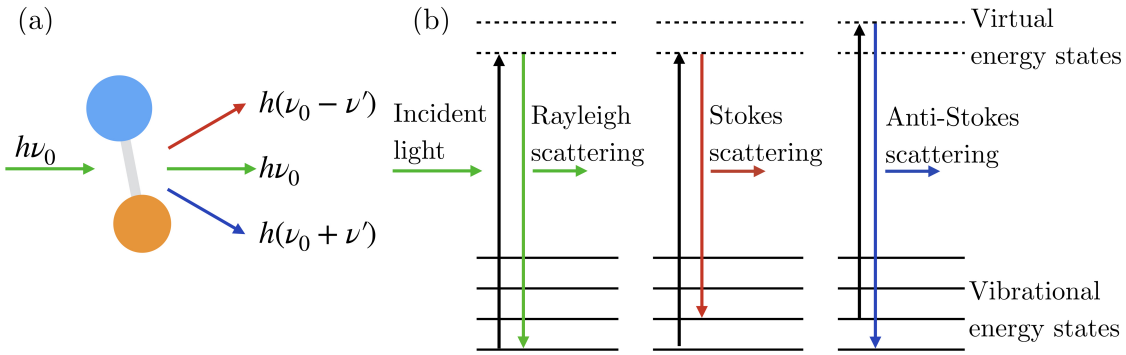

Figure 1.1: (a) Simple model molecule probed with an incident photon with energy $h\nu_0$. The scattered photon can either conserve the same energy in case of Rayleigh scattering or have lower or higher energy in case of Stokes and anti-Stokes scattering, respectively. (b) The transitions between the vibrational energy states are reported in the diagram for the elastic and inelastic scattering processes.

The energy lost or gained by the molecule is the difference between the excitation energy and the scattered light energy λ as $\Delta E = h(\nu_0 - \nu_s) = hc(\frac{1}{\lambda_0} - \frac{1}{\lambda_s}) = \Delta(\frac{1}{\lambda})$. The wavelength shift $\Delta(\frac{1}{\lambda})$ is referred to as *Raman shift* and it is positive for a Stokes process and negative for an anti-Stokes. It is conventionally indicated in wavenumbers (cm^{-1}), this makes the peaks positions in the spectrum independent from the excitation wavelength. The energy difference can appear as vibrational or rotational energy of the molecule and so the peaks position in the spectrum constitutes a unique *fingerprint* identifying the molecule. Figure 1.2 reports the Raman spectrum of ethanol as an example. The intensity of Rayleigh scattered light dominates the spectrum showing that the elastic scattering is the most probable scattering process, concerning inelastic scattering the anti-Stokes signal is much weaker than the Stokes scattering.

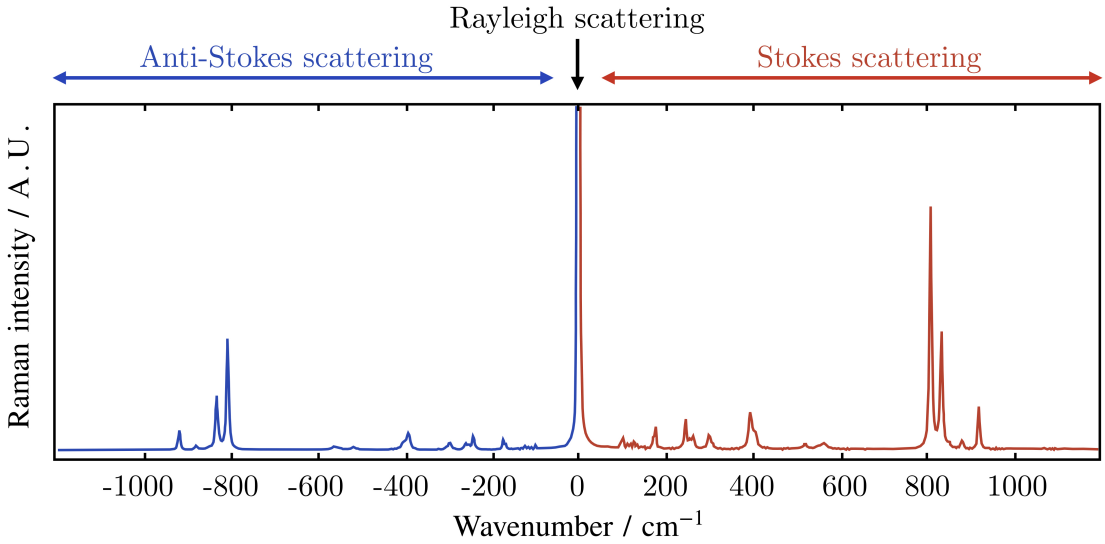

Figure 1.2: Raman spectrum of ethanol excited with incident light at 532 nm. The intensity of the Raman signal is displayed as a function of the Raman shift expressed as wavenumber in cm^{-1}. The negative Raman shift is referred to as anti-Stokes scattered light, while the positive axis is referred to more intense Stokes scattering. The largest percentage of the scattering occurs through an elastic process leading to an intense Rayleigh signal.

As well as the frequency shift, the intensity of the peak contains significant information regarding the Raman scattering occurring at the molecule. In the classical framework, when the molecule is placed in the electric field of the incoming electromagnetic wave, a separation of charges occurs which causes an induced electric dipole moment. The magnitude of such induced dipole moment $\overrightarrow{p} = \alpha \overrightarrow{E}$ depends on the applied field and on the polarisability of the molecule and it is modulated by the molecular vibrations [13]. The induced dipole vibrates at the frequency of the incoming wave but also at higher and lower frequencies dependent on the molecular vibration. The intensity of these side bands in the spectrum, i.e. Stokes and anti-Stokes bands, is proportional to the polarisability change of the molecule and varies for each vibrational mode. Other significant features of the Raman spectrum consist in the shape and broadening of the peaks, indicating inhomogeneity in the chemical composition or molecular chains length, or the shift from tabulated values, which may indicate stress in the molecular bonds.

The interpretation of the frequency spectrum relies on the assignment of the peaks to the vibrational modes of the probed molecule. The frequency of the Raman bands depends on the structure of the molecule and on its chemical groups; molecules with similar functional and chemical units tend to exhibit Raman bands in the same frequency range. Three main types of movements are usually considered in the assignment procedure of Raman peaks for a polyatomic molecule or functional

group, these are reported in figure 1.3 for a $=CH_2$ chemical group as an example. The vibrations include the stretching of the bond, which consists in the elongation and contraction of the bond between two neighbouring atoms in figure 1.3(a), the in-plane bending of the bond in figure 1.3(b), and the out-of-plane twist in figure 1.3(c). Moreover, in complex cyclic compounds, the so-called ring-breathing mode can also occur as shown in figure 1.3(d).

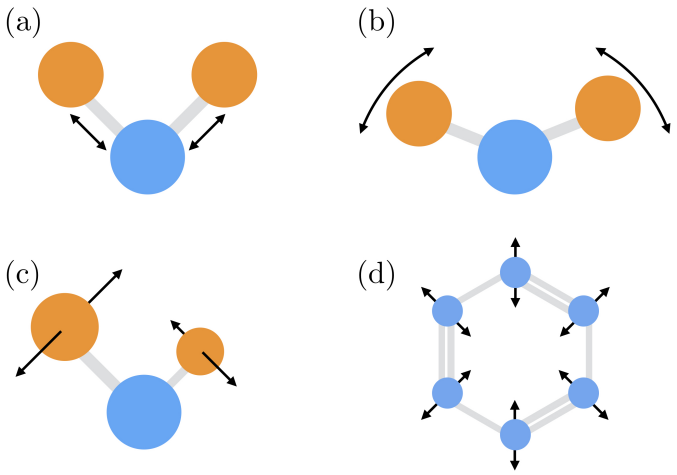

Figure 1.3: Common vibrational modes of a simple functional group ($=CH_2$) are (a) the stretching mode, (b) the in-plane bending mode, (c) the out-of-plane torsion or twist. In all of these modes, the atoms can either vibrate symmetrically or asymmetrically around their equilibrium position. An animated image of such movements is visible here. In case the molecule presents a ring, such as benzene (d), it can additionally exhibit the totally symmetric C−H stretch in the ring-breathing mode. An animated image of the ring-breathing mode is visible here.

1.1.2 Signal enhancement

The nature of the scattering processes is intrinsically feeble when compared with other optical phenomena, such as fluorescence and absorption. Despite the definition of the cross section for the vibrational modes is quite complex and requires much consideration, including the orientation of the molecules with respect to the incident field, typical values of the Raman scattering cross sections are estimated to be between 10^{-28} and 10^{-30} cm^2. Such values are about 14 orders of magnitude lower than fluorescence ones, estimated to be around 10^{-16} cm^2 [14, 15, 16]. Such weak signal and low detector sensitivity constitute a significant disadvantage of Raman spectroscopy which cannot be exploited advantageously for the detection of molecules in low concentration. In the seventies, an unexpectedly high Raman signal was detected from pyridine on a rough silver electrode [17] and in the following years the same effect was reported for many other molecules attached on different

rough metal surfaces or colloids in aqueous solution[18, 19] and it was proved to be related to a real intensification of the Raman scattering rather than by a larger number of molecules [3, 20].

The enhancement of the signal is traditionally attributed to two factors, displaying a chemical or an electromagnetic origin. The chemical enhancement effect has not been completely understood yet, it results from the adsorption of the molecule on the metallic surface. This interaction induces a modification of the electronic structure either by a charge transfer or a complex creation between the molecule and the surface. The consequent change in the polarisability of the molecule brings to a change in the Raman signal intensity. The electromagnetic effect is widely accepted to give the largest contribution to the enhancement. It can be obtained by exploiting the optical properties of nanostructured metallic surfaces through two different processes of interaction, schematised in figure 1.4 and described hereafter following references 21 and 22. The first process consists in the interaction of the incident beam with the metallic surface. The incoming field E_0 at frequency ν_0 undergoes a local enhancement resulting in $E_{\mathrm{loc}} = f_{\mathrm{loc}}(\nu_0)E_0$. A molecule close to the surface can be excited by the enhanced field E_{loc}; the scattered photon has shifted frequency ν_{s} and the amplitude of the detected signal is proportional to E_{loc} as $p = \alpha E_{\mathrm{loc}} = \alpha f_{\mathrm{loc}}(\nu_0)E_0$. The Raman signal is already enhanced compared to the case of a molecule far from a metallic nanoparticle. The second process involves the scattered photon at shifted frequency ν_{s} that interacts with the metal; the signal can be therefore enhanced in the so-called re-radiation process, $E_{\mathrm{rad}} = \alpha f_{\mathrm{loc}}(\nu_0) f_{\mathrm{rad}}(\nu_{\mathrm{s}})E_0$. In the electromagnetic effect, the Raman signal takes advantage from two enhancement factors at the excitation and Raman frequency, so that the SERS intensity can be calculated as $I_{\mathrm{SERS}} = f^2_{\mathrm{loc}}(\nu_0) f^2_{\mathrm{rad}}(\nu_{\mathrm{s}})I_0$ where $I_0 = \alpha^2 E_0$ is the intensity scattered by a molecule far from a metallic nanoparticle or surface. The product $F = f^2_{\mathrm{loc}}(\nu_0) f^2_{\mathrm{rad}}(\nu_{\mathrm{s}})$ is the total electromagnetic enhancement factor; when the incident and Raman frequency are close enough the two factors can be considered equal and the total enhancement is proportional to the local enhancement to the fourth power $F = f^4_{\mathrm{loc}}$.

The cause of the electromagnetic enhancement factor lies in the optical properties of metallic nanoparticles, as a matter of fact the conduction electrons undergo collective oscillations, called surface plasmons, which are confined in the nanofeatures of the metal and are referred to as *localised surface plasmons* (LSP), see figure 1.5 for an illustration of the LSP. Depending on the shape, size, material, and dielectric environment of the metallic nanoparticles, the maximum absorption in the visible (VIS) range occurs at a different frequency. When the excitation occurs at the maximum absorption frequency, the driven oscillation response is particularly intense and a localised surface plasmon *resonance* (LSPR) is observed [23].

Localised surface plasmons occur in metallic nanoparticles or nanostructures with dimension in the range from 10 nm to 200 nm and result in the amplification of the electric field near the particle surface. The decay length of LSP is generally of

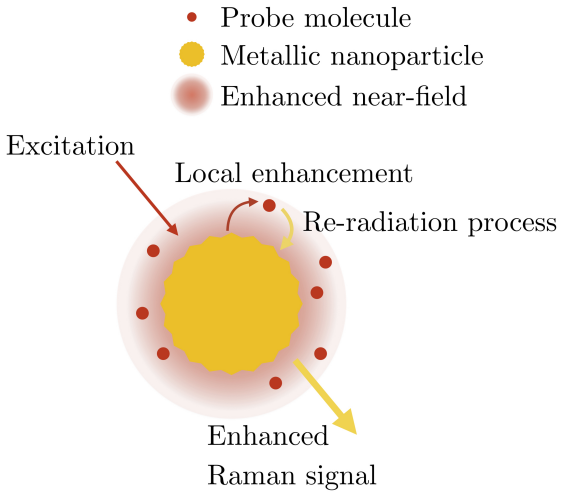

Figure 1.4: Basic principle of the electromagnetic enhancement effect. Figure adapted from reference 21.

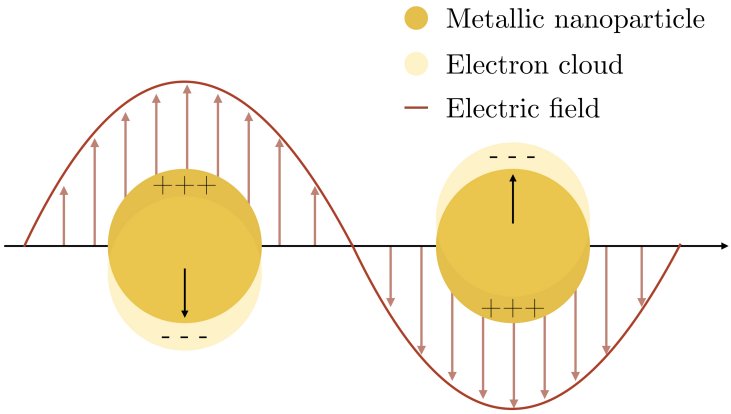

Figure 1.5: Schematic illustration of the plasmon oscillations in metal nanoparticles under the excitation of the incoming electric field. The displacement of the conduction electrons cloud relative to the nuclei is displayed.

the order of tens of nanometres and depends on the specific size and geometry of the nanostructure. As a consequence, the enhancement effect is extremely localised to the surroundings of the nanoparticles and the intensity of the SERS signal decreases exponentially in the first few nanometres from the surface of the metal. The analyte must be located within $\sim$ 10 nm in most cases, this is achieved either through physisorption or chemisorption, i.e. formation of a chemical bond with the metal, on the surface. The local enhancement also depends on the charges confinement in elongated structures and on the coupling effects among nanoparticles under specific close separation conditions [22].

It is clear that the morphology of the metallic structures, constituting the SERS

substrate, plays a crucial role in SERS to support a strong plasmonic enhancement. Particularly, the presence of localised regions, such as gaps of a few nanometres found in between plasmonic objects, produces extremely large local field enhancement and electromagnetic SERS enhancement, which has been theoretically predicted to reach values as high as 10^{12} [24]. Such confined areas are called *hot spots* and they account for the largest enhancement of the Raman signal across the substrate. The distribution of hot spots across the SERS substrate can cause the enhancement to vary drastically from point to point, this is taken into account in the definition of the SERS EF that indicates the enhancement obtained with respect to the non-SERS conditions.

The experimental estimation of the enhancement factor (EF) constitutes a central aspect for the characterisation of the SERS effect. The necessity to standardise SERS technique and to compare different substrates justify the attention that has been dedicated to the subject of the EF over the years to obtain a rigorous definition and practical calculation method [25]. A simple definition of the EF, particularly relevant for analytical chemistry, is reported in the equation 1.1:

$$\mathrm{AEF} = \frac{I_{\mathrm{SERS}}/c_{\mathrm{SERS}}}{I_{\mathrm{RS}}/c_{\mathrm{RS}}}, \tag{1.1}$$

where the intensity of the Raman signal I_{RS} is measured for a given concentration of the analyte c_{RS}, under identical experimental conditions the SERS signal I_{SERS} is measured for the same analyte at the concentration c_{SERS}. The analytical enhancement factor (AEF) in such definition can be improved by taking into account that SERS is a surface spectroscopy, thus only the adsorbed molecules contribute to the signal, and that the enhancement magnitude depends on the distance between the molecule and the metal. The adsorption properties of the substrate and the surface coverage can be considered by correcting the measured intensity with the number of molecules contributing to the signal to obtain the EF:

$$\mathrm{EF} = \frac{I_{\mathrm{SERS}}/N_{\mathrm{surf}}}{I_{\mathrm{RS}}/N_{\mathrm{vol}}}. \tag{1.2}$$

Equation 1.2 reports the average enhancement factor calculated across the substrate, where $N_{\mathrm{vol}} = c_{\mathrm{RS}}V$ is the average number of molecules in the scattering volume V for Raman measurement. The use of equation 1.2 requires to have a monolayer coverage, so that N_{surf} is the number of molecules adsorbed on the surface inside the scattering volume for SERS experiments. The SERS substrate enhancement factor could also be defined in equation 1.3:

$$\mathrm{SSEF} = \frac{I_{\mathrm{SERS}}/\mu_{\mathrm{M}}\mu_{\mathrm{S}}A_{\mathrm{M}}}{I_{\mathrm{RS}}/c_{\mathrm{RS}}H_{\mathrm{eff}}}. \tag{1.3}$$

The number of molecules $N_{\text{surf}} = \mu_{\text{M}}\mu_{\text{S}}A_{\text{M}}A_{\text{eff}}$ and $N_{\text{vol}} = c_{\text{RS}}H_{\text{eff}}A_{\text{eff}}$ both contain the effective surface area of the scattering volume, which is irrelevant to the final result. The term μ_{M} is the density of single nanostructures, A_{M} is the metallic surface area in each one, μ_{S} is the surface density of the molecules on the metal, while c_{RS} is the concentration of the solution used for the normal Raman measurement and H_{eff} is the effective height of the scattering volume.

The practical calculation of the EF requires a careful evaluation of the non-SERS conditions and of the many factors that influence the EF, including the properties of the laser excitation and the detection as well as the intrinsic properties of the analyte, the surface adsorption properties and the substrate characteristics [26]. In both EF and SSEF it is crucial to have an accurate estimate of the surface density of the analytes and metallic coverage surface area.

1.2 Detection platform for SERS

The detection of the molecular Raman fingerprint of the analyte depends on the SERS substrate, in terms of morphology and molecule-metal interaction. This measurement platform plays a pivotal role in facilitating the molecular sensing through signal enhancement. With regards to this goal, the criteria that identify an ideal substrate for sensing applications [27] can be detailed as the following:

- strong enhancement, and thus high sensitivity;
- uniformity of the enhancement across the substrate;
- reproducibility among different substrates;
- robustness of the structures.

The fulfillment of all such requirements in a single substrate is an ongoing challenge, as a matter of fact a substantial part of literature reporting on SERS is dedicated to the development of efficient substrates [28, 29, 30, 31]. Since the gain in the Raman signals intensity and increased sensitivity are the fundamental premises of SERS, the first characteristic associated with the SERS substrate is the capability to produce a large enhancement. The most intense amplification on a substrate is found in the presence of hot spots, but strong discrepancies in the enhancement can arise among these regions and other locations characterised by a weaker near-field intensity. Therefore, many times the substrates present a complementarity between enhancement and uniformity, the ones with the largest enhancement exhibit poor uniformity and vice-versa [32]. The fabrication of SERS substrates has been often addressed to finding a trade-off between these two features. In this framework, the dramatic expansion of nanotechnologies and related techniques has promoted the advancement of SERS through the development of substrates with more and more controllable features.

1.2.1 From one to three-dimensional structures

In order to obtain large local field enhancement, it is desirable to have a metallic surface showing strongly localised plasmons [33]. The most common metals employed in SERS substrate are gold, silver, and copper, because they have their plasmon resonance frequencies in the VIS and near-infrared (NIR) range ($\sim$ 400 nm to 1000 nm), where most of Raman measurements occur, and they are highly conductive [34]. Particularly, gold and silver are widely used because they combine good enhancement and significant chemical stability in air [35]. Aluminium has also been used as plasmonic metal with intense enhancement in the NIR-VIS range [36, 37, 38]. Despite the plasmonic metal, a large number of substrates has been proposed as possible support for SERS measurement; the metallic substrates can be classified by their morphologies in three categories:

- 1D substrates as nanoparticles and colloids;
- 2D substrates as roughened electrodes or nanoporous surfaces;
- 3D substrates as nanostructures fabricated on a solid substrate.

Historically, the substrates that contributed to the discovery and early development of SERS were roughened electrodes [17, 39, 40].Analogously, nano and mesoporous silicon substrates have been reported quite recently as possible SERS active supports [41, 42, 43, 44]. The class of substrates constituted of metallic nanoparticles occupies a preeminent place in the early and recent progress of SERS [45]; metallic colloids are some of the most used substrates for their versatility and simple preparation by chemical methods, as they can be used in suspension to trace molecules in liquid or they can be deposited on a solid substrate. Moreover, they come in several shapes ranging from nanospheres and nanotriangles to nanostars and nanorods [46, 47], and can be optimised to produce large enhancement up to single molecule detection [48, 49, 50]. Often times the formation of aggregates of plasmonic particles is promoted, by chemical functionalisation of the colloids, to efficiently produce electromagnetic hot spots where interparticle distances are of the order of a few nanometres [51]. However, the use of colloidal solutions has some drawbacks concerning the uniformity and reproducibility of the enhancement, due to the random aggregation of the nanoparticles and to broad size distribution, and the stability of the substrate [52]. Figure 1.6(a) shows a sketch of plasmonic colloids in solution, while figure 1.6(b) displays a possible geometry of 3D nanostructures on a solid substrate.

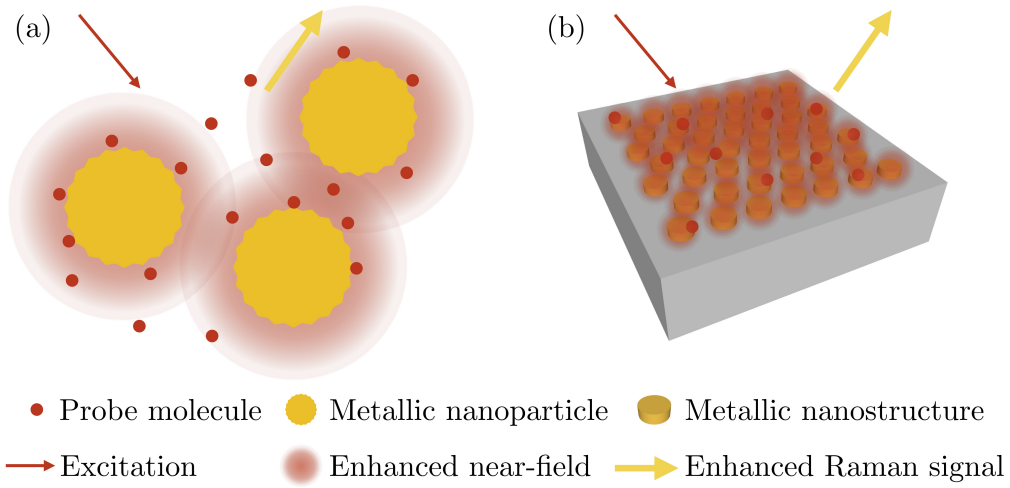

Figure 1.6: This scheme represents some of the possible substrates for SERS: (a) 1D substrate constituted of plasmonic nanoparticles in solution and (b) 3D substrate constituted of nanostructured plasmonic metals on a rigid support. Figure adapted from reference 21.

A multitude of different three-dimensional morphologies and geometries has been produced throughout the last decades, such as periodic arrays of metallic particles on a solid substrate or regular nanoholes and nanopillars [28]. Very well-known commercial substrates for SERS are constituted of regular arrays of inverted square pyramids evaporated with gold. The square base is designed by optical lithography on a resist mask and the underlying silicon is etched anisotropically by KOH, which attacks silicon in the <100> plane producing characteristic V-etched sidewalls. This substrate offers high reproducible SERS performance and constitutes a good platform for those applications that do not require significantly high EF. The fabrication of 3D nanostructures has been pursued with many physical micro and nanolithographic techniques combined with each other and through chemical growth methods as well [53].

1.2.2 Conventional nanofabrication of SERS substrates

The relationship between SERS and nanofabrication is evident because SERS depends strongly on nanostructured features and nanofabrication can produce optimised architectures to maximise the enhancement with reproducible outcomes. As mentioned in section 1.2.1, several physical methods have been adopted for nanofabrication; a significant class of lithographic methods is given by the *top-down* techniques, such as optical lithography, either with shadow mask or by direct laser-writing (DLW), electron beam lithography (EBL), and nanoimprint lithography (NIL) for direct patterning onto a solid support.

One of the most widely used methods is EBL, a direct writing (maskless) method that enables accurate control over the geometrical parameters of periodic metallic features with a sub-10 nm resolution and the realisation of any shape, such as triangular, circular, square or linear patterns. Moreover, it provides the possibility to design nanoscale patterns optimised for the frequency of Raman laser source [54]. Several works have been devoted to studying the contribution of different sizes and gaps among the metallic patterned regions on the SERS perfomance of the substrates prepared by EBL [55, 56]. Furthermore, this technique has been combined with complementary processes, such as reactive ion etching (RIE) [57, 58] to obtain nanopillars and nanoporous structures or angle evaporation technique [56] for a variety of nanostructures or coating features. Despite its outstanding resolution, this technique has some shortcomings related to the cost of the instrumentation and implementation as well as the incompatibility of sequential processing methods with lithographic patterning over large area even though some time-optimisation procedures have been applied [59].

The combination of EBL to parallel lithographic techniques, such as NIL and nanotransfer printing (NTP), constitutes a way to partly overcome the time-related drawbacks of this method. For example, a stamp with periodic arrays of square structures has been prepared by EBL and coated via physical vapour deposition, with the possibility to use it many times to transfer the pattern of metallic squares onto polymeric supports to create a nanocomposite substrate for SERS [60]. Similarly, nanoimprint lithography has been employed to produce a series of replicas from a nanopatterned mold [61, 62]. These parallel lithography methods can be paired with other nanopatterning methods to obtain nanostructured features over large area with regards to costs and process time. However, NIL and NTP present some issues in the production of structures with high aspect ratios due to adhesion on the template and need for anti-sticking coatings.

Another versatile technique to shape 3D structures without the employment of a mask is the focused ion beam (FIB). It has been used to fabricate complex arrays of elliptical nanostructures on silicon coated with gold [63]. This sequential writing technique presents limitations similar to EBL in achieving acceptable throughputs of square centimetre area for application with contained costs.

Electron beam lithography and the other reported traditional top-down lithographic approaches offer an excellent level of control on the geometrical parameters of the nanostructures organised in regular arrays to increase the enhancement and the uniformity as well as the reproducibility. These techniques give access to a considerable assortment of shapes, sizes and features in combination with etching and sculpting techniques, such as RIE or FIB, or parallel writing techniques in the field of soft lithography, such as NIL. However, the major drawbacks of such methods are related to the time-consuming and expensive implementation so that significant obstacles remain especially concerning patterning over large-area which is required for sensing applications.

Other than the top-down approach discussed above, *bottom-up* methods constitute another class of lithographic techniques. These have been largely utilised and combined with other processes for the realisation of several plasmonic nanostructures and, in consideration of their relevance for SERS and for this dissertation, they will be treated in depth in chapter 2.

1.2.3 Probe and substrate

Alongside with the choice of a suitable enhancing substrate and fabrication method, the preparation of SERS experiments include some conditions regarding the molecular species to be detected. In the first place, the probe molecule for SERS is required to have intrinsic Raman properties, i.e. a good Raman cross-section. As a rule of thumb, if a molecule does not present any symmetry group then all its mode will be Raman active; in general, Raman modes correspond to a distortion of the electronic cloud of the molecule and so in a large polarisability change. Compounds with Raman-active modes which can have their signal enhanced through SERS effect include aromatic amines, phenols, compounds containing oxygen and carboxylic acids; common molecules are the rhodamine 6G (RH6G), pyrimethanil, 4-mercaptopyridine, and 4-aminothiophenol, among others.

In addition, a good level of compatibility between the analyte and the substrate is required; the molecule must be bonded or adsorbed on the surface in the interest of exploiting the plasmonic enhancement of the Raman signals which occurs at a length scale of a few nanometres. Many molecular species and functional groups display strong a chemical affinity to the most widely used plasmonic metals, i.e. gold and silver. As a matter of fact, many analytes can be physisorbed on the surface of gold and molecules containing a thiol group ($-$SH) form a covalent bond with Au atoms on the surface [35]. In some other cases, there is no affinity between the molecule and the metal so that the functionalisation of the surface through chemical manipulation is requested. For example, the detection of biomarkers in immunoassay applications demands the metallic surface to be coated with antibodies to facilitate their capture on the surface [64]. In some other cases, analyte engineering is preferred; for example, many molecules can be attached to functional groups that can effectively bind to the metal surface or exclusive bond can be obtained by functionalising the metallic surface and the molecule with complementary groups, such as DNA strands.

A further important aspect to take into account is the fact that, since the electromagnetic enhancement is extremely localised near the surface of the plasmonic metal, the most efficient adsorption configuration consists in a monolayer of molecules directly adsorbed on the surface. The presence of multiple layers of analyte reduces the number of excitation photons that reach the molecule-metal interface leading to a decrease of the detected signal intensity. The step of the molecule deposition is particularly important to guarantee a significant interaction

between the probe molecule and the plasmonic metal. When dealing with a solid substrate, the deposition of the molecule from a liquid solution is particularly delicate. Several methods can be chosen for the deposition. The most common ones are spin coating of the probe solution on the substrate, drop casting a small volume of the solution in specific locations on the surface or incubating the substrate inside the liquid solution [65].

Chapter 2

Large-area fabrication of 3D substrates

This chapter serves as an introduction on the fabrication technique under study in this dissertation, nanospheres lithography, and on the strategy proposed for the realisation of ordered nanostructures tested as substrates for SERS analysis. In section 2.1, the bottom-up approach to nanofabrication is presented with particular emphasis on the mechanism of self-assembly of colloids in section 2.1.1 and nanospheres lithography in section 2.1.2. The subsequent section 2.2 is dedicated to the class of SERS substrates based on the assembly of 3D nanostructures for the generation of hot spots. The adopted strategy of fabrication is discussed in the same section. Section 2.3.1 constitutes an introduction to high-aspect-ratio anisotropic etching by metal-assisted chemical etching used for the realisation of the SERS substrates. The mechanism of etching and mass transport are discussed. The final subsection 2.3.2 is dedicated to a brief description of the overall fabrication protocol.

2.1 Bottom-up approach to nanofabrication

The development of alternative repeatable fabrication protocols is an important part of research on SERS and it is mandatory to obtain substrates with a large number of regularly distributed hot spots in a timewise manner and with affordable materials and methods. An increasingly popular solution is the bottom-up approach. In general terms, bottom-up lithographic methods are based on the *self-assembly* of macromolecular units with dimensions down to 10 nm into regular arrays over square centimetres area. Common self-assembling building blocks are block copolymers (BCP) used in BCP lithography for the realisation of complex arrangements at the nanoscale displaying different morphologies, such as cylindrical, fingerprint-like, lamellar and gyroidal structures [66]. Spherical nanoparticles

are also employed as building blocks in nanospheres lithography to produce arrays of planar or three-dimensional structures. The potential of NSL for SERS rapidly emerged for its versatility, low cost and high throughput nanofabrication over large area.

2.1.1 Self-assembly of colloids on substrates

The self-assembly is the spontaneous formation of organised structures in an ordered state of thermodynamic equilibrium[1] starting from a disordered system of pre-existing components through a stochastic process [68]. The ubiquitous presence of self-assembly in chemistry, physics of soft condensed matter, nanotechnology and biology underlines the vast opportunities related to its exploitation [69]. Common building blocks in bottom-up lithographic methods are block copolymers, molecules or segments of macromolecules and colloidal particles.

Colloidal particles are not only defined by their size, which is usually comprised in the range between 1 nm and 1 µm, but especially by their behaviour when dispersed in a solvent; their dynamics in equilibrium is governed by the Brownian motion, while the effect of gravity can be neglected. During the course of their random motion, colloidal nanoparticles collide and undergo a series of interactions. These inter-colloidal interactions in dispersion are described by keeping into account the presence of the solvent which mediates the forces. The interactions are fundamentally electrostatic in origin and are related to the surface charges carried by the particles. However, compensating counter charges are present in the solvent and the resulting Coulomb force is not simply repulsive, even in the apparently straightforward situation of two like-charged particles. Its nature is compensated by the free ions in the medium forming a screen layer around the particles. Moreover, the colloidal particles undergo hard-core repulsions due to the fact that they have a well-defined size and shape and behave like solid bodies not able to interpenetrate. On the other hand, attractive van der Waals interactions occur among the colloids and can cause aggregation. An exhaustive discussion of the forces between colloids in dispersion can be found in reference 70.

The balance of the attractive and repulsive interactions among the colloidal particles allows them to reach the equilibrium separation; this interplay of forces is the foundation of the self-assembly. The mechanism underlying the self-assembly process of monodispersions of NSs in two-dimensional crystals is quite complex. It can be exploited in several conditions and, depending on the crystallisation conditions, different driving forces may arise and dominate the process. The most

[1] In literature, the term self-assembly is often used interchangeably to the term self-organisation [67, 2]. However, it is worth noting that, while the term self-assembly is referred to a process leading to a state of equilibrium, self-organisation is often used in complex systems science in the description of non-equilibrium processes.

common configurations for self-assembly are found at liquid-gas interfaces where attractive long-range interactions guide the ordering process, in the presence of electric fields via electrophoretic deposition on the surface of a solid electrode and in a thin film of liquid on a solid substrate where attractive capillary forces arise. The work discussed in this dissertation regards the self-assembly of colloids in a thin-liquid film on a rigid substrate; the mechanism of self-assembly was described in depth by N. D. Denkov and K. Nagayama et al. [71, 72]. Their observations suggested a two-stage mechanism of the 2D crystallisation: the formation of a nucleus of nanoparticles partially immersed in the wetting film driven by attractive capillary forces and the subsequent growth of the crystal through the convective flux of particles towards the area of liquid evaporation in the nucleus.

At first, the nanoparticles are immersed in a liquid film whose thickness exceeds the diameter of the nanoparticles, leaving them to float in Brownian motion and the vast range of interaction introduced so far. An illustration of this situation is depicted in figure 2.1(a). The progressive evaporation results in the thinning of the wetting film and in the formation of menisci in between the nanoparticles. This configuration leads to the onset of attractive capillary forces $\overrightarrow{F}_{\mathrm{c}}$ starting the formation of an ordered cluster of particles partially immersed in the liquid layer [73]. These forces are indicated by the orange arrows in figure 2.1(b). Inside the thin wetting film on the rigid substrate, the particles are confined to move in a 2D space driven by a convective flux of the solvent J_{s}, which compensates the continuous evaporation in the cluster regions with thinner solvent layer. In figure 2.1(b) the flux is displayed by a dark-blue arrow and it causes a hydrodynamic force (light-blue arrow) that drags the particles towards the array under formation.

The lattice of nanoparticles forming under the action of the capillary forces has a hexagonal close-packing (HCP) symmetry. The self-assembly of equal spheres occurs in a way to seek the most favourable energetic configuration by maximising the contact with neighbours [74]. As a matter of fact, the HCP symmetry constitutes the arrangement of equally sized spheres providing the largest packing density, together with the cubic close-packing or face-centred cubic (FCC) symmetry. As stated by the mathematical theorem known as Kepler conjecture[2], the density of these arrangements is around 74%. As an example, figure 2.2 reports a scanning electron microscope (SEM) image of colloidal spheres ($d = 617\,\mathrm{nm}$) arranged in a double layer displaying both the FCC and HCP symmetries on the left and right, respectively.

[2]The conjecture proposed by Johannes Kepler in 1611 states that close packing, either cubic or hexagonal, constitute the densest possible sphere configurations among possible regular and irregular arrangements. Several mathematicians attempted to prove the theorem but failed throughout the years. After four centuries the mathematical proof was proposed by Hales in 1998 and in 2017 the correctness of his proof was confirmed at last [75].

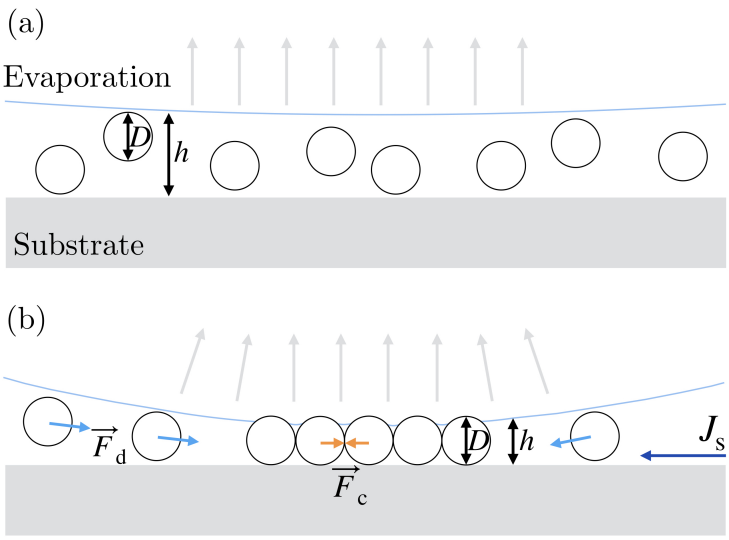

Figure 2.1: (a) The nanospheres layer undergo Brownian motion when they are immersed in a liquid layer with thickness h larger than the particle size D. (b) The continuous evaporation reduces the wetting film to a thickness comparable to D. In this environment, the formation of an ordered nucleus is ascribable to the onset of capillary forces $\vec{F}_c$ between the particles indicated by the orange arrows. The light-blue arrows indicate the hydrodynamic forces $\vec{F}_d$ that drive the nanoparticles to the ordered region. These are caused by the solvent convective flux J_s indicated by the dark-blue arrow.

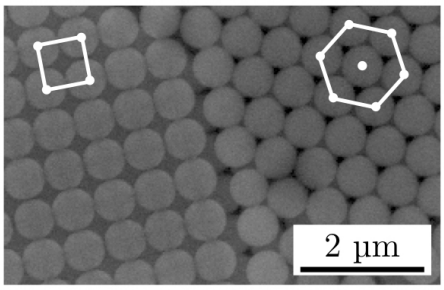

Figure 2.2: SEM image showing the two most dense arrangements of equal spheres: FCC and HCP on the left and right, respectively.

2.1.2 Nanospheres lithography

Nanospheres lithography, also known as *colloidal* or *natural lithography*, is based on the self-assembly of spherical colloids leading to the formation of single or double-layered matrixes exhibiting HCP symmetry, as shown in figure 2.3(a) and figure 2.3(b). The colloidal crystal shields the metal deposition and its removal produces

periodic arrays of metallic nanostructures, either nanotriangles in figure 2.3(c) or nanodots in figure 2.3(d), thanks to the deposition of metal through the interstices among the ordered NSs. The colloidal suspension with narrow size distribution can be chosen to control the size, shape, and spacing of the resulting metallic nanostructures arrays.

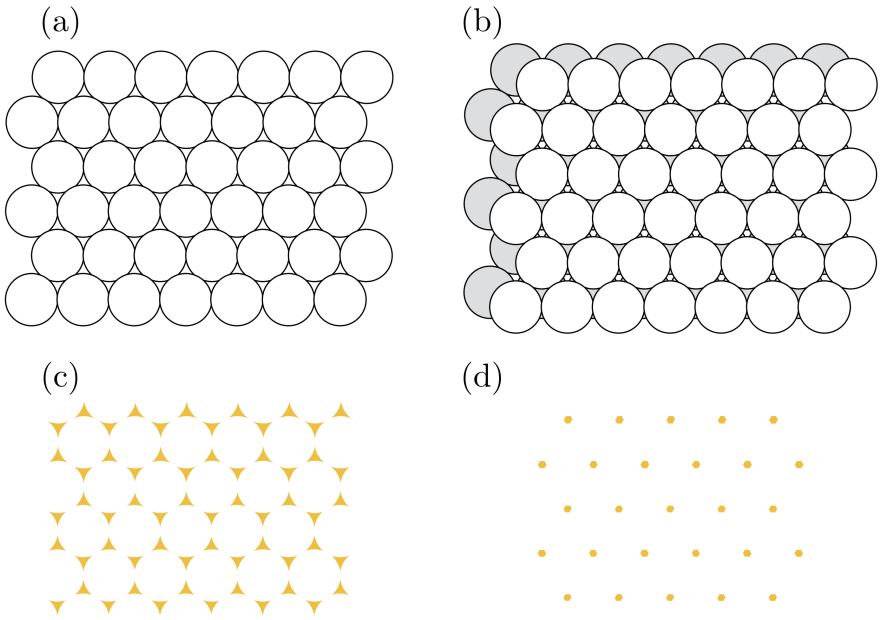

Figure 2.3: (a) Monolayer and (b) double layer of polymeric colloids arranged in HCP configuration, used as lithographic mask to realise periodic arrays of metallic (c) nanotriangles and (d) nanodots, respectively.

The knowledge on the mechanism of self-assembly and the consideration that the rate of the solvent evaporation influences the ordering process and thus the quality of the array of NSs [71] promoted the development of several methods to control the first and most delicate phase of NSL, the deposition of the nanoparticles.

A common method is the Langmuir-Blodgett coating which consists in transferring a monolayer of NSs formed at a liquid-gas interface onto a solid substrate through controlled substrate withdrawal. The monolayer formation requires the use of surfactants to enhance the hydrophobicity of nanospheres. The nanospheres are compressed by a barrier in order to organise in a 2D colloidal crystal on the liquid surface. This procedure allows to control the number of layers and the packing density and to pattern macroscopic areas with possible extension to flexible substrates with the roll-to-roll Langmuir-Blodgett technique [76]. Floating monolayers can also be deposited on a substrate immersed in the liquid until it naturally evaporates [77]. A simplified version of Langmuir-Blodgett is the dip-coating in which the evaporation rate and the withdrawal speed are tuned to achieve large 2D crystals in

which a precise particle distribution is not required [78]. The most simple way is to deposit a drop of NSs suspension on a rigid substrate and let it evaporate. Colloidal monolayers have been prepared by controlling the temperature and the humidity of the system [79, 80]. To allow the suspension to spread all over the surface, the substrate can be tilted at a certain angle or moved in circular motion [81], however, this method offers low control on the self-assembly outcome. It is possible to accelerate and control the evaporation rate of the solvent by depositing the suspension by *spin coating*. This method consists in the deposition of a drop of colloidal suspension on the substrate which is then accelerated to a certain rotational speed so that the suspension is uniformly spread on the surface and the solvent evaporates leading to the self-assembly of the colloids [67]. The spinning deposition is quite versatile for the possibility to change the acceleration, speed, and duration of the process and it is well established in industrial lithographic processes. Another valid technique is the doctor blade in which the convective transport of the colloidal suspension and its evaporation rate are controlled by sliding a thin spreading blade above the substrate at a fixed distance and velocity [82, 83].

The adjective 'versatile' is recurring in the description of NSL; this is due not only to the variety of available techniques for the deposition of the colloids but also to the possibility to customise the fabrication, in terms of the choice of the substrate material and pre-treatment, the NSs materials, surface functionalisation, and size. The most common substrate materials used for the self-assembly of colloidal spheres are silicon, mica and glass [73], indium tin oxide (ITO) glass is also used when a conductive substrate is needed [84]. The particles material is usually selected between silica (SiO_2), poly(methyl methacrylate) (PMMA) and polystyrene (PS). Additionally, the colloidal particles are synthesised in a broad range of sizes ranging from tens of nanometres to 1 µm. The particles are often dispersed in water to be deposited on the substrate and an important parameter of such colloidal suspension is the so-called dispersity, namely the index measuring the heterogeneity of sizes of particles in a mixture. The realisation of regular patterns of NSs relies on the use of a *monodisperse* suspension.

Furthermore, the adaptability of NSL translates into the realisation of several geometries in different fabrication protocols involving both bottom-up and top-down methods for an abundance of applications. Monolayers of NSs have been employed for the fabrication of nanostructures for vacuum micro and nanoelectronic devices [85], graphene nanomeshes on patterned Cu foils [86] and Co/Pt nanodisks for magnetic memory devices [87] as well as macroporous nanoparticles film for catalysis and membranes [88]. Moreover, arrayed colloidal particles have been used for applications in drug delivery [89], biosensors and optoelectronic devices [90]. Furthermore, the realisation of metallic nanodisks has been achieved with NSL by depositing the nanospheres directly on a metallic coated substrate and by adding an RIE or ion milling step to etch the surrounding areas to each nanosphere [91].

Bilayers of NSs are also employed in the so-called Moiré-NSL for sequential layer stacking leading to the formation of unorthodox nanopatterns, the Moiré patterns, used for image processing and refractive index sensing [92]. Multi-layered colloidal crystals constitute an interesting product of NSL as well, both silica and polystyrene beads have been used for the realisation of opaline structures and photonic crystals [93, 94, 95].

2.1.3 Nanospheres lithography for SERS substrates

Since Deckman and Dunsmuir pioneered natural lithography, in which a monolayer of colloidal particles was used to define a large-area lithographic mask [96], and Van Duyne et al. developed what now is known as nanospheres lithography [97], the technique gained popularity for the fabrication of periodic arrays of metallic nanostructures. The broad choice of nanoparticles materials and sizes for this technique allowed to achieve tunable geometrical parameters with different material properties and to study the size-dependent chemophysical properties of the nanostructures. Particularly, the optical properties were recognised to hold distinctive importance in the field of plasmonics and SERS so that this technique emerged as an appropriate choice for substrate fabrication [98, 99].

Historically, nanotriangles and nanodots are the first geometries produced by NSL and by far the most common type of structures used for SERS. Notable studies of the tunability of the position of LSP resonant frequency were performed by modifying the in-plane and out-of-plane dimensions of the metallic nanostructures and their reciprocal distance, by selecting spheres with different diameters and changing the thickness of the deposited metal [100]. So that these nanostructures can be coupled to different excitation wavelengths. The highest calculated enhancement occurs at the tips of the nanotriangles; the detection of several analyte species is possible down to single molecule sensitivity as described in reference 29. A novel photonic-plasmonic composite substrate was recently proposed by Zahn et al. by building the triangular nanostructures obtained by NSL on top of a porous silicon Bragg reflector, this coupling provides a new way to amplify the optical response of the plasmonic resonances [31].

By matching NSL to angle-resolved deposition, which consists in the metal deposition with non-zero incident angle with respect to the normal direction of the substrate, isosceles nanotriangles for plasmonic enhancement have been obtained by Haynes and coworkers using an evaporation angle from 0° to 45° [101]. A slightly more complex variation of the angle-resolved deposition with an incidence angle of 15° was applied to produce gold and silver heterogeneous binary nanostructures [102].

Simple employment of the NSs monolayer for SERS detection consist in coating the polymeric nanoparticles with a metallic thin film to obtain a film over

nanosphere (FON) surface. Ag FON surfaces have been reported as robust plasmonic materials for SERS [103, 104]. By adopting tilted metal evaporation with an incidence angle of 80°, gold nanocrescents have been prepared on self-assembled monolayers of polymeric particles, giving nanostructures with tunable LSP resonances and SERS enhancement [105].

Nanospheres lithography has also been exploited to produce templates for smaller nanoparticles self-assembly, such as arrays of silver nanocubes piles in reference 106, displaying hot spots at the corners and suitable for single-molecule SERS. Moreover, 2D substrates constituted of arrays of circular voids on a metallic film can be obtained by combining NSL with plasma etching or RIE [107]. It is possible to obtain a shrinkage of the beads size to a non-close packed array and to use such colloidal crystal as a mask for the deposition of the plasmonic metal. Tunable plasmonic properties can be obtained by selecting the size and circular or elliptical shape of the holes [108]. A particularly interesting example of the use of circular nanoholes as effective SERS substrates is given by the work of Baek et al. in reference 2. They took advantage of the BCPs self-assembly inside the holes in the gold film to promote the formation of nanogaps and generate a stronger SERS signal compared to the simple nanoholes structures.

2.2 3D substrates with assembly-induced hot spots

The long-standing goal of the research branch concerning SERS substrates is to push the detection limit to the single-molecule level, this has been obtained in some rare instances. On account of the fact that only the molecules adsorbed specifically in the hot spots of the substrate can profit from their extremely large electromagnetic field enhancement, SERS future advancement goes hand in hand with the development of nanofabrication capabilities to engineer the position of the hot spots and place the analyte inside that localised region.

As already mentioned in section 1.2.1, the aggregation of nanoparticles in solution and on solid supports is often beneficial for the production of electromagnetic hot spots in the interparticle crevices. Analogously, the formation of nanometre-sized gaps in between metallic features is promoted in 3D nanostructures. In recent years, the category of substrates constituted by assemblies of plasmonic nanopillars or nanowires (NWs) found great consent in the SERS community and new strategies were developed in this framework.

The use of arrays of thin InP standing NWs, grown from gold nanoparticles seeds and decorated with gold particles, has been discussed in the work in reference 109. After the deposition of the analyte, the NWs can self-close driven by the microcapillary force under the exposure to liquid and bind together in disordered clusters. Hot spots are formed in the interstices between metallic nanoparticles with distances of 5 nm or less. The molecules bound to the nanoparticles in the bundles

of NWs are trapped in the hot spots thus their Raman signal is strongly enhanced, by more than 11 orders of magnitude under certain conditions. Afterward Hu et al. proposed the use of tailored gold-coated polymer nanofingers or nanopillars capable of self-closing in regular groups of four units. Such a mechanism allows pursuing molecular trapping in the hot spots formed between the tips of the nanostructures [110]. The matrix of polymer nanopillars presents square lattice symmetry and was realised by the method reported in reference 111, based on nanoimprint lithography for the polymeric nanostructures preceded by EBL and RIE for the construction of the master mold. With well-established nanofabrication techniques, it is possible to achieve nanometre precision on the control of the gap size and a controllable number of nanopillars involved in the hot spots formation. Nonetheless, the fabrication suffered from some drawbacks concerning the expensive instrumentation and procedure and from the main limitation of EBL in terms of fabrication over large area. A different option for fabrication, employing BCP lithography and deep RIE, was proposed in reference 112.

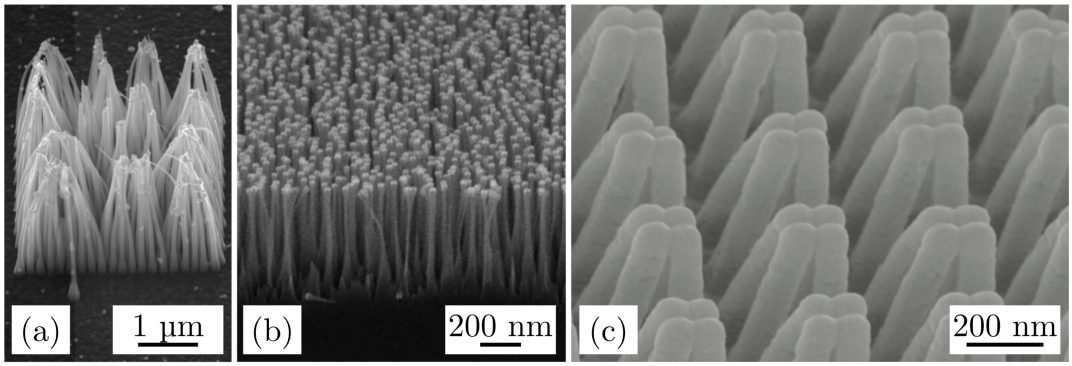

Figure 2.4: Cross-sectional SEM images of three examples of high-aspect-ratio structures forming clusters to trap the molecules in the hot spots regions in the nanogaps between the tips of the nanopillars. The images are reproduced from (a) reference 109 ©2008 IOP, (b) reference 112 ©2016 ACS and (c) reference 110 ©2010 ACS.

The promising results reported for this kind of SERS substrates gave start to other research activities on similar systems. An alternative way to achieve effective measurement platform with assembly-induced hot spots was proposed by Schmidt et al. [113]. They applied a simpler one-step fabrication procedure based on maskless dry etching to produce silicon nanopillars over large area. The nanopillars were subsequently coated with silver, forming oval caps on the tips. The characterised substrates displayed large enhancement, particular attention was given to the density of such NWs and its importance for the enhancement of the Raman intensity. The use of maskless RIE presents some disadvantages regarding the randomness of the sites where the NWs are located and usual issues associated with

the implementation of the method with expensive instrumentation and materials.

2.2.1 Strategy of fabrication and motivation

The need to develop a method for the realisation of high-aspect-ratio[3] and flexible nanostructures ordered over large-area still remains. The aforementioned method should accommodate the requirements on the SERS substrate, regarding enhancement capability and uniformity, with simple and low-cost processes avoiding the use of sophisticated instrumentation.

To give a contribution to the open search of suitable fabrication procedures for SERS substrates, a considerable part of the work of this dissertation was dedicated to the development of a fabrication protocol for the realisation of a substrate constituted of flexible gold-coated silicon NWs (SiNWs) especially tailored to generate hot spots when forming bundles for effective SERS detection. The NWs structures offer large area-to-volume ratio and have the ability to confine the incident light on the surface leading to improved enhancement of the electromagnetic field [114, 115]. A schematic representation of the gold-coated NWs is reported in figure 2.5.

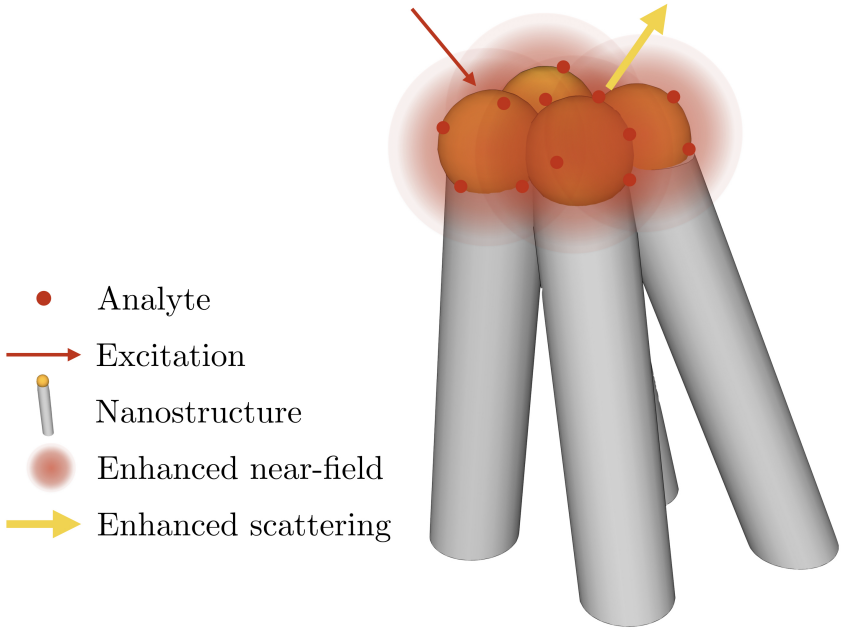

Figure 2.5: Illustration of the bundle of gold-coated SiNWs used as SERS substrates and whose development constituted a significant part of this dissertation.

The manufacturing of this SERS substrate is achieved with the combination

[3]The aspect-ratio of a nanowire is the ratio between the length and the diameter.

NSL to metal-assisted chemical etching. The latter is an anisotropic wet chemical etching process chosen as an alternative to conventional and expensive RIE, described in section 2.3.1. The chosen methods for fabrication purposes were matched to other standard physical vapour deposition, plasma etching technique and SEM analysis to achieve great tunability of the nanostructures in terms of in-plane and out-of-plane geometrical parameters, low-cost, easy implementation and compatibility with cm^2 area. The great versatility of these techniques is one of the reasons for adopting them for fabrication. Another consideration that motivate their use regards the interest to deepen the comprehension of the mechanism underlying the self-assembly of NSs as well as the etching of silicon and to develop the fabrication methods even further for applications including not only SERS but spanning from nanoelectronics, photonics, catalysis and energy production and storage to drug delivery, biological assays and sensing [116]. Another detail which is worth discussing is the choice of the materials for the substrate. Polymer-based substrates can be subject to chemical degradation over time as well as low mechanical and thermal stability. The use of silicon as substrate material brings significant robustness to the nanostructures and durable mechanical properties. The choice of gold over silver as the plasmonic metal is slightly more expensive but allows to avoid the oxidation and preserve the plasmonic activity over time thus improving the stability. In addition, many molecules containing the thiol functional group are available for Raman spectroscopy and form preferential bonds to the gold surface, as described in section 1.2.3.

2.3 Fabrication protocol

The fabrication of SERS-active nanostructures with NSL and MACE represents a favourable solution in terms of cost-effective realisation of functional nanostructures in orderly large-scale arrays. As thoroughly described in section 2.1.2, NSL constitutes a good candidate for SERS substrate fabrication. For its versatility, it is suitable to be combined to MACE allowing to build high-aspect-ratio nanostructures while cutting the cost usually related to the use of expensive RIE Bosch processes, requiring vacuum, high-frequency electronics, and ion optics.

2.3.1 Anisotropic wet etching

Metal-assisted chemical etching is an anisotropic wet electroless etching process to carve silicon and other semiconductors; reactions on Si/Ge, GaAs, GaN, and SiC have been demonstrated [117]. The process is characterised by the presence of an oxidising agent, usually H_2O_2 or HNO_3, which is reduced in a reaction catalysed by the presence of a metal. The most frequently-used catalytic metals are silver, gold, platinum and palladium in the form of spread particles, quasi-continuous or

patterned thin films on the wafer. In the following cathodic reaction, H_2O_2 is used as oxidising agent and gold as a catalyst:

$$2H^+ + H_2O_2 \xrightarrow{Au} 2H_2O + 2h^+.$$

The charge carriers generated by the first reaction, holes h^+, are injected into the semiconductor thus causing its oxidation. Consequently, the oxidised material is dissolved by a reaction with another reactant, typically hydrofluoric acid HF, to form a soluble silicon hexafluoride and gaseous H_2 [118]. The reaction involving silicon is reported hereafter:

$$Si + 4HF_2^- + 2h^+ \longrightarrow SiF_6^{2-} + 2HF + H_2(g).$$

The schematic of the two reactions leading to the etching of silicon by MACE is depicted in figure 2.6.

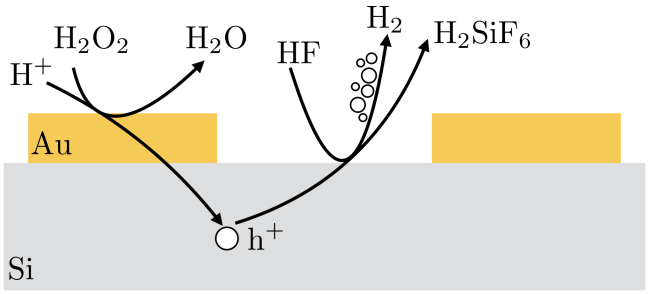

Figure 2.6: Schematic of the silicon etching reaction during metal-assisted chemical etching. Figure adapted from reference 118.

During the dissolution process when the catalyst is distributed in isolated particles, the etchant solution can penetrate under the metal to the etching front and the byproducts can easily diffuse. However, the mechanism of the process underneath an extended metallic film has been largely debated especially concerning the mass transport process. Different explanatory models have been proposed and these are discussed in references 117 and 119. According to one of the proposed model, the Si atoms would diffuse through the metallic film and would be oxidised and dissolved at the metal-solution interface. Another model expects the diffusion of both reactants and byproducts to occur through small openings in a non-continuous metallic film. In both these models, the diffusion length of silicon atoms is considered to be quite modest, typically some tens of nanometres equal to the thickness of the metallic film. A third model predicts that the oxidation of the silicon surface proceeds at the Si-Au interface through the formation of a porous layer. The porous

layer facilitates the diffusion of HF to the surface of Si and thus its dissolution as well as the diffusion of the byproducts. In this model, the diffusion length would be dependent on the lateral size of the metallic areas. In the experiments reported in reference 119, Geyer et al. tested MACE catalysed by metallic stripes with different lateral size and thicknesses to assess the validity of one of the proposed models. The experimental findings highlighted that the etch rate remains constant for increasing thickness, while it decreases for larger and larger stripes thus confirming the last model. The most recognised model is schematised in figure 2.7. The same model is reported in the work of Azeredo et al. in which a porous layer is used to increase the diffusion process of reactants in a direct imprinting process based on MACE [120]. The overall mechanism of MACE is based on the balance between the charge transfer kinetics at the catalyst-semiconductor interface and the rate of diffusion of the reactants and byproducts towards or away from the same interface.

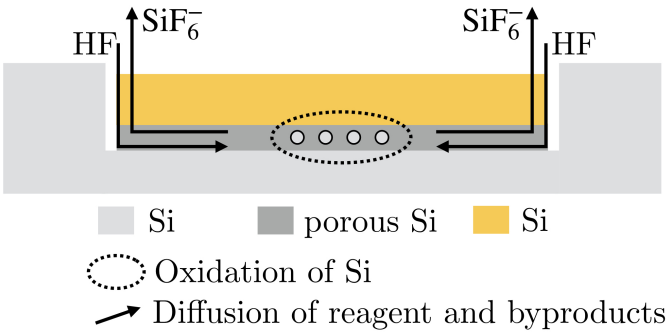

Figure 2.7: Schematic illustration of the main model proposed to explain the mass transport occurring during metal-assisted chemical etching catalysed by a metallic thin film.

The etch rate without any catalytic enhancement would be below $10\,\mathrm{nm\,h^{-1}}$, while it increases substantially when a metallic catalyst is introduced in the system with the possibility to achieve µm-long nanostructures within few minutes. Some unresolved aspects of the mechanism of the electroless etching regarding the role of the metal in the catalysis [118] are still present. Nonetheless, it is known that the etch rate during MACE depends on multiple factors, including morphological parameters of the catalytic metal, i.e. sizes of the openings and distances, doping type and doping level of the wafer and ratio between the concentration of oxidising and reducing species in the etchant solution (H_2O_2 and HF). The doping level and the reactants ratio also affect the morphology of the nanostructures. From the point of view of the reaction chemistry, if the rate of hole consumption at the silicon-gold interface is smaller than the holes injection rate, the unconsumed charge carriers can diffuse to the off-metal areas and sidewalls leading to the formation of microporous structures [117].

Moreover, the different etch rates in the metal and off-metal areas produce a great spatial control over the etching process. The morphology of the three-dimensional objects obtained by MACE is strictly related to the lateral dimensions of the metal distribution on the surface, either random or regularly patterned. This method allows to obtain vertically aligned nanowires across wafer-scale area and it is used for the micromachining of silicon and other semiconductors at scales from millimetre to nanometre for numerous applications including solar energy conversion devices [121], energy storage [122], thermoelectric nanowire devices [123] and gas sensing [124].

2.3.2 Combination of NSL and MACE

Both the bottom-up lithographic technique based on the self-assembly of colloidal nanoparticles and the metal-assisted chemical etching method are combined in the multistep fabrication process adopted for the realisation of SERS substrates and discussed in the following chapters. A brief overview of the steps of the fabrication procedure is reported hereafter and a scheme is displayed in figure 2.8.

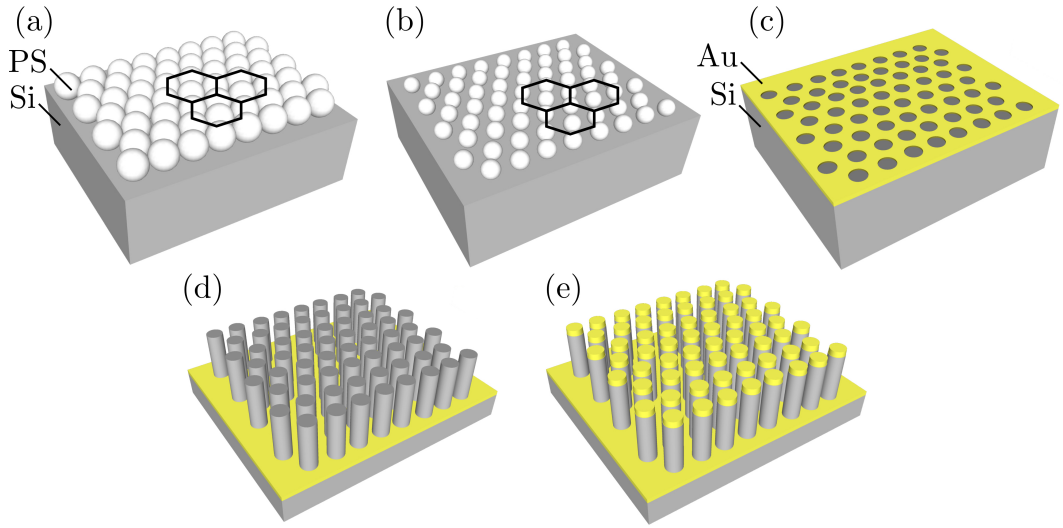

Figure 2.8: Schematic figure that summarises the multi-step fabrication process: (a) spin coating of the NSs in a HCP colloidal crystal, (b) plasma etching, (c) patterning of the gold thin film, (d) extrusion of the SiNWS, and (e) coating with gold.

The very first step of fabrication is the deposition of the NSs: this is achieved by spin coating. This choice is motivated by the fact that spin coating is well established in micro and nanofabrication to deposit uniform films of resist with adjustable thickness for optical and e-beam lithography. Additionally, it provides rapid implementation and compatibility with wafer-scale fabrication. A schematic

representation of the honeycomb symmetry of the monolayer of NSs is reported in figure 2.8(a). The manipulation of the colloidal mask is possible through a plasma etching process performed in a low vacuum chamber by accelerating Ar^+ ions on the sample. This technique allows a tunable control over the dimension of the NSs by keeping their centre-to-centre distance fixed to the original value and preserving the HCP symmetry. The reduced NSs are depicted in figure 2.8(b). The reduced NSs are used as a mask for the deposition of a thin film of gold so to obtain a patterned catalytic film reported in figure 2.8(c). The patterned film of gold is used for the etching process of silicon by MACE to extrude a matrix of ordered silicon NWs illustrated in figure 2.8(d). To produce the final substrate for SERS analysis, the SiNWs are coated with a layer of gold forming small cylinders or caps on their tips shown figure 2.8(e). The technical details of the fabrication regarding all the steps mentioned in this section are reported thoroughly in chapter 3. The quality of the whole manufacturing procedure is crucial for the realisation of reliable substrates so each step was optimised to fulfill the requirements of SERS measurements.

Part II

Methods

Chapter 3

Materials and methods

The purpose of this chapter is to present the technical details concerning the materials and the methods employed in the experimental activities of fabrication, characterisation and measurements described throughout the dissertation. The fabrication of the SERS-active substrate is treated in section 3.1.1 and 3.1.2. The methods adopted for the characterisation of the substrate are reported in section 3.2. The measurements of SERS enhancement on tailored substrates is described in section 3.3. Moreover, details on complementary fabrication and characterisation methods are provided in section 3.4.

3.1 Fabrication of the substrates

3.1.1 Nanospheres lithography

Synthesis of the nanospheres

The polystyrene nanoparticles were supplied by the Laus research group of Polymer Science at the University of Piemonte Orientale. The NSs were synthesised by using the emulsion polymerisation of styrene using sodium dodecyl sulphate as surfactant and potassium persulphate as the initiator. In emulsion polymerisation, the hydrophobic monomer is dispersed in a solution of surfactant and water at room temperature by stirring to obtain the formation of emulsified monomer droplets (ca. 1 - 10 µm) and micelles (ca. 5 - 20 nm in diameter). The amount of monomer and surfactant in the reaction mixture can be adjusted to obtain the desired particles size. The reactor is heated up above 50 °C and a water-soluble initiator is added to the emulsion. The initiator starts decomposing and it reacts with the micelles high surface area so that these are transformed into nuclei for the polymerisation and continue to grow by acquiring the reactant species from the monomer droplets. The mixture is reacted for 24 hours under a constant flux of nitrogen and the process terminates when the free monomer droplets are consumed. The final product of

the emulsion polymerisation process is a latex with particles of diameter between 100 nm and 2 µm.

The reaction was carried out in a five-neck reactor equipped with a condenser, a mechanical stirrer, a thermometre and inlets for nitrogen and styrene. The obtained latex was purified from reactants and unreacted styrene by repeated dialyses against ultrapure water and the polystyrene NSs were dispersed in Milli-Q deionised (DI) water (18 MΩ cm). The diameter of the NSs was determined by SEM D = 250 ± 4 nm; their hydrodynamic radium, determined by dynamic light scattering (DLS), is equal to 259 nm. The particles feature negative charges at the surface due to the decomposition of sodium persulphate providing anionic radicals SO_4^-. Like-charged colloids tend to repel each other and the surface charge can be exploited to render the dispersion stable against aggregation in the so-called charge stabilisation. All the experimental details regarding the adopted polymerisation process are reported in references 125 and 126.

Silicon wafer preparation

The first step of fabrication consists of the preparation of the silicon substrate for the deposition of the nanoparticles. The choice of the wafer depends on the MACE process; in this case, phosphorous doped silicon wafer with a thin layer of native oxide is selected with resistivity in the range from 27 mΩ cm to 47 mΩ cm (purchased from SunEDISON/MEMC). The n+ silicon wafer was cleaved in pieces of 1.5 cm per side; the polished surface was cleaned in an ultrasonic bath of acetone and subsequently in isopropyl alcohol (IPA) and it was dried with a nitrogen flux.

The surface of silicon is non-wettable in water, i.e. hydrophobic, meaning that a droplet of water has a high contact angle with respect to the surface. In order to be able to spread the aqueous suspension of NSs on the surface, it needs to be functionalised to make it hydrophilic. The hydrophilisation can be achieved by two methods. A very well-known method requires the use of piranha solution; this is a solution of sulfuric acid and hydrogen peroxide mixed with $H_2SO_{4(96\%)}$:$H_2O_{2(35\%)}$=3:1 volume ratio. The surface funzionalisation can be performed by heating the solution on a hot plate up to 80 °C and by soaking the samples in the solution for 90 minutes. Handling the piranha solution presents some safety issues and the process itself is quite lengthy. It was substituted by a rather safer and quicker method consisting in the wafer surface activation by oxygen plasma. The plasma was generated at 40 W power by using a tabletop plasma cleaner (Plasma matrix Bdiscom), the treatment only lasted 6 minutes reducing considerably the duration of the wafer preparation.

Deposition of the nanospheres

The following step consists in the deposition of the NSs on the functionalised substrate. As already mentioned in section 2.3.2, the method selected for the deposition

was spin coating. By using a programmable spin coater (Laurell technologies WS-400B-6NPP/LITE), it was possible to select the spinning speed [1] ω and acceleration α. The duration of the process can be selected as well as the number of steps with different settings. A controlled volume of 60 µl of the aqueous suspension of PS nanospheres was deposited on the substrate and it spread covering the whole functionalised surface. As soon as the spin coater is started, the colloidal suspension starts becoming thinner and the self-assembly process is triggered as described in section 2.1.2. An example of nanospheres self-assembly used for the following steps of fabrication of SERS substrate discussed in this dissertation is shown in figure 3.1.

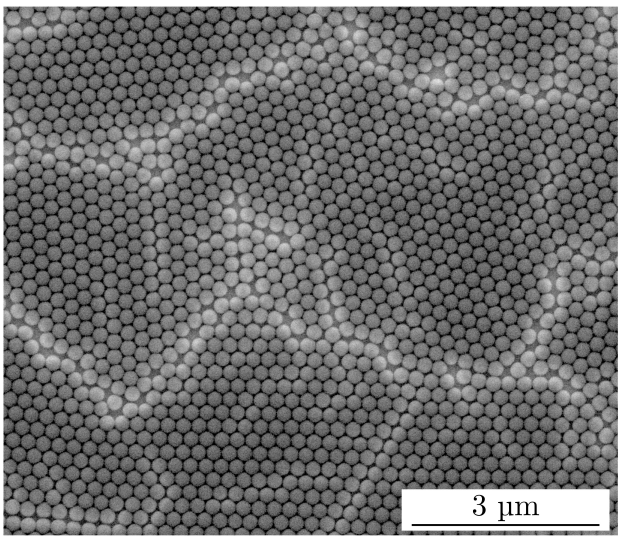

Figure 3.1: SEM image of an HCP-ordered monolayer of nanospheres of 250 nm in diameter. The monolayer is divided into domains with random shapes and orientation.

The formation of the monolayer was obtained by setting two spin coating steps. The adopted spin coating protocol consisted of two steps; the first step was set to last 10 s where ω and α are set to 500 rpm and 410 rpm/s, respectively. The second step, starting consecutively to the first one, had a duration of 30 s. The speed and acceleration were set to 3000 rpm and 1000 rpm/s, respectively, for the tests described in section 4.2. As part of the work reported in section 4.4, the speed and acceleration in the second spinning step were adjusted to several values by keeping

[1] The conventional unit of measurement for the speed of rotation around a fixed axis is rotation per minute (rpm) and it is usually used for the spin coating speed. This unit does not exist in the international system of units (SI), however, the conversion is done considering the measured physical quantities so that $1\,\mathrm{rpm} = \frac{\pi}{30}\mathrm{rad\,s^{-1}} = \frac{1}{60}\mathrm{Hz}$.

their ratio, i.e. the ramp time, fixed to 3.05 s. All the values adopted are reported in table 3.1

First step (10 s)		Second step (30 s)		
ω (rpm)	α (rpm/s)	ω (rpm)	α (rpm/s)	Reference
500	410	3000	1000	section 4.2
		1000	328	section 4.4
		1250	410	
		1500	492	
		2000	656	
		2250	738	
		2500	820	
		2750	902	
		3000	984	
		3500	1148	

Table 3.1: Rotational speed and acceleration settings of the two-steps spin coating process.

Control of nanospheres size

After the deposition step, the substrate presents a monolayer of PS nanospheres arranged in a compact manner. The NSs size can be reduced by treating the sample by plasma etching by setting the power and time of the process. The time of the treatment can be changed with respect to the desired final size of the nanoparticles. The minimum time is related to the necessity to separate the NSs and avoid the formation of polystyrene bridges between two adjacent spheres. The maximum duration of the plasma is set so that the spherical shape of the nanoparticles is preserved, in fact, the NS get flat and their edges lose definition for overextended plasma etching. In this process, pure argon plasma was used for the manipulation and was generated at 75 W RF power in a pressure of 1 Pa. Starting from NSs with diameter D of 250 nm, the minimum and maximum time could be set to 5 and 8 minutes leading to NSs diameter from 200 nm to 130 nm, respectively. The original centre-to-centre distance (250 nm) was maintained after the reduction of the nanospheres and the hexagonal lattice was preserved. For the realisation of the nanowires substrate for SERS the reduction time was set to 8 minutes.

Metallic film patterning

The hexagonal non-closed packed monolayer of nanospheres constitutes a shadow mask for the subsequent metal deposition. A layer of gold with a thickness of 20 nm was deposited by e-beam evaporation in a high-vacuum chamber with a base pressure of 5×10^{-5} Pa to ensure high purity. The filament current was set to

35 mA and the emitted electrons were accelerated by a 6 kV voltage. By keeping the sample at a fixed distance of 10 cm from the crucible, the deposition rate was $1.5\,\mathrm{nm\,s^{-1}}$.

After the evaporation, the colloidal mask was lifted off by soaking the sample in an ultrasonic bath of ethanol (EtOH) for 6 minutes at 50% of the power. The resulting pattern on gold consisting of a two-dimensional array of holes in the original position of the spheres is shown in figure 3.2.

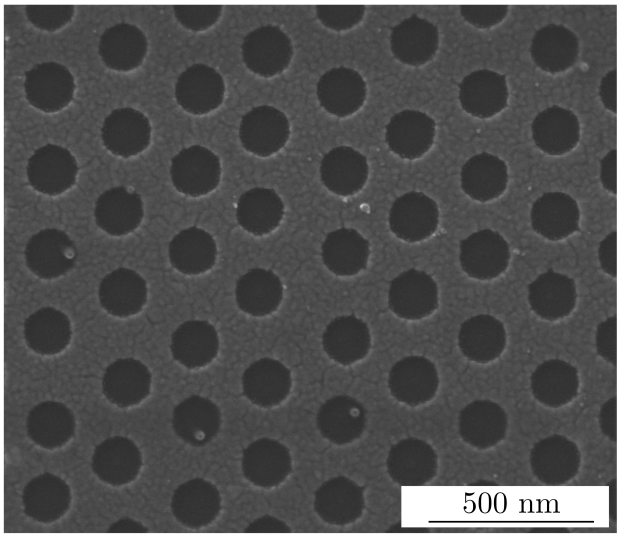

Figure 3.2: SEM image of the hexagonal non-close packed pattern of circular holes in the 20 nm-thick layer of gold.

3.1.2 Metal-assisted chemical etching

The patterned gold mask resulting from NSL is used to catalyse the chemical etching process of silicon: the geometry of hexagonal non-close packed circular voids is transferred to the underneath bulk silicon by MACE.

Preparation of the etchant solution

The etchant solution used for the etching of n+ type silicon was prepared with hydrofluoric acid, hydrogen peroxide and DI water mixed with a proportion of $HF_{(50\%)}$, $H_2O_{2(35\%)}$ and H_2O equal to 3:1:1 in volume, as related to the results in section 4.2. In the subsequent work presented in section 4.4, the use of DI water was substituted with EtOH which increases the adhesion of the gold layer to the substrate [127]. Thus the etchant solution was made with $HF_{(50\%)}$, $H_2O_{2(35\%)}$ and EtOH with a 10:1:3 ratio in volume. All the reagents were purchased by Carlo Erba Reagents.

Etching process

The sample was mounted inside a Teflon cell with a circular opening of 1 cm leaving the silicon wafer exposed. The sample was rinsed with EtOH and then a volume of 5 ml of the freshly prepared etching solution was poured on the sample. As already explained in section 2.3.1, the rate of the etching process depends on the time of exposure to the solution, on the doping level of the wafer and on the HF:H_2O_2 ratio. As related to the solution containing water used for the preparation of the samples described in section 4.2, the etching time was set between 30 s and 60 s to obtain nanowires with a aspect ratio of 5:1 and 10:1. In the second solution, used for samples described in section 4.4, the higher HF:H_2O_2 ratio reduces the etch rate making the process more tunable; in this case, the time of the process was set to 210 s to obtain nanowires of aspect ratio 10:1. To stop the process, the sample was rinsed abundantly with EtOH. The nanostructures were let to dry in air to end up with a matrix of standing silicon nanowires, as shown in figure 3.3. The use of nitrogen gun is discouraged at this stage since the strong flux of nitrogen can bend or break the nanowires.

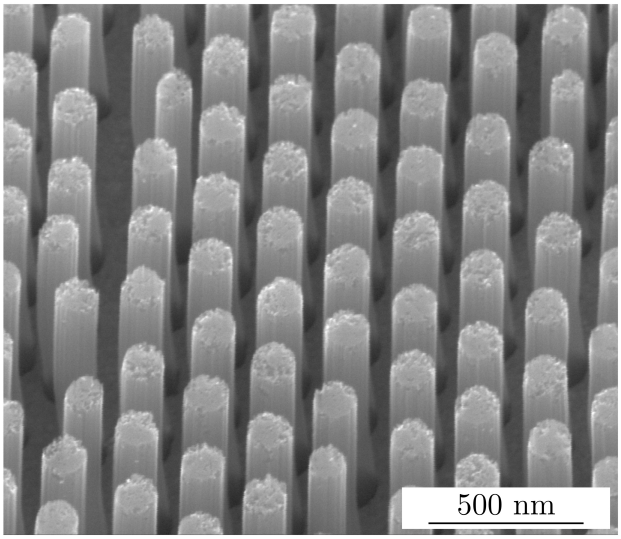

Figure 3.3: SEM image of the ordered matrix of high aspect ratio SiNWs.

3.2 Characterisation of the substrates

3.2.1 Scanning electron microscopy

In parallel to the fabrication, a characterisation of the substrate was carried out by means of scanning electron microscopy at INRiM NanoFacility Piemonte laboratory using an FEI Inspect-F^{TM} field emission gun (FEG) SEM. The SEM is a common

type of electron microscope that produces images of a suitable sample by scanning its surface with a focused beam of electrons. The interaction of the primary electrons with the matter produces several signals carrying information related to the surface topography and elemental composition of the specimen. The secondary electrons are ejected from the K shell of the atoms at a distance of 5 nm to 50 nm from the sample surface and their detection gives morphological information of the specimen.

For the characterisation, the substrate was located inside the vacuum chamber (1×10^{-3}-1×10^{-4} Pa). The operational conditions depended on the stage of fabrication of the specimen and on the features to be observed. The electrons acceleration voltage was set to 10 kV to observe PS nanoparticles compact or non-compact monolayers to reduce the charging effect on the insulating material and usually the acquisition of SEM micrographs was carried out from a top view by keeping the stage at 0°. The voltage was increased up to 30 kV for the conductive patterned gold film or SiNWs and gold-coated structures. For the measurements of holes diameter in the gold film, the top view configuration was adopted, but in the case of three-dimensional nanostructures, the cross-sectional view at 30° or 80° was used to measure the length of the nanowires. The full cross section of the nanowires was measured by placing the specimen on a 90°-stub and tilting it at 10°.

All the SEM measurements were carried out at the optimal working distance from the secondary electron detector equal to 10 mm. Different magnifications were adopted ranging from 10000 times to 120000 times depending on the feature size; for systematic investigation of the NSs monolayer quality, discussed in section 4.4, the acquisition of the SEM micrographs was done at the same magnification of 10000 times and the resolution was set to (2048 × 1886)pixels.

3.2.2 Image processing

The quality of the NSs monolayer was evaluated by performing image processing and quantitative analysis using a MATLAB© tool. The results regarding this analysis are reported in section 4.4.

The operating principle of the software is based on the recognition of each NS in the image within a given interval of dimension and with a certain sensitivity level influenced by contrast and brightness of the image itself. Each particle in the frame of analysis is represented by a lattice point in the HCP matrix. The plane of lattice points is divided into a triangular mesh according to the rules of Delaunay triangulation[2] so that each point is connected to its nearest neighbours. Each point having less or more than six nearest neighbours, expected in the sixfold

[2]Delaunay triangulation, named after the Russian mathematician who worked on its development, is a subdivision of a plane into triangles $DT(\mathcal{P})$ such that, for a given set of points $\mathcal{P}$, no point in $\mathcal{P}$ is found inside the circumcircle of any triangle in $DT(\mathcal{P})$.

coordination of the HCP symmetry, constitutes a defect [128]. The presence of defective points delimits the boundaries of the domains with random shapes and orientations composing the NSs monolayer. An example of an SEM image analysed with this software is reported in figure 3.4(a) and the corresponding diagram of triangulation is reported in figure 3.4(b). The blue and red circles specify the appearance of defects where the highlighted nanoparticle is connected to five or seven nearest neighbours, respectively.

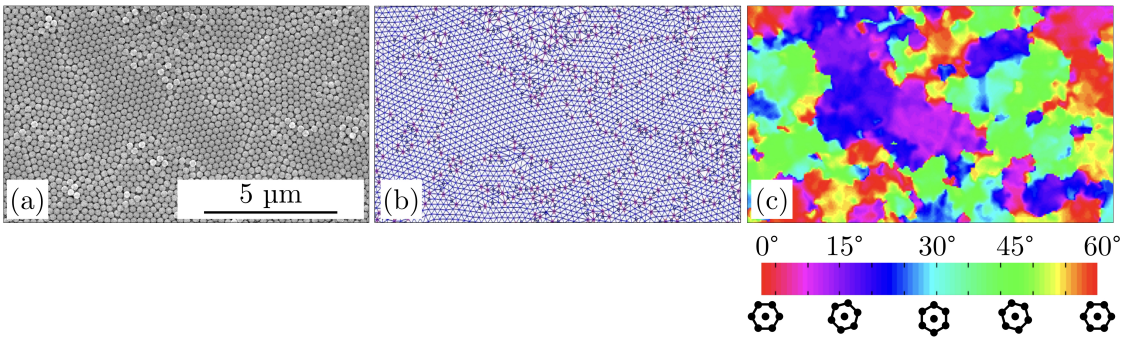

Figure 3.4: (a) SEM micrograph of the nanospheres monolayer. (b) Delaunay triangulation diagram of the HCP domains where the lattice points with five or seven nearest neighbours are highlighted as defects in blue and red, respectively. (c) The colour map of the triangulation diagram is generated to calculate the orientation of the NSs domains. A short video showing the superposition of the colour map is visible here.

From the triangulation diagram, the software extrapolates a colour map wherein each colour variation corresponds to a different orientation of the HCP unit cell, as displayed in figure 3.4(c). Furthermore, the software elaborates the data from the colour map to generate the so-called autocorrelation function $ACF = \mathrm{e}^{-\overrightarrow{r}/\xi}$, where $\overrightarrow{r}$ is the vector indicating the location of the domains in the two-dimensional lattice [129] and ξ is the correlation length, i.e. the distance within which the coherency of the HCP symmetry is preserved.

3.3 SERS measurements

3.3.1 Substrate preparation

After the matrix of standing SiNWs was obtained by NSL and MACE, the final substrate for SERS was prepared by coating the NWs with 80 nm of gold by e-beam evaporation and obtain caps of gold on the top parts as displayed in figure 3.5. The gold caps thickness was chosen according to reference 130.

Two different analytes were used to test the performance of the SERS substrates included in this dissertation, both were purchased from Sigma Aldrich. Melamine

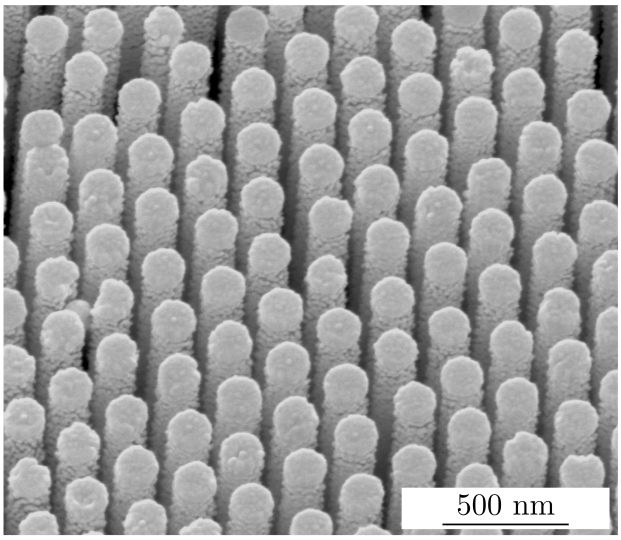

Figure 3.5: SEM image of the SERS substrate constituted of gold-coated SiNWs.

molecule ($C_3H_6N_6$), whose chemical structure is shown in figure 3.6a, was used in several concentrations ranging from 100 mg l^{-1} to 1×10^{-5} mg l^{-1}, declared in the different part of the discussion in chapter 4 and 5. The solutions were prepared in Milli-Q DI water by serial dilution of a stock solution at 1000 mg l^{-1}. The molecule was deposited by drop casting or incubation and either water or EtOH were used as solvents. Further tests were carried out by using 7-mercapto-4-methylcoumarin ($C_{10}H_8O_2S$), reported in figure 3.6b, for which a solution in EtOH was prepared at the concentration of 1 mM. The substrate was incubated in the solution for 120 minutes and rinsed abundantly with EtOH to remove any excess and to be able to assume a monolayer coverage on the nanostructures. Prior to deposit the analyte on the substrate, it is advisable to remove any organic residue that may be present on the substrate. In order to do so, the gold-coated samples were subject to a cleaning process with oxygen plasma generated at 40 W for 1 minute.

3.3.2 Spectra acquisition

The Raman spectra of the probe molecule enhanced by the gold-coated silicon NWs were recorded using a Raman imaging confocal microscope (Thermo Scientific DXR^{TM} xi) equipped with an excitation laser source at 780 nm and a charge-coupled device (CCD) detector. The substrate was placed on a motorised stage with a minimum step size of 1 µm; the position along the z-axis was set by focusing the laser beam on the tips of the nanowires so to maximise the enhanced intensity of the Raman signal. The target of SERS experiments is often the detection of low concentration of the probe molecules through a favourable signal enhancement. Whenever the maximum achievable signal is too low, some instrumental conditions

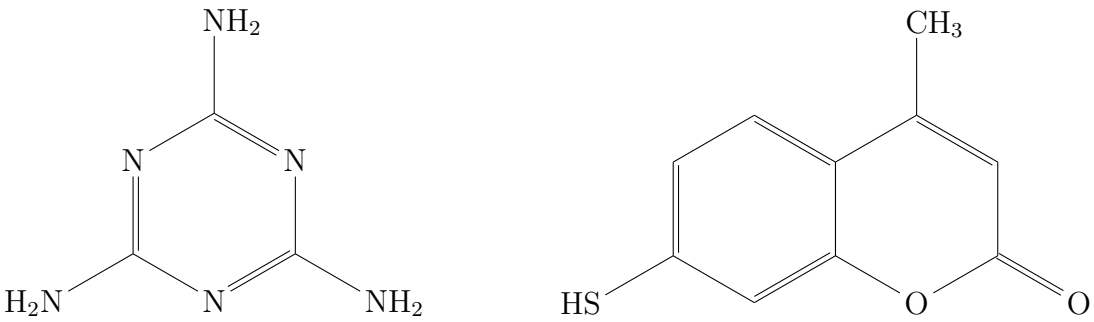

(a) Melamine (b) MMC

Figure 3.6: Probe molecules used for SERS measurements performed on the gold-coated SiNWs substrate.

can be changed. A possible solution is to increase the laser power compatibly with sample-damage issues or to increase the scattering volume and therefore the surface area of detection. With these premises, different conditions were applied for the acquisition of the SERS signal of the two probe molecules. For melamine the spectral range was extended from $300\,\mathrm{cm}^{-1}$ to $1100\,\mathrm{cm}^{-1}$ with a full range resolution grating of $5\,\mathrm{cm}^{-1}$, a the laser power and integration time were set to 24 mW and 1 s for 20 repetitions, respectively. On the other hand, the detection of MMC was conducted in the spectral range from $250\,\mathrm{cm}^{-1}$ to $1750\,\mathrm{cm}^{-1}$ with a full range resolution grating of $5\,\mathrm{cm}^{-1}$ and it was set to have a laser power of 8 mW and an integration time of 1.67×10^{-3} s for 10 scans. Both measurements were carried out by using a 10× microscope objective and a pinhole aperture of 50 µm. The laser spot width was 1.9 µm. The experiment for the calculation of the enhancement factor, reported in section 5.2, was conducted by using the same instrumentation equipped with a 20× long working distance microscope objective and by setting an exposure time of 1 s for 20 scans at a laser power of 8 mW. The use of x and y motors allowed to scan the surface of the substrate across some tens of mm^2, with a step size depending on the interest on the surface variation of the signal enhancement and set to 150 µm in the experiment reported in section 4.2. For the detection of MMC in the experiment reported in section 4.4, the step size was set to a minimum of 8 µm and a maximum of 50 µm at different phases of the experiment.

3.3.3 Data analysis

The computation and assignment of the spectra were conducted by the group of optical spectroscopy at INRiM. The geometry optimisation of the model molecule structures was carried out without imposing any constraint and the consequent calculations of the vibrational (IR and Raman) spectra were computed with a

discrete Fourier transform (DFT) method using Gaussian 03 software [131]. The computation procedure to obtain the vibrational information was performed with the Lee, Yang and Parr (LYP) correlation functional combined with the Becke's non-local three-parameter hybrid exchange functional (B3) [132]. The simulated spectra were compared to the experimental ones acquired on the SERS substrates so to assign the vibrational modes to the main bands [133]. The acquired spectra were processed to extract the chemical images based on the peak of interest in the Raman spectrum, by selecting its baseline and intensity. The spectral maps were processed with MATLAB© for map unfolding and statistics.

3.4 Complementary methods

3.4.1 X-ray fluorescence characterisation

A complementary characterisation of the SERS substrates was performed by X-ray fluorescence (XRF) measurements to determine the number of MMC probe molecules on the gold-coated SiNWs arrays. The basic principles of XRF are described in section 5.3.1 and the results of such characterisation are reported in section 5.3.2.

Experimental setup

The XRF characterisation was performed at the laboratory of Physikalische-Technische Bundesanstalt (PTB), German NMI, with a dedicated beamline at BESSY II electron storage ring, a third generation synchrotron radiation source emitting brilliant photon pulses in a broad energy range from the terahertz waves to hard X-rays. PTB beamline is equipped with a four-crystal monochromator (FCM) for bending magnet synchrotron radiation with high spectral purity and high photon flux in the hard X-ray energy range from 1.75 keV to 10.5 keV[3]. At the end station of the beamline, the sample is inserted in an ultra-high vacuum (UHV) chamber with carefully designed sample manipulator with nine axes which allows extreme precision in the procedure of alignment to the incoming beam. A thorough description of the experimental setup used at PTB can be found in reference 134, while a scheme of the adopted experimental condition is visible in figure 3.7 where a top-view of the chamber is depicted.

For the quantification of SERS probe molecule containing sulphur, the low-divergence monochromatic incident X-ray beam was set to have an energy $E_0 =$

[3]The electronvolt (eV) is a unit of energy commonly used in atomic and nuclear physics and in the synchrotron science. It is defined as the energy gained by an electron when it is accelerated by a potential of 1 V; in SI units it corresponds to 1.602×10^{-19} J.

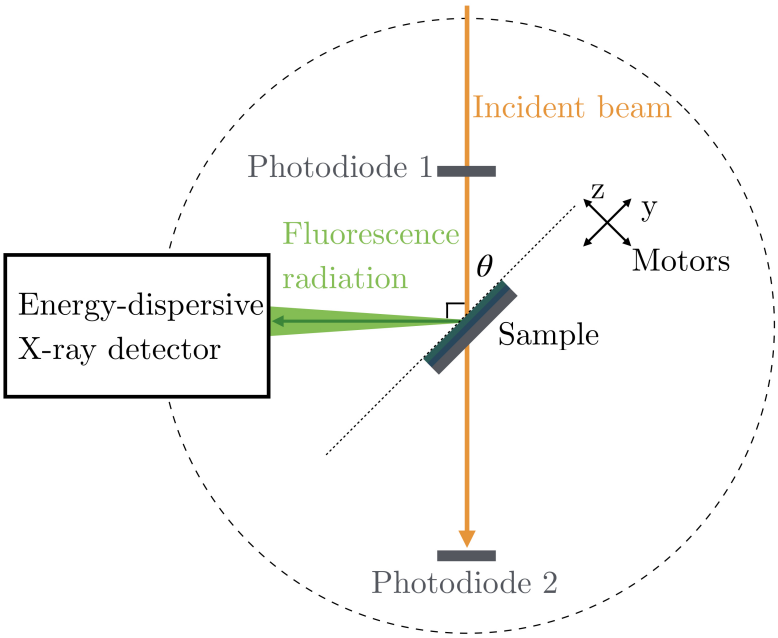

Figure 3.7: Instrumental setup for X-ray fluorescence measurements at the PTB FCM beamline at the BESSY II storage ring. The sample is inserted in a UHV chamber on a manipulator and its position is set along three translational axes with respect to the incident X-ray beam and one rotational axis θ to vary the angle of incidence on the surface. A calibrated energy-dispersive detector is used to measure the fluorescence signal. Two calibrated photodiodes are used during the alignment procedure and to measure the incoming photon flux. Figure adapted from reference 135.

2.5 keV, larger than the X-ray adsorption edge for sulphur K shell 2.472 keV. The presence of motorised calibrated photodiodes inside the chamber allows monitoring the conditions of the beam. The beam width is equal to 361 µm. Moreover, the photon flux f_0 incident on the sample is calculated by the formula in equation 3.1:

$$f_0 = i_{\text{meas1}} \cdot \frac{i_{\text{ref2}}}{i_{\text{ref1}}} \cdot \frac{1}{E_0} \cdot \frac{1}{R_2(E_0)}, \tag{3.1}$$

where i_{meas1} is the photocurrent generated during the fluorescence measurement by the incoming beam on the upstream photodiode, marked as 1 in figure 3.7. This is corrected by the ratio of the current measured by the calibrated photodiode 2 i_{ref2} and the current on the upstream photodiode i_{ref1} during a preliminary reference measurement. All the photocurrents are expressed in ampere. The factor $R_2(E_0)$ is the responsivity of the photodiode 2 at the energy of the incident beam, R is expressed in A W^{-1}, and E_0 is expressed in J. The dimensional analysis leads to an incoming photon flux expressed in photons/s. The estimated incident photon flux

for the measurement under discussion was $f_0 \approx (4.497 \pm 0.004) \cdot 10^8$ photons/s.

In the exploited configuration, the incoming beam impinged on the sample placed in an upright position[4] and the angle of incidence θ between the beam and the sample surface was varied in the range from 27.5° and 45° with a step width of 0.5° and an angular resolution of 0.0005°. The emitted fluorescence occupies a cone-shaped volume and it is detected by means of an energy dispersive X-ray detector, precisely a silicon drift detector (SDD), mounted at 90° with respect to the incident beam. The detector is calibrated for its response functions and detection efficiency at different energies [135]. The solid angle of detection $\Omega/4\pi$ gives the portion of the fluorescence signal which is detected and it is calculated through an algorithm implemented by PTB, from the active area of detection, the width of the primary beam, the distance between the detector and the sample (215 mm) and the offset angle of incidence ($\theta_0 = 0.269°$), which is the θ-motor position when the beam is parallel to the sample surface. The solid angle of detection remained constant to $\Omega/4\pi = 0.01134$ sr in the angular range of the measurement. Another instrumental parameter of interest for the treatment of data is the detector lifetime LT which was set to 249.4 s. All the calculations on the instrumental parameters are implemented using IDL (Interactive Data Language).

3.4.2 Directed self-assembly

The study of the directed self-assembly (DSA) of nanospheres by hard-template on the substrate is illustrated in section 6.1. The realisation of the samples required the steps described in section 3.1.1, however, some relevant differences and additional steps are described hereafter.

Direct laser writing lithography

The choice of the substrate for the production of hard templates fell on polished silicon wafer with thermally grown SiO_2 with thickness ranging from 50 nm to 200 nm. As well as the flat silicon wafers, the substrates used for the patterning step are cleaved to be 1.5 cm per side. For the preparation of the templates, direct laser writing (DLW) lithography was chosen. Analogously to standard optical lithography, the wafer is covered with a homogeneous film of photosensitive polymeric resist, as shown in figure 3.8(a), and it is exposed to light in the regions corresponding to the desired pattern. DLW enables the free design of complex geometrical patterns without the need of a shadow mask and for this reason it is categorised as a serial-writing lithographic technique. Such direct writing principle makes DLW lithography very adaptable and allows the preparation of templates with different

[4] As related to the experimental setup described in reference 134, the upright position corresponds to setting φ and χ angle to 90°.

shapes and sizes with a limitation in terms of the resolution and depends on the laser beam size.

The design of the templates was obtained using a Heidelberg μPG101 laser writer, equipped with a 2 mm laser head ($\lambda = 375$ nm) with a laser spot resolution of 900 nm and an intensity between 10 mW and 15 mW. The exposed resist was developed for 40 s in a 1:1 solution of AZ Developer (Merck Performance Materials GmbH) and H_2O and finally rinsed in deionised water for 60 s; the remaining resist shielded the silicon wafer from the subsequent etching process, as illustrated by figure 3.8(b). The quality of the development step was verified by an optical microscope. Hexagonal and linear shapes were selected for the design of the templates. The lateral dimension was set to a multiple of the diameter D of the nanospheres to be confined (250 nm), 4.5 µm in the hexagonal templates and 3.75 µm in the linear ones, to accommodate an integer number of particles in one line.

Reactive ion etching

After the development of the exposed photoresist, the pattern transfer to the oxide layer was achieved by RIE using a chemically reactive plasma. A schematic illustration of the result is shown in figure 3.8(c) and after the etching step the excess resist was removed by dipping the sample in acetone. A mixture of two gaseous species, CHF_3 and Ar, was prepared in the chamber using a flowmeter with a flow ratio of 54 sccm to 29 sccm and the plasma was generated with a residual pressure equal to 180 Pa and applied power of 300 W with typical reflected power of 25 W. Under these operating conditions, the etch rate on SiO_2 was 10 nm/minute. The depth of the templates H and the time of etching were selected by keeping the size of nanospheres, employed for the self-assembly process, as the upper limit in order to avoid the accumulation of multiple layers inside the templates. In this way, the templates were prepared with different depths selected to be fractions of the spheres diameter D, including H = 50 nm (H/D = 0.2), H = 100 nm (H/D = 0.4), H = 150 nm (H/D = 0.6) and H = 200 nm (H/D = 0.8).

Deposition of the nanospheres

The deposition of the NSs on the templated substrates, as schematised in figure 3.8(d), requires the same functionalisation step as the flat substrate and was performed by the spin coating process. Two different set of spinning parameters were selected $\omega = 1250$ rpm and $\alpha = 410$ rpm/s or $\omega = 2500$ rpm and $\alpha = 820$ rpm/s. A scheme representing the fabrication of the templated substrate is reported in figure 3.8, where the hexagonal templates have been taken as an example.

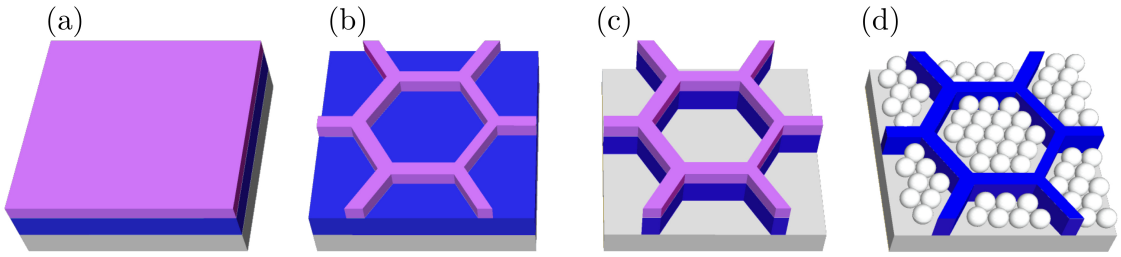

Figure 3.8: The hexagonal templates are taken as an example for the illustration of the fabrication process. (a) The silicon (grey) substrate with a thermal SiO_2 layer (blue) is covered with a homogeneous layer of photosensitive resist (purple) to which the hexagonal pattern is transferred by DLW lithography. (b) The exposed resist is developed and (c) the underlying SiO_2 layer is etched by RIE. (d) The excess photoresist is removed and the polystyrene nanospheres are deposited inside the trenches.

SEM and AFM characterisation

The confinement of the nanoparticles inside the templates was investigated by means of atomic force microscopy (AFM). This technique, belonging to the family of scanning probe microscopies, is often used to characterise surfaces at extremely high resolution by very sensitive detection of the probe movement along the z-axis. AFM was adopted to discern the role of the depth of the templates in the confinement processes. The surface topography on the NSs soft material was investigated by means of an atomic force microscope (Bruker Corp. INNOVA microscope) by using etched silicon probes (Bruker RTESPA-300) with nominal spring constant and tip radius of $40\,\mathrm{N\,m^{-1}}$ and 8 nm, respectively. The measurements were performed in tapping mode[5] with a resonance frequency of 230 kHz and a scanning rate of 0.5 Hz. The analysis and post-processing of the AFM micrographs were carried out by the freeware Gwyddion, including correction for plane inclination.

Systematic SEM analyses were conducted analogously to the case of the self-assembled colloidal crystal on the flat substrate. The SEM micrographs were processed using the MATLAB© tool presented in section 3.2.2 implementing an additional masking step to exclude the mesas from the processing. The ordering process inside the templates was evaluated through the quantitative analysis of the orientation of HCP domains.

[5]The tapping mode maps the topography by lightly tapping the surface with the AFM probe that is oscillated at its resonant frequency, this modality allows imaging of delicate and soft samples.

Part III

Results and Discussion

Chapter 4

Morphological characteristics of the SERS hot spots

The work reported in this chapter regards the necessity to control the location of the hot spots on the SERS substrate constituted of gold-coated silicon nanowires as well as the molecule positioning with respect to these localised regions of large enhancement. The flexibility of the NWs is especially exploited for the formation of bundles leading to hot spots. Moreover, the degree of order of the nanostructures is evaluated in terms of the quantitative index ξ, the correlation length. This is achieved by means of a systematic analysis of the SEM micrographs of the monolayer of colloidal spheres used in NSL for the fabrication of the substrate. The intensity of the SERS signal produced as a function of the degree of order is also investigated. The empirical study on the mechanical bending of the SiNWs is reported in section 4.1, followed by the determination of the most efficient configuration for the enhancement in section 4.2. Moreover, a brief introduction of the relevance of the distribution and density of hot spots is given in section 4.3. Subsequently, the quantitative evaluation of the degree of order is described in section 4.4 while its influence on the signal intensity is treated in section 4.5.

The content of this chapter and part of its text are reported in two articles published by the author of this dissertation in references 125 and 136.

4.1 Flexible plasmonic nanostructures

As introduced in section 2.2, the engineering of the hot spots is an essential aspect of modern research on SERS, focusing on the location of the hot spots on the plasmonic nanostructures and the position of the probe molecule with respect to these regions. Assembly-induced hot spots constitute a significant improvement of 3D SERS substrates and several fabrication protocols have been proposed to

obtain nanowires or nanofingers, made of several materials, with the ability to bend forming bundles.

The fabrication protocol constituted of the combination NSL and MACE allows tuning both the lateral dimensions, such as diameter and centre-to-centre distance, and the vertical dimensions, i.e. length of the nanostructures. By changing the time of etching, it is possible to exploit the mechanical properties of the SiNWs by fabricating wires with different lengths. When the aspect ratios are exceedingly larger than 10:1, the NWs bend and stick together to form bundles during the drying phase after etching as visible in figure 4.1(a). On the other hand, SiNWs with aspect ratio of 5:1 remain straight exhibiting high stiffness after the evaporation of solvent used for etching (either water or ethanol), as shown in figure 4.1(b).

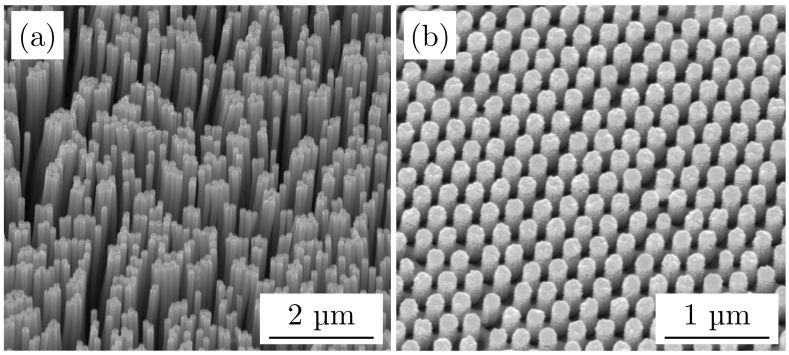

Figure 4.1: (a) SiNWs with high aspect ratio (larger than 10:1) sticking together to form bundles. (b) SiNWs with aspect ratio of 5:1 exhibiting straight morphology.

A substrate of standing SiNWs with aspect ratio 10:1 was coated with a droplet of water and dried in air. The NWs exhibited high flexibility since they were induced to lean and stick together forming different groups in the area exposed to the evaporation of water. Figure 4.2(a) presents a low-magnification SEM image of the droplet edge. A zoomed view of the area outside of the droplet is reported in figure 4.2(b) where standing nanowires are visible, while the nanowires lean onto each other inside the droplet region as visible in figure 4.2(c). The optimal aspect ratio to have SiNWs that remain straight after the fabrication but are flexible and can be induced to bend is 10:1.

By substituting the droplet of water with ethanol, no mechanical bending was induced. The leaning phenomenon could be explained by the onset of capillary forces during the evaporation of water due to its surface tension coefficient, $\gamma_{H_2O} = 72.8\,\mathrm{mN\,m^{-1}}$ three times larger than the one of ethanol $\gamma_{EtOH} = 22.39\,\mathrm{mN\,m^{-1}}$. According to the Young-Laplace equation[1], the pressure in between the nanowires,

[1]The Young-Laplace equation $\Delta(P) = \frac{\gamma}{R}$ gives the capillary pressure arising at the interface

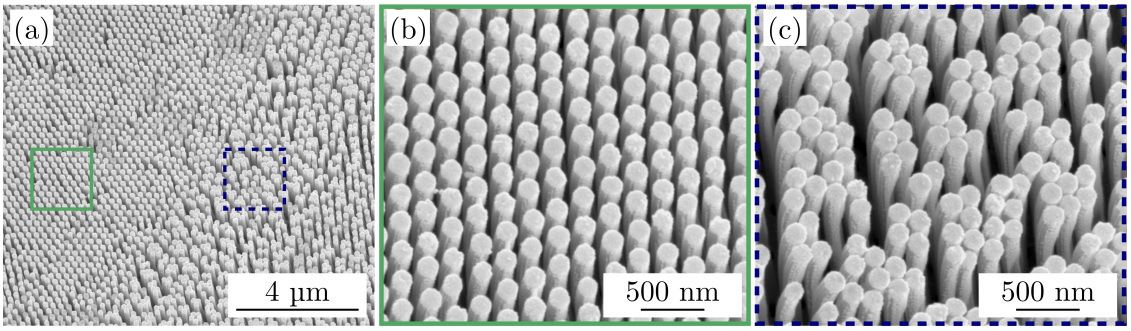

Figure 4.2: (a) Low-magnification SEM image showing the region at the edge of the drop of water deposited on the substrate. (b) SEM image of a small area outside of the drop where the gold-coated nanowires stand straight. (c) High-magnification image showing the groups of leaning silicon nanowires formed after the evaporation of water.

where water is evaporating, is lower than in the neighbouring areas and this could exert a bending moment on the NWs [137]. The patterning by NSL and the flexible nanowires with high aspect ratio obtained by MACE allow to produce a distribution of bundles across cm^2 area, which could be difficult to obtain with a fabrication based on EBL and RIE.

4.2 Efficient assembly-induced hot spots

It is known from the literature that, in flexible and leaning nanostructures, a hot spot is created at the tip-to-tip site so that a multitude of electromagnetic hot spots can be found on the substrate. To prove the most convenient configuration for the enhancement of Raman scattering on the substrate, the aspect ratio of silicon nanostructures and the position of the analyte were investigated. The probe molecule selected for this test is melamine, chosen for its demonstrated properties to bind the gold surface [138, 139]. The SERS signal of the analyte was measured under different leaning configurations reported in the schematic illustration in figure 4.3. In figure 4.3(a), the molecule solution is deposited on the substrate before the leaning of the nanowires thus the molecules are trapped in the tip-to-tip sites. The molecule solution can also be deposited after inducing the NWs to bend so that the molecules are placed just outside the tip-to-tip sites. The two configurations are called *post-leaning* and *pre-leaning*, respectively. The additional configuration with straight nanowires was measured.

between static fluids, like water and air, and relates it to the surface tension coefficient γ and the curvature radius R of the interface.

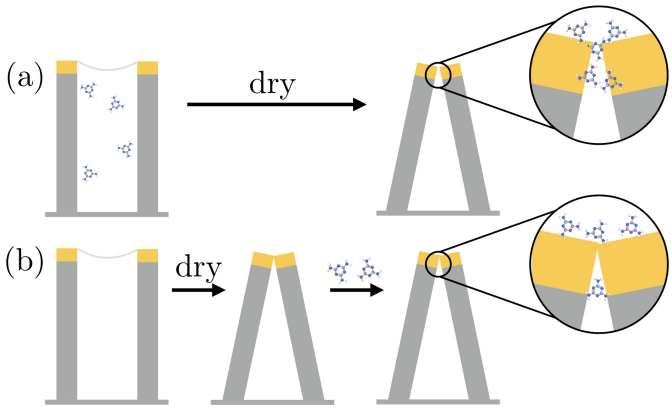

Figure 4.3: Schematic illustration of the two mechanical configurations exhibited by the gold-coated silicon nanowires. (a) The molecule solution can be deposited on the standing nanowires and it is dried in air thus inducing the bending of the NWs upon the evaporation of the water. In this way, the molecules are trapped in between the nanowires. This configuration is referred to as post-leaning. (b) Alternatively, the bending can be induced prior to the solution deposition thus the molecules are placed above and under the nanowires tips. This configuration is called pre-leaning. Figure adapted from reference 110.

The enhanced melamine spectra produced in these configurations, under the experimental conditions reported in section 3.3, are compared in figure 4.4. The normal Raman spectrum of melamine is reported in figure 4.4(a). The most intense peak at 676 cm^{-1} is assigned to the ring-breathing II mode, which involves the in-plane deformation of the triazine ring. The peak with the second largest intensity at 983 cm^{-1} arises from the ring-breathing mode I of the triazine ring [140]. The SERS spectra of melamine in figure 4.4(b)-(d) are dominated by the amine trigonal breathing mode which shifts at higher wavenumbers and splits into two main peaks at 680 cm^{-1} and 712 cm^{-1}, indicating that melamine is bound to the electropositive gold surface via the lone electron pair of ring nitrogen. The shift and the intensity ratio between the main peaks depend on the physicochemical interactions of melamine with the metallic nanostructures. Noteworthy splittings and shifts from the original melamine bands at 676 cm^{-1} were already reported in the literature using respectively Klarite SERS substrates [141], triangular gold nanoparticles [142], silver nanoparticles [140] and spherical gold nanoparticles [6]. It is reasonable to assume that an intense polarisation occurs at the surface of these metallic nanostructures, where the electric field increases strongly, and that it can result not only in a larger enhancement factor but also in a change of the vibrational Raman selection rules.

The spectra collected on the gold-coated SiNWs forming clusters are shown in figure 4.4(b)-(c) for post-leaning and pre-leaning configurations, respectively. The

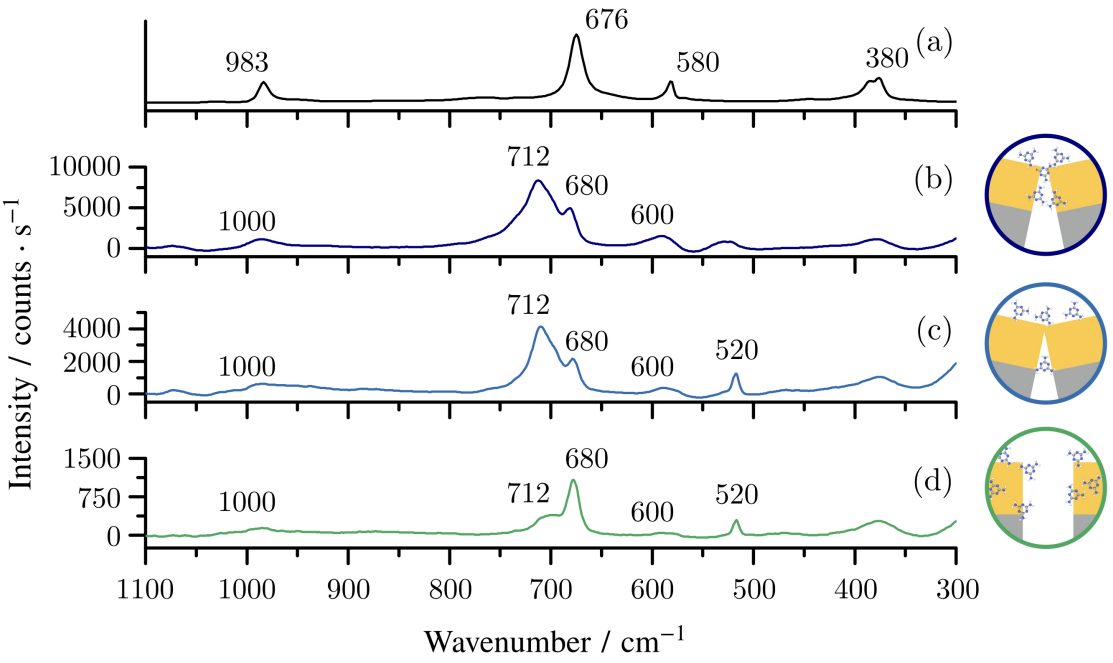

Figure 4.4: (a) Normal Raman reference spectrum of melamine. The Raman shifts are indicated above the main peaks in the spectral region between 300 cm^{-1} and 1100 cm^{-1}. The SERS spectra recorded after the deposition of a 1 µl droplet of a 100 $mg\,l^{-1}$ solution of melamine on the substrate with (b) leaning induced after the deposition of the molecule, (c) leaning induced prior to the deposition of the molecule and (d) no leaning induced. The small illustrations on the right depict the nanowires configuration for each spectrum.

molecules are adsorbed at the gold coated tips of the wires, in the gaps among the tips a strong local electromagnetic field is distributed leading to the formation of multiple hot spots. The result is a large enhancement of the melamine signal at 712 cm^{-1}, which reaches about 4000 counts/s for pre-leaned wires and 9000 counts/s for post-leaned wires. The first order of silicon at 520 cm^{-1} is clearly visible in the spectrum collected from the pre-leaning configuration but partially overlapped with a melamine peak for the post-leaned wires due to the substantial Raman enhancement. The spectrum reported in figure 4.4(d) is collected on the substrate with straight, non-leaning wires. It can be assumed that the analyte is adsorbed uniformly all over the gold-coated tips of the nanowires, leading to an enhancement of the Raman signal of the melamine. In particular, as reported by Wu et al. [143], when standing wires are present on the surface and the Raman excitation is provided by a 780 nm laser line, it could be inferred that a strong enhancement of the electric field occurs at the interface Au/SiNWs. In this configuration the ring-breathing II mode is dominated by the peak at 680 cm^{-1}, which reaches about 1000 counts/s with only a small shoulder at 712 cm^{-1}.

The results on the different configurations show that the most efficient configuration is post-leaning one where the Raman signal is more than two times larger with respect to the pre-leaning configuration and nine times larger than the one obtained with non-leaning nanowires. If the wires are brought to lean prior to the deposition of the analyte (pre-leaning) some potential hot spots and/or adsorption sites are forbidden to the analyte exposure. The result is in agreement with reference 113.

4.3 Distribution and density of the hot spots

The experiments in the previous section allowed to understand the location of the hot spots in the substrate constituted of gold-coated flexible silicon NWs. Moreover, it guaranteed the control of the mechanical properties of the nanostructures to select the molecule position at the hot-spots location. As already introduced in section 1.1.2, the hot spots are the regions of the substrate where the Raman signal enhancement is the largest. Strong discrepancies with the signal intensity in other regions of the substrate may arise leading to poor uniformity. SERS substrates owning large EF often show scarce uniformity and inconsistent sensitivity, on the other hand substrates with significant uniformity show limited enhancement [32]. One of the main focuses of the research on the development on SERS substrates is to control the location of the hot spots with homogeneous distribution to provide a favourable chemical detection level together with low variability across the substrate. Another remarkable parameter known to influence the SERS activity of the substrate is the density of the plasmonic nanostructures since, by increasing it, an increment in the number of hot spots is ultimately produced.

A further extension of the fabrication protocol of the flexible gold-coated SiNWs is required in the interest of achieving ordered distribution and high density of the SERS-active nanostructures over large area and thus of the hot spots forming in the bundles of nanowires. The employment of NSL as the first step of fabrication allows obtaining the high-density HCP arrangement of the nanostructures. The extent of the HCP configuration in NSL is limited by the appearance of defects during the self-assembly process. Typically the defects consist of nanospheres surrounded by 5 or 7 close neighbours instead of 6 and constitute breaks in the lattice symmetry bringing to the formation of various grains with different sizes, shapes and orientations. The presence of defects in the NSs monolayer has repercussions throughout the fabrication of the NWs. The direct consequence of the formation of such domains is an overall lower number of nanostructures per unit area and so a decrease of hot spots. To preserve both the homogeneity and the density, it is mandatory to improve the NSL step to increase the average size of the NSs domains in the monolayer.

The deposition of the NSs by spin coating constitutes a common approach and

some fabrication protocols have been proposed to increase the monolayer coverage area and to avoid defects in the six-fold coordination of NSs. However, the quantitative analysis of the effective long-range order is missing in the literature. In the work discussed hereafter, a systematic study on the degree of order of the NSs monolayer is presented. The parameter identified for the quantification of the long-range order is the correlation length ξ of the monolayer, evaluated by the image processing of SEM micrographs. The variation of the degree of order is achieved by influencing the rate of evaporation of water in which NSs are dispersed, thus the capillary forces bringing the NSs to self-assemble, by changing the spin coating conditions.

4.4 Maximisation of the degree of order

The mechanism of self-assembly of the NSs, discussed in section 2.1.2, is influenced by several factors, including the dispersion properties of the colloidal solution (i.e. weight fraction, solvent volatility and viscosity) [144] and the evaporation rate of the solvent in which the NSs are dispersed [67]. The dynamic conditions of spin coating, i.e. the rotational speed (ω) and the acceleration (α), can be modified to influence the evaporation of the solvent. This has a direct impact on the capillary forces among the nanoparticles [145] and ultimately on the efficiency of the self-assembly process.

In the interest of clarifying the relation between rotational speed and ξ, a set of samples was prepared by varying ω between 1000 rpm and 3500 rpm. The SEM micrographs for all the samples, as the ones in figure 4.5(a)-(f), were analysed to evaluate the topographical distribution of NSs and to extract the values of ξ. By setting a spinning speed of 1000 rpm, the formation of double layers of NSs can be observed in figure 4.5(a); it is worth to notice that the second layer is often ordered in a square close-packing. In this case, it is not possible to perform any further lithographic process, thus such deposition parameter can be discarded in the subsequent experiments. By increasing ω, the layer of NSs becomes more compact and the formation of a monolayer is reproduced in the range between $1250 \leq \omega \leq 2000$ rpm as shown in figure 4.5(b)-(d). On the other hand, in all the samples processed at $\omega \geq 2500$ rpm large portions of the surface are not covered by the NSs resulting in an unpacked layer shown in figure 4.5(e)-(f). From a practical point of view, the speeds between 1250 rpm and 2000 rpm are adequate to perform a subsequent ordered pattern-transfer process.

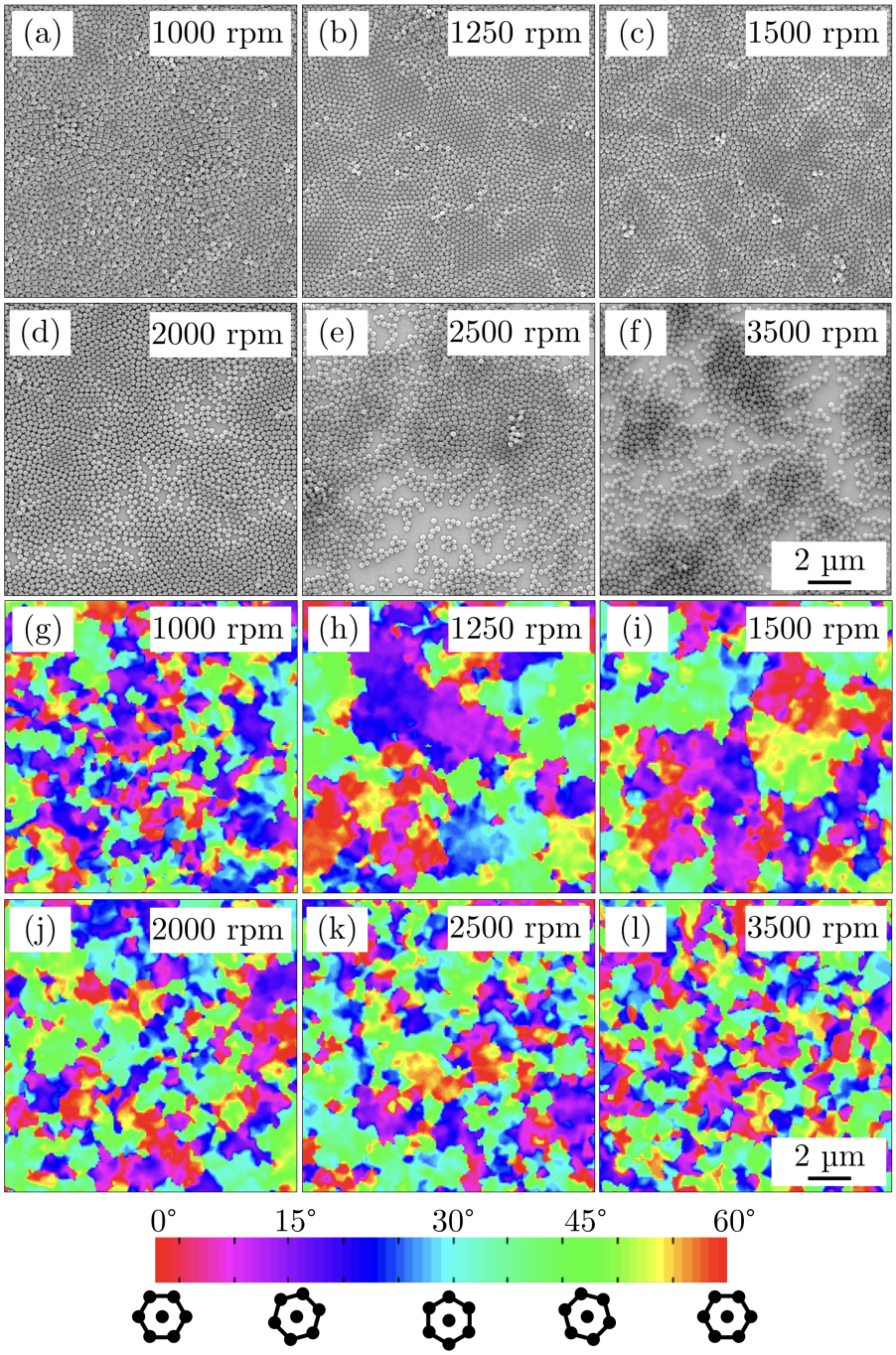

Figure 4.5: (a)-(f) SEM images of the colloidal crystal achieved by spin coating at different speeds ranging from 1000 rpm to 3500 rpm. (g)-(l) The colour maps corresponding to the SEM images obtained after the image processing by means of the Delaunay triangulation.

The quantitative analysis of the self-assembly of NSs layers is achieved by image

processing based on Delaunay triangulation of the SEM micrographs of the monolayer. The complete method is described in section 3.2. The colour maps in figure 4.5(g)-(l) are extracted from the SEM images above and represent the orientation of the grains. The resulting correlation function can be fitted producing a ξ value associated with each spinning speed. The long-range order of self-assembled NSs can be maximised by selecting the best deposition parameters with this procedure. Figure 4.6(a) displays the behaviour of ξ as a function of the rotational speed. The curve presents a monotonic decreasing trend with increasing spinning speed in the range of values $1250 \leq \omega \leq 3500$ rpm. For $\omega = 1250$ rpm, ξ reaches the maximum value of 1084 nm, while it drops to 339 nm for $\omega = 3500$ rpm. The error bars are obtained by calculating the standard deviation among ξ values extracted from different images for each substrate. The decrease of ξ to 1000 rpm can be associated with the presence of a second layer of NSs, as evident from figure 4.5(a). The value of ξ constitutes an indication of the ordering process and it can be considered representative of the whole sample. The formation of domains causes breaks in the periodicity of the lattice of NSs and each of these introduces a defective point in the triangulation. The number of defects in the HCP lattice was counted and the total percentage is reported in the graph in 4.6(b). The percentage of defects in the monolayer as a function of ω follows a complementary trend with respect to ξ. For $\omega = 3500$ rpm, the number of defects reaches 55 %, while for slower spin coating processes it decreases and presents a minimum value at the speed corresponding to the largest ξ.

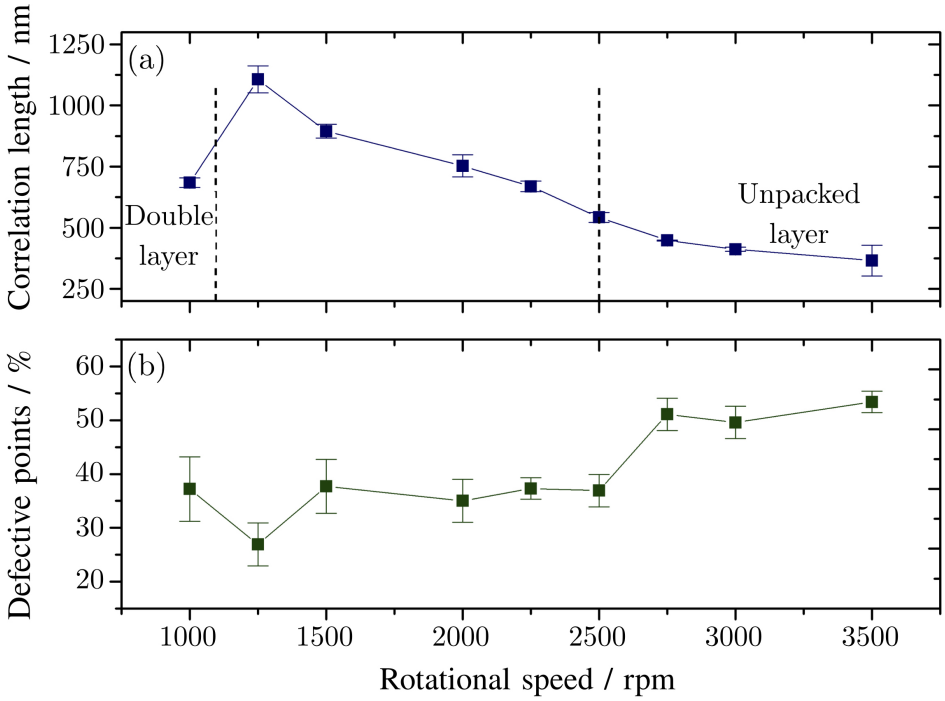

Figure 4.6: (a) The plot reports the monotonic decreasing trend of the correlation length ξ at different values of the rotational speed. The maximum distance at which the coherency of the HCP symmetry is maintained is 1084 nm found at 1250 rpm. (b) The graph shows the percentage number of defects in the six-fold coordination of the NSs monolayer, the scatter plot refers to the sum of less and more than six nearest neighbours to each particle.

The effect of various dynamic conditions of spin coating on the ordering of NSs can be better understood through the comparison to a different self-assembling system, such as the BCPs. The ordering of BCPs is influenced by the thermodynamic conditions during the thermal annealing process, i.e. time of annealing, temperature, heating and cooling ramp [146, 147]. It has been observed that raising the temperature during the annealing process and tuning other parameters leads to a process of reorganisation of adjacent domains with the annihilation of defects [148] to form larger and larger defect-free areas. Analogously, the effect of the rotational speed and acceleration during spin coating to which the NSs are subjected can be isolated by the previous analysis. By matching the graphs reported in figure 4.6, it is possible to point out that a slow spin coating deposition contributes to triggering the evaporation of the solvent at a proper rate to activate the capillary forces among NSs, resulting in the most correlated monolayer in the adopted experimental conditions. On the contrary, the centrifugal force prevails on other physical interactions at higher speeds spreading the nanoparticles on the substrate randomly. The optimal dynamic conditions are dependent on the diameter of the

NSs (in this case D = 250 nm), the use of bigger NSs is often described in the literature resulting in large domains easy to self-assemble [149]. Despite the significant interest for large area NSL and the use of ξ for the estimation of BCPs order, in the literature the degree of order of self-assembled NSs arrays has been evaluated only qualitatively rather than quantitatively, making it difficult to compare these results with previous works.

4.5 Ordering effect on the SERS response

Having determined the relation between the deposition parameters and ξ and optimised the fabrication protocol, it is possible to inspect the influence of the degree of order on the activity of the SERS substrate by completing the fabrication to obtain a two-dimensional array of gold-coated NWs distributed with different correlation lengths. Four samples with different ξ are selected to produce the ultimate substrate as described in section 3.1.2 and section 3.3.1.From this point on, these four samples will be referred to as NW1 (ξ = 1084 nm and ω = 1250 rpm), NW2 (ξ = 861 nm and ω = 1500 rpm), NW3 (ξ = 757 nm and ω = 2000 rpm) and NW4 (ξ = 339 nm and ω = 3500 rpm).

To test the SERS effect on the NWs, 7-mercapto-4-methylcoumarin was selected as probe molecule. After the incubation of the SERS substrates with MMC, the leaning of the nanowires was induced to obtain the most efficient configuration. The normal Raman spectrum of MMC in the solid state is shown in figure 4.7(a). The major vibrational peaks of the typical Raman fingerprint of pure MMC are due to the stretching mode of the -C-O- bond at 1169 cm^{-1}, to the conjugated -C=C- stretching mode at 1593 cm^{-1}, and to the -C-C- stretching and in-plane deformation of -C-$H_{(ring)}$ at 1543 cm^{-1}. The band assignments to all the peaks are listed in table 4.1 and were obtained by a combination of a computational procedure with vibrational information from reference 133 and 150.
Micro-Raman mapping was performed on the four chosen samples within an area of 0.5 mm^2 and repeated eight times over a total area of 4 mm^2. The spectra displayed in figure 4.7(b)-(e) represent the average among the signal detected in the eight mapped areas. Correspondingly, the chemical maps are obtained at 1593 cm^{-1} in a portion of the investigated area. The resulting spectra present the fingerprint of MMC consistently with its conventional Raman spectrum. The main characteristic peaks cited above are clearly visible in their SERS spectral counterparts. However, the relative intensities and Raman shifts slightly changed due to a typical effect seen in SERS, mostly due to the interactions of the analyte with the gold surface, in particular to the orientation of analyte molecules on the substrate and their specific functional groups bound to the substrate [151]. A significant decrease of the intensity was observed in the SERS spectra for the peaks at 438 cm^{-1}, 1169 cm^{-1} and 1544 cm^{-1} shifted to 443 cm^{-1}, 1171 cm^{-1} and 1539 cm^{-1}, respectively.

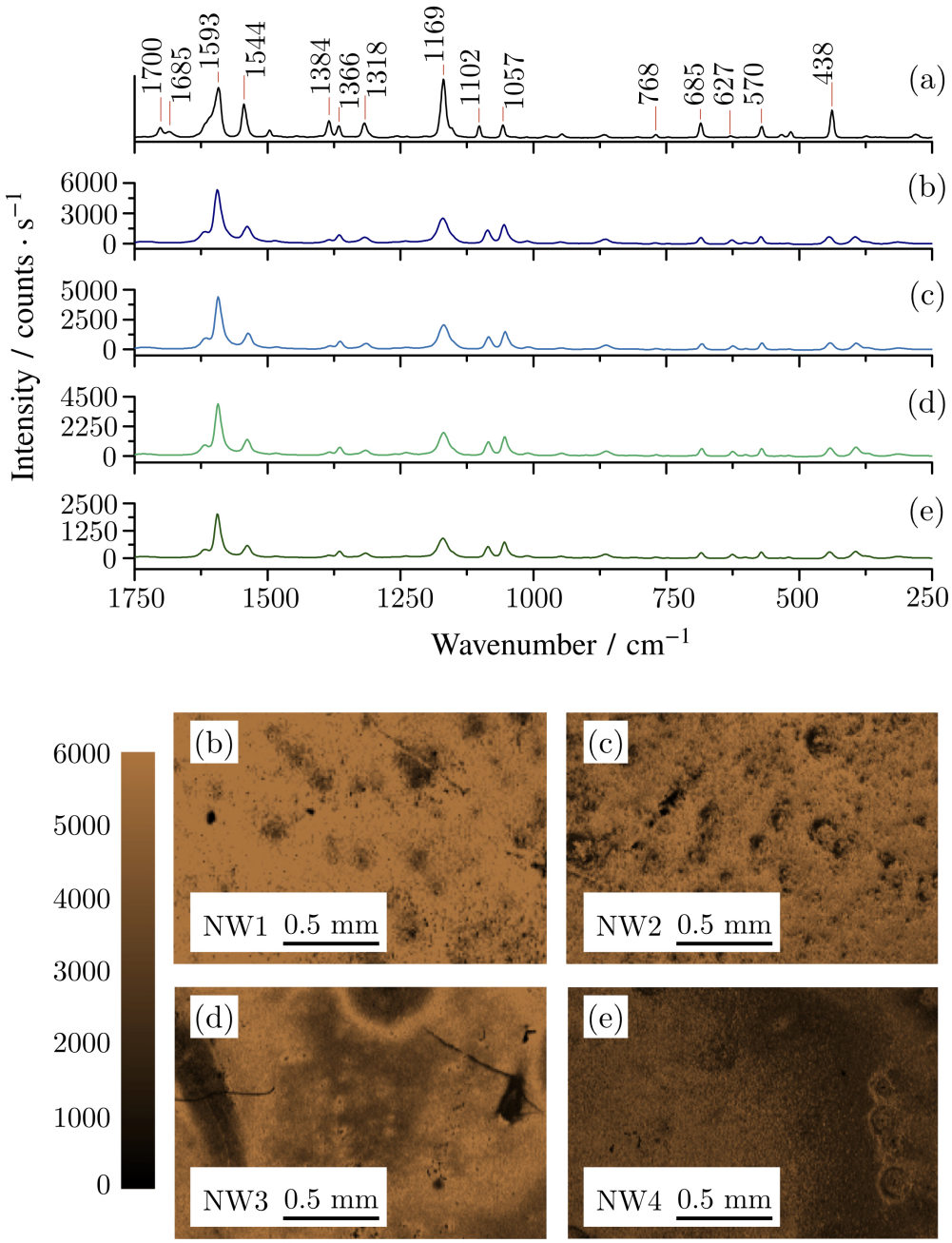

Figure 4.7: (a) Normal Raman spectrum of the probe molecule 7-mercapto-4-methylcoumarin (MMC). The Raman shifts are indicated above the main peaks in the spectrum and the corresponding assignments are reported in table 4.1. The average SERS spectra of MMC and the corresponding chemical maps at 1593 cm^{-1} are reported for the tested substrate (b) NW1, (c) NW2, (d) NW3 and (d) NW4.

The intensity of the main vibrational peak at 1593 cm^{-1} can be used to compare

Raman shift (cm^{-1})	Assignment
438	Skeletal vibration
570	Ring vibration
685	Skeletal vibration
1057	Characteristic ring vibration
1102	Characteristic ring vibration
1169	-C-O- str
1318	-C-O- str.
1366	Conjugated -C=C- asym. str.
1384	-C-H_3 def.
1543	-C-C- str. and -C-$H_{(ring)}$ in-plane deformation
1593	Conjugated -C=C- sym. str.

Table 4.1: Band assignments to the Raman fingerprint of the MMC shown in figure 4.7(a).

the enhancement provided by different substrates. The scatter plot in figure 4.8 reports the intensity values for the four substrates against the correlation length ξ of the original monolayer of NSs. It is easy to observe that the enhancing capability of the substrates is improved by the degree of order of the nanostructures; the intensity is enhanced up to 5300 counts/s in the substrate NW1 with the largest ξ and it progressively decreases for lower ξ reaching below half of the first value for substrate NW4. The error bars are calculated as the relative standard deviation of the repeated measurements. One of the reasons to motivate such trend is that the number of NWs per unit area increases coherently to the degree of order due to the HCP symmetry of the nanostructures. Consequently, there is an increase in the number of hot spots. However, the density alone is not enough to explain the trend seen in figure 4.8.

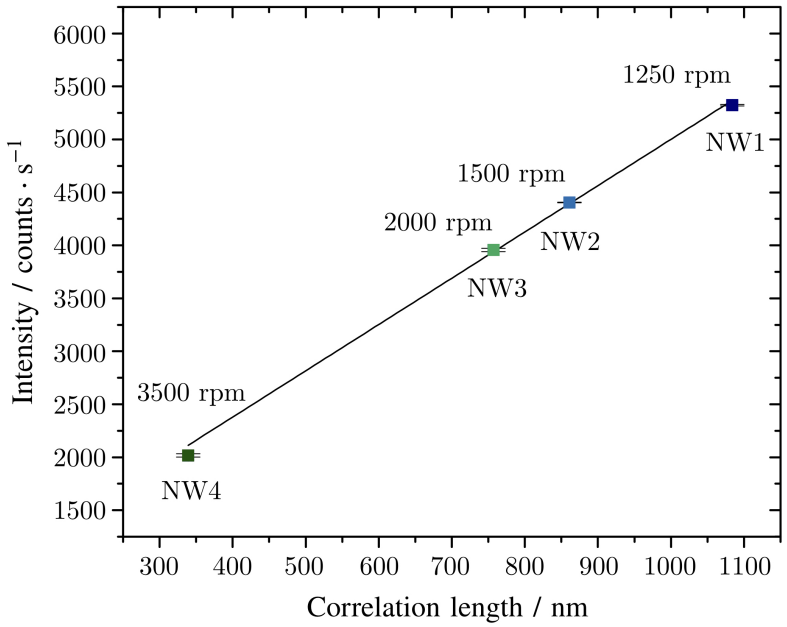

Figure 4.8: Scatter plot of the average intensity of the SERS signal of MMC at 1593 cm^{-1} as a function of the correlation length ξ detected on the four characterised substrates.

The morphology of the hot spots has been investigated in the area of analysis through correlative microscopy by matching the SERS maps to the SEM analysis, as reported in figure 4.9(a) showing a low-magnification view of the substrate NW1. The coloured squares in the image highlight the areas in which high-magnification SEM micrographs were acquired. The SEM image in figure 4.9(b) shows the morphology of the SERS-active nanowires in the area corresponding to the largest enhancement on the substrate. The leaning nanowires are arranged in groups of two to five nanowires. This configuration is prevalent in the substrate NW1 and, in agreement with reference 130, it produces a large enhancement of the electromagnetic field in proximity to the hot spot. The presence of defects within the same substrate may cause the nanowires to arrange in larger groups, as in figure 4.9(c), thus producing a lower enhancement. The images in figure 4.10(a)-(d) show a comparison of the arrangement of the nanowires in the different substrates after the probe molecule deposition. The formation of small groups of NWs prevails in substrate NW1, while the NWs bending configuration in substrates NW2 and NW3 is dominated by the formation of larger and irregular bundles leading to a lower enhancement of the SERS intensity. The nanowires in substrate NW4 present a disordered configuration and random leaning of the nanostructures.

The degree of order, measured through the correlation length ξ, strongly conditions the formation of bundles of nanowires. The relevance of the degree of order ξ is further highlighted by the graph in figure 4.11, where the percentage reduction

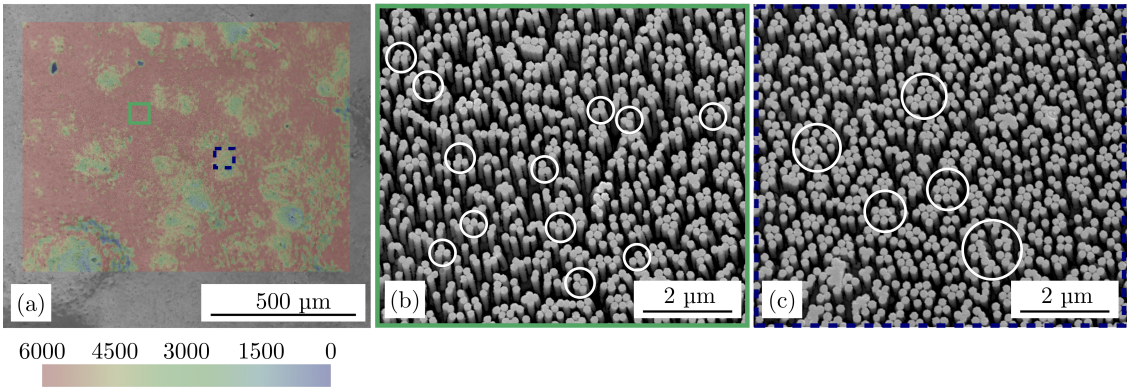

Figure 4.9: (a) Correlative microscopy image obtained combining the low-magnification SEM micrograph of substrate NW1 to the corresponding Raman map. (b)-(c) High-magnification SEM micrographs acquired in regions corresponding to different enhancement of the signal. The white circles highlight the arrangement of the nanowires forming bundles.

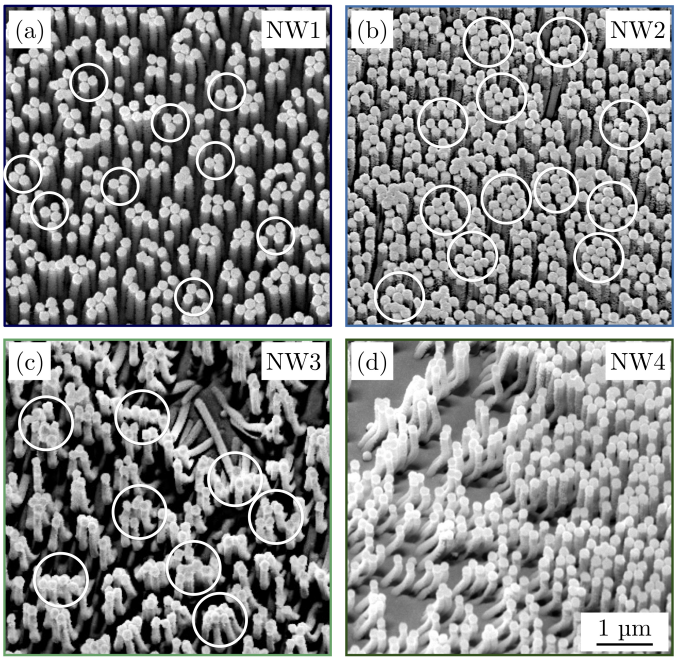

Figure 4.10: SEM micrographs acquired on the four characterised substrates (a) NW1, (b) NW2, (c) NW3 and (d) NW4. The white circles highlight the disposition of the nanowires after the deposition of the probe molecule and the formation of bundles. The number of nanowires involved in each bundle influences the efficiency of the signal enhancement.

of the SERS signal, of ξ and of the NWs density are plotted for each sample as a function of the spinning speed. A strong agreement between the data sets for the

SERS signal and ξ is evident. Thus the correlation length can be identified as a fundamental and easy-to-measure parameter influencing both the density and the NWs bending arrangement and playing a key role in the SERS signal enhancement.

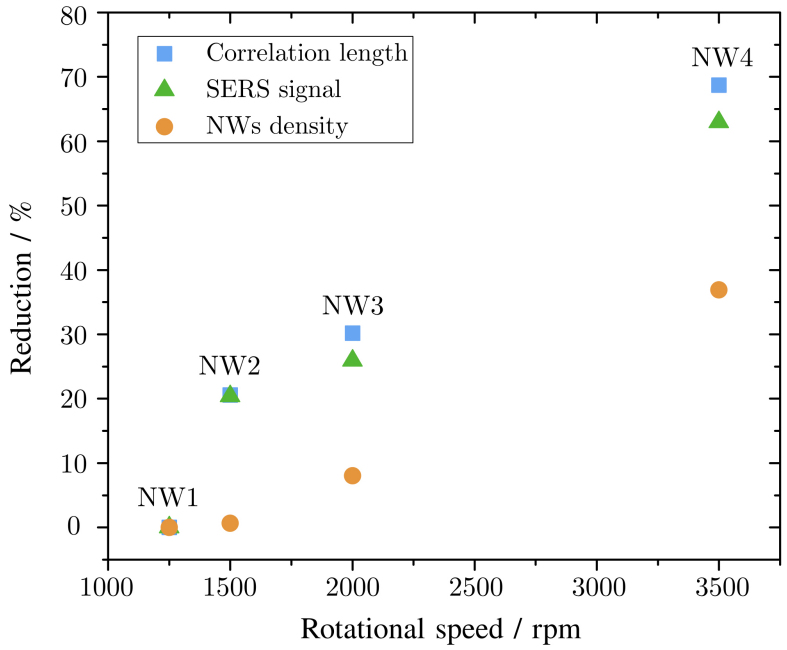

Figure 4.11: The scatter plot presents the percentage reduction of the correlation length, the NWs density (nanowires/µm^2) and the intensity of the SERS signal of MMC as a function of the rotational speed. This datum is reported for the four substrates and each data set is normalised to the value measured on NW1.

The results reported in this chapter confirm that tailoring the fabrication protocol allows to control remarkable parameter to provide SERS substrates with good enhancement. Optimising the aspect ratio of the plasmonic nanostructures and their long-range order was proved fundamental to control the location of the hot spots on the substrate, the positioning of the molecules inside these regions, and to have an homogeneous distribution of hot spots with high density.

Chapter 5

SERS substrate characterisation and application to analytical chemistry

The work presented in this chapter is dedicated to the characterisation of the SERS substrate performance in terms of the homogeneity across large area and the enhancement factor of the Raman signal on the sample with the highest degree of order. Moreover, the need to obtain a reliable EF value motivates the development of a possible procedure for a trustworthy estimation of the number of molecules probed by the laser during the SERS measurement. The discussed technique to achieve this task is synchrotron-based reference-free X-ray fluorescence, with the possibility to expand it to different laboratory environments and sample systems. The SERS substrates are also proved to give a promising contribution to analytical chemistry; the use of model molecules, such as food contaminants, is exploited at different concentrations. The performance of the most ordered substrate in this study is characterised in terms of the homogeneity across large area in section 5.1 and the enhancement factor in section 5.2. The results of the XRF characterisation are presented in section 5.3. The results of the characterisation of the SERS substrate in terms of the sensitivity level of detection are reported in section 5.4.

The content of this chapter and part of its text are reported in two articles published by the author of this dissertation in references 125 and 136.

5.1 Homogeneity of the signal

The uniformity of SERS response over an active substrate is a crucial aspect in view of applications to analytical chemistry. In order to evaluate it, one can take into account the variability of the signal across the substrate through the relative standard deviation (RSD). The RSD is widely adopted in the SERS community to

assess the spatial homogeneity of a substrate. Lower RSD values imply remarkable homogeneity [152, 153] and values as low as 3% have been recently reported pushing the homogeneity to outstanding levels [27]. Even though these figures are quite appealing, it is worth considering that a detailed comparison is hindered by the fact that the practical calculation does not result from a standard protocol and every group reports its own methodology. In some cases the RSD is calculated by considering the mean among tens to thousands punctual spectra [154, 155], while in other cases it is obtained from multiple scanning areas within a larger area on the substrate [156, 157]. In some papers, the scanning area onto which the analysis has been carried out is not reported clearly [143, 158] leading to ambiguity in the results. For the purpose of defining the SERS substrates homogeneity rigorously, here is a suggestion to extend the analysis to greater portions of the substrate and declare the analysed area unequivocally.

One interesting parameter to be considered is the intra-map homogeneity, which is well described by the RSD calculated on all the spectra composing the Raman map. In other words, it represents the variability from pixel to pixel within a single map. As long as the scanned area is enlarged, the response variability of different sites increases, leading to a higher RSD value.

However, satisfactory repeatability of the measurements can be obtained by increasing the spot-size of analysis, in this way local differences are averaged. In punctual confocal Raman, the spot size is constant and it depends on the section of the focalised laser on the investigated surface (2.7 µm for 780 nm laser and 10x objective), however a spot-size enlargement can be practically obtained collecting spectra on a wider area and averaging all of them. In this way, the point-to-point intensity differences due to local defects can be overcome. The resulting mean spectrum is representative for the whole mapped area. In this concern, a relevant piece of information is the minimum area that guarantees adequate repeatability. The inter-maps RSD, i.e. the RSD of repeated measurements of equal area on the same SERS substrate, is considered to evaluate the latter. A similar approach is used by Giorgis et al. [159] and Fu et al. [156]. For this scope, the calculation of the RSDs was performed by elaborating the SERS spectra acquired over progressively increasing areas from 150×150 µm^2 to 2000×2000 µm^2. The chemical map, shown in figure 5.1, is built over the maximum area of analysis around the band at 1593 cm^{-1}. For each map dimension, four different regions of the substrate were scanned and the number of spectra included in the analysis is reported as well as the intra-map and inter-maps RSDs. The results and details of this analysis are specified in table 5.1.

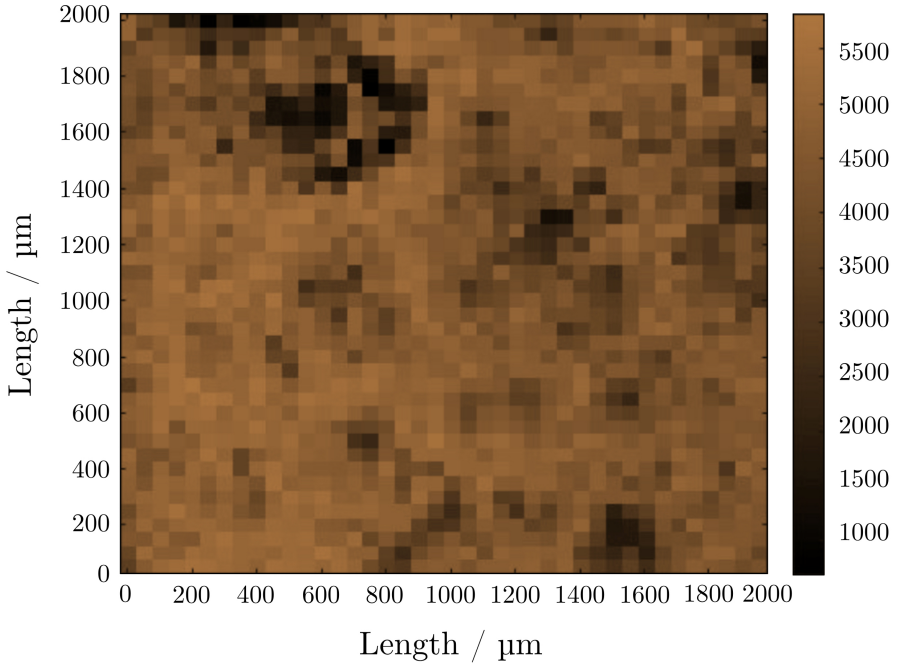

Figure 5.1: The chemical map represents the intensity of the band at 1593 cm^{-1}. It is built over the maximum area of analysis of $(2000 \times 2000)\mu m^2$ on substrate NW1 to evaluate the surface homogeneity and it is acquired with a step size of 50 µm.

Scanned area (μm^2)	Number of spectra	Intra-map RSD (%) [a]	Inter-maps RSD (%) [b]
150×150	9	12.1	12.8
300×300	36	16.4	13.6
450×450	81	16.2	10.7
600×600	144	17.4	8.0
750×750	225	18.1	7.3
900×900	324	17.9	6.8
1000×1000	400	18.1	6.6
2000×2000	1600	20	–

[a] The intra-map RSD is the RSD calculated upon all the spectra composing one Raman map, the reported values are the mean of 4 determinations.
[b] The inter-maps RSD is the RSD calculated upon the four intensity averages for each map.

Table 5.1: Values of relative standard deviation for different areas to study the substrate homogeneity.

The value of the intra-map RSD was found to be 12.1 % over the smallest scanning area and a growth up to 20 % is registered for the maximum area of

investigation. It is commonly accepted that RSD values around 20% indicate a fair grade of homogeneity in SERS detection [157, 143, 160]. On the other hand, the particularly interesting aspect is that the values of the inter-maps RSD decrease when the scanning area is enlarged. The inter-maps RSD remains around 13 % for small areas, while it reaches values lower than 10 % when the analysis is carried out over $500 \times 500\ \mu m^2$. The result of about 13 % for the intra-map and inter-maps RSD over $150 \times 150\ \mu m^2$ revealed an appreciable homogeneity level of the SERS substrate and the repeatability expressed by the inter-maps RSD values is a remarkable result. Moreover, this outcome constitutes an encouraging step forward in comparison to the homogeneity levels of 20 % for substrates with leaning nanowires as declared by Lin et al. [27] over a scanning area of $100\ \mu m^2$.

5.2 Enhancement factor

To evaluate the performance of the most ordered substrate NW1 in terms of signal enhancement, the EF was calculated according to the method proposed in reference 26 using the MMC mode at $1593\ cm^{-1}$ and the formula in equation 1.2 reported hereafter for simplicity:

$$EF = \frac{I_{SERS}/N_{surf}}{I_{RS}/N_{vol}}.$$

First of all, the laser-probe interaction volume was determined using a 20× long working distance (LWD) objective, with aperture number (NA) equal to 0.4. It is measured by placing the SERS substrate in the focus plane and then moving the substrate out of the focus plane in increments of 2 µm. The Raman intensity at $1593\ cm^{-1}$ for each position along the z-axis was integrated and normalised to the maximum intensity at the focus plane, where the laser spot diameter was 1.9 µm. The probe volume is modelled as an ellipsoid with two axes equal to the laser focus-spot diameter and the height equal to the effective probe depth. Thus, the interaction volume was measured to be $67.8\ \mu m^3$.

The value of $I_{SERS} = (67.5 \pm 3.2) \cdot 10^3$ counts/s for the $1593\ cm^{-1}$ peak was measured on sample NW1 in the same conditions used for the determination of the laser-probe interaction volume. To calculate the intensity of the Raman signal in non-SERS conditions and the number of molecules contributing to it, the measurement was performed on a liquid sample[1], an ethanol solution of MMC at known concentration 0.01 M. The intensity of the peak at $1593\ cm^{-1}$ was measured $I_{RS} = (5.2 \pm 0.3)$ counts/s. The number of molecules contained in the laser-probe

[1]No Raman signal of the MMC was collected on a gold flat substrate due to the low sensitivity of the normal Raman in the detection of an organic monolayer.

interaction volume and responsible for the normal Raman signal was calculated to be $N_{\text{vol}} = (4.1 \pm 0.2) \cdot 10^8$ through the solution concentration.

The number of molecules contributing to the SERS signal N_{surf} was estimated under the premise that the main contribution to the SERS signal, and thus to the enhancement factor, is imputable to the molecules adsorbed inside the hot spots at the tips of the NWs in agreement with references 110 and 113. For this evaluation, the dimension of the probed surface area is required and thus of the NWs topography. The number of nanowires per unit area was measured with the same image processing tool used for Delaunay triangulation and its value is $14.8\,\mu\text{m}^{-2}$ on sample NW1. By considering the laser spot diameter of 1.9 µm, it was possible to estimate the number of NWs included in the laser spot area as 41.9 wires. Moreover, the SEM measurements of the NWs dimensions were conducted by using a metrological dimensional standard[2] and the effective surface area of the tips probed by the laser was estimated[3] to be $A_{\text{surf}} = (2.4 \pm 0.4)\ \mu\text{m}^2$. The assessment of the number of molecules adsorbed on this surface area required some geometrical considerations concerning the area occupied by a single molecule. Given the molar volume of MMC divided by the Avogadro number, the volume occupied by a spherical molecule was obtained and consequently the area of its circular projection was estimated to be equal to $(6.90 \pm 0.09) \cdot 10^{-7}\ \mu\text{m}^2$. Knowing the total surface area and the area occupied by a single molecule and assuming the MMC to be distributed with a monolayer coverage in the hot-spot regions, the number of molecules was calculated to be $N_{\text{surf}} = (3.5 \pm 0.6) \cdot 10^6$.

Using the quantities estimated so far, the value of the enhancement factor on sample NW1 comes to

$$EF_{NW_1} = (1.5 \pm 0.3) \cdot 10^6,$$

in the same order of magnitude of the one reported in reference 113 on silver coated silicon nanopillars substrate. The uncertainty associated to the EF is calculated

[2]The calibration of the SEM magnification is of utmost importance when length measurements are required. The length scale can change at different magnification and working distance and it can shift over time. The standard procedure for the SEM calibration requires to use the proper calibration feature size depending on the selected magnification. The sample selected for calibration is constituted of self-assembled PS-b-PMMA BCPs arranged in vertically-aligned cylinders with the lateral centre-to-centre distance $L_{0\text{calib}} = (28.1 \pm 0.5)$ nm measured by metrological AFM [161]. Both the calibration sample and the silicon nanowires substrate were observed by fixing the working distance to 10 mm and the magnification to 160 000. The measurement of the diameter of the NWs D_{meas} is corrected by means of the measured and calibrated value of L_0 as follows:

$$\text{D}_{\text{calib}} = \text{D}_{\text{meas}} \cdot \frac{L_{0\text{calib}}}{L_{0\text{meas}}}.$$

[3]The gold surface area was estimated by approximating the gold cap to a smooth cylinder.

by the standard propagation of uncertainties for independent variables. The relative uncertainties related to the SERS I_{SERS} and Raman I_{RS} punctual intensity measurements are given by the instrumental sensitivity of 5 %. The relative uncertainty on the N_{vol} of 6 % comes from the uncertainty on the solution concentration and on the scattering volume. The largest contribution to the total EF uncertainty is given by the estimation of the number of molecules N_{surf} based on geometrical reasoning.

The EF calculated with the equation 1.2 provides the average SERS enhancement of the substrate, its critical aspects are discussed in the supplementary information of reference 26. Particular interest is addressed to the difficulties in the evaluation of the number of molecules, provided that a monolayer coverage (or lower) is granted. These are related to the estimation of the metallic surface area in a complex three-dimensional topography and of the molecule surface density, which could introduce artificial variations of the EF up to two orders of magnitude [26]. Some papers report the use of alternative factors to classify the SERS substrate when the morphology complicates the scrupulous determination of the amount of adsorbed molecules [159].

5.3 Molecule quantification by X-ray fluorescence

The importance of using a univocal definition of the EF and of determining the number of molecules contributing to the SERS signal is constantly remarked in conferences and scientific discussions. In the conclusive remarks of the Faraday discussion 2006 on SERS [25], it is stated that the correct evaluation of the EF should rely on the unambiguous knowledge of the number of SERS-active molecules residing in the laser beam. In order to standardise the evaluation of the substrate by the EF, multiple tools should be brought together to address the mentioned issues.

The calculation of the EF, as reported in section 5.2 for the sample NW1, is based on the estimation of the number of molecules N_{surf} by means of some geometrical assumptions on the volume occupied by the molecules and the surface area excited by the laser. Several examples in literature rely on analogous geometrical approaches [162, 113, 110]. Even the use of the formula for SSEF (see equation 1.3) in some other papers still carries some vagueness regarding the determination of the molecules surface density and metallic surface area[27, 155]. The EF calculation could be strengthened by a quantitative and reliable assessment of the number N_{surf}. In the interest of proposing a method to achieve this goal, a metrological study was performed through a synchrotron-based reference-free approach to X-ray fluorescence for quantitative analysis. In the particular case presented in this section, the XRF analysis was performed on the SiNWs substrate NW1 coated with

the SERS analyte. Sulphur was chosen to be the target element of the quantification in order to relate its amount in the sample to the total number of SERS probe molecules, since it is contained in the ratio 1:1 in each MMC molecule ($C_{10}H_8O_2S$).

5.3.1 Basic principles of X-ray fluorescence

X-ray fluorescence is a physical phenomenon consisting of the emission of characteristic secondary X-rays from a material excited with high-energy X-rays. A scheme of this phenomenon is depicted in figure 5.2. In figure 5.2(a) the incoming X-ray photons, with sufficient energy to ionise the atom, induce the ejection of the electrons from the core orbital (K shell in the X-ray notation). The electrons leave some vacancies behind, thus bringing the atom to an unstable condition and inducing the recombination with electrons from higher orbitals. If a radiative recombination occurs, the emitted photon possesses the energy of the difference between the electronic states involved in the transition, as shown in figure 5.2(b) for sulphur. The fluorescent transition from the L shell to the K shell produces the Kα emission line, while the transition from the M shell to the K shell results in the Kβ emission line. In a more accurate representation of the Bohr model, other multiple transitions are possible and the energy value of each emitted photon is a characteristic and tabulated value identifying the atomic species. The photons are counted by a detector producing a signal with magnitude proportional to the occurrence of each particular transition and related to the abundance of the element in the sample. For these reasons, XRF is a well-established and powerful tool for non-destructive characterisation of virtually any material for different purposes, such as determination of the elemental composition, layer thicknesses, mass quantification and contamination.

The quantification is usually traced to calibration standards and reference materials with known elemental composition. The quantitative determination of the amount of sulphur can be carried out with a *reference-free* approach to X-ray fluorescence developed by PTB X-ray spectrometry group, meaning that reference measurements on a similar substrate become unnecessary. Reference-free quantification requires the a priori knowledge of the atomic fundamental parameters of the elements in the specimen as well as of the relevant experimental parameters. PTB's beamline is fully characterised with monochromatic excitation radiation and radiometrically calibrated detector and photodiodes for a traceable non-destructive investigation of the specimen [163].

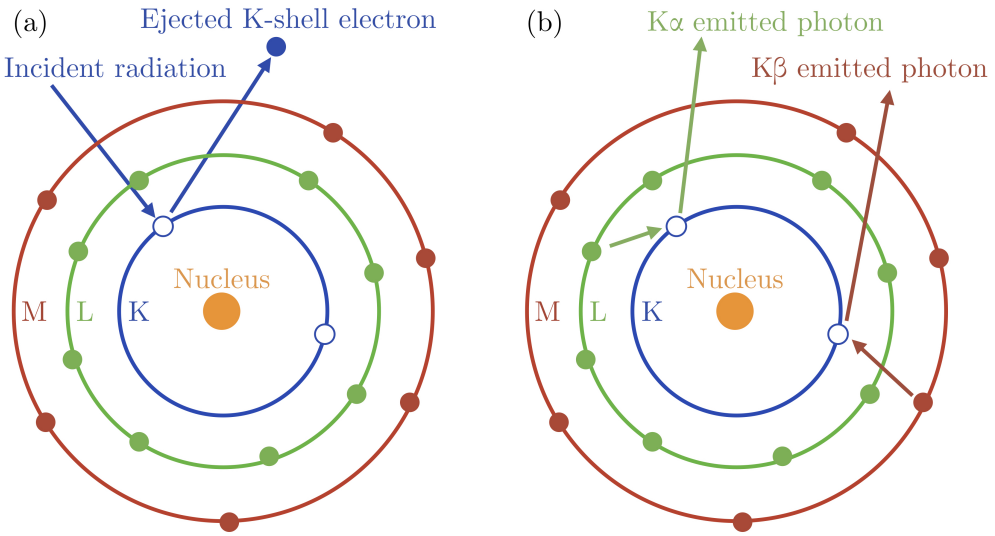

Figure 5.2: Simplified Bohr model of the sulphur atom S ($[\mathrm{Ne}]\,3\mathrm{s}^2\,3\mathrm{p}^4$) in which the nucleus and the atomic orbitals, labelled in the X-ray notation, are shown. (a) The incident X-ray beam ionises the atom by exciting an electron in the K shell. (b) The vacancy in the K shell can be filled by an electron either from the L shell or from the M shell leading to the emission lines Kα and Kβ, respectively. The energy of the emitted X-ray photon is equal to the difference between the energy of the initial and final electronic levels of the transition.

5.3.2 Quantification of sulphur through reference-free XRF

A simple descriptive scheme of the measurement on the gold-coated SiNWs is shown in figure 5.3, where the X-ray beam hits the surface at 45°. The angle of incidence was changed during the measurement from 27.5° to 45° with step of 0.5° by means of the alignment system described in section 3.4.1. Given the incidence configuration, the X-ray beam excites the atoms distributed on the whole surface of the nanowires. The fluorescence signal emission occurs in a cone-shaped volume, which is detected with an energy-dependent efficiency.

The specimens subject to XRF were sample NW1 after the SERS analysis and a nominally identical sample without MMC ($\mathrm{NW_{bg}}$), used to calculate the background quantity of sulphur present on the substrate prior to the MMC deposition. The recorded fluorescence spectra at all incident angles were deconvoluted using the known detector response functions for the relevant fluorescence lines [164]. The deconvolution algorithm, developed by PTB X-ray spectrometry group, is implemented in IDL and leads to the extraction of the photon counts for the fluorescence lines of the elements in the specimen. The elemental contribution included in the deconvolution were the fluorescence lines from sulphur S-Kα and S-Kβ as well as other lines from organic residues and elements in the molecule C-Kα and O-Kα.

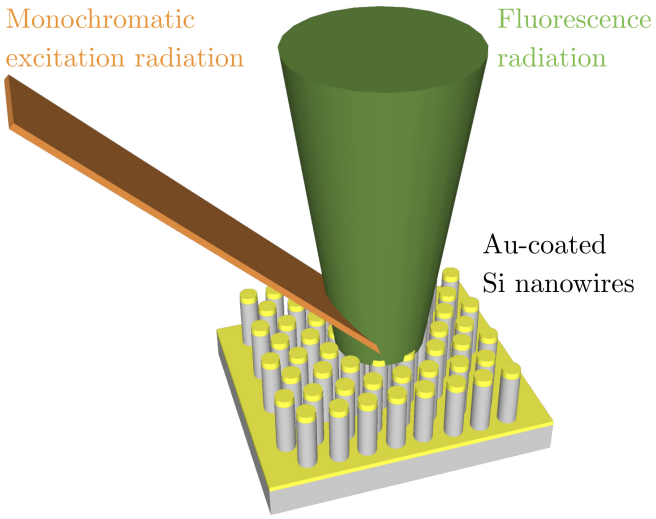

Figure 5.3: Scheme of the gold-coated SiNWs substrate probed with the 2.5 keV beam forming a 45° angle with the surface.

Moreover, the lines from the silicon substrate Si-Ll, Si-Kα and Si-Kβ were included together with the contribution from some contaminants such as nitrogen, fluorine, sodium, magnesium and phosphorus.

The obtained photon counts for each elemental line were normalised to the experimental parameters included in the normalisation factor N in equation 5.1. This includes the incident photon flux f_0, the solid angle of detection $\Omega/4\pi$, the detector lifetime LT and the correction for the offset angle θ_0, previously determined in section 3.4.1. The normalisation factor is an adimensional term whose value depends on the angle of incidence, this varies from 4.55×10^{-9} at 27.5° to 6.98×10^{-9} at 45°.

$$N = \frac{\sin(\theta - \theta_0)}{f_0 \cdot \Omega/4\pi \cdot LT} \tag{5.1}$$

The normalised photon count of the S-K fluorescence line ($P_{\mathrm{S,K}} = P_{\mathrm{S,K}\alpha} + P_{\mathrm{S,K}\beta}$) averaged over the angular interval of the measurement can be related to the amount of sulphur present on the sample. The value should be corrected by the instrumental parameter concerning the efficiency of the radiometrically calibrated detector at the energy of the S-K fluorescence line $\epsilon(E_{\mathrm{S,K}})$. Moreover, relevant fundamental atomic parameters should be used to allow the physical modeling of the characteristic X-ray fluorescence radiation emitted by the sample. The partial photoionisation cross-section is required for the K shell of sulphur at the energy of the incoming photons $\tau_{\mathrm{S,K}}(E_0)$, it gives the probability that the adsorbed photon produces an inner-shell ionisation and is expressed in $\mathrm{cm^2\,g^{-1}}$. In addition, the probability of radiative

de-excitation, i.e. fluorescence yield, is required for sulphur K shell $\omega_{S,K}$.

By means of the knowledge on the instrumental parameters and atomic constants, the element-specific fluorescence radiation allows to determine the mass of sulphur per unit area m_S/A as shown in equation 5.2:

$$\frac{m_S}{A} = N \cdot P_{S,K} \cdot \frac{1}{\tau_{S,K}(E_0) \cdot \omega_{S,K} \cdot \epsilon(E_{S,K})}. \tag{5.2}$$

The values of such atomic fundamental parameters were extracted from the xraylib repository [165], $\tau_{S,K}(E_0) = 1901.26\,\mathrm{cm^2\,g^{-1}}$ and $\omega_{S,K} = 0.080\,38$. The detector efficiency $\epsilon(E_{S,K})$ is around 0.9883.

The value of the $\frac{m_S}{A}$ on the sample NW1 is $(3.9 \pm 0.5) \cdot 10^{-7}\mathrm{g\,cm^{-2}}$ and the background content of sulphur in the analogous sample $\mathrm{NW_{bg}}$ is $(0.66 \pm 0.08) \cdot 10^{-7}\mathrm{g\,cm^{-2}}$. The uncertainties associated to the measurements were calculated through the standard propagation of uncertainty and the major components included in the budget are 10% uncertainty on the fluorescence yield $\omega_{S,K}$ and 5% due to the spectral deconvolution [135]. Other smaller contributions to the total uncertainty comprise 4% from the calculation of the effective solid angle, 3% relative standard deviation on the calculation of the average of the photon counts $P_{S,K}$, 2.5% from the S-K photon counts and 2% instrumental uncertainty. The computation of the total relative uncertainty produced a value of 12.7%. The amount of sulphur per unit area that is ascribable to the SERS analytes is given by the difference between the two terms from sample NW1 and sample $\mathrm{NW_{bg}}$:

$$m_{S_{MMC}}/A = (3.3 \pm 0.5) \cdot 10^{-7}\mathrm{g\,cm^{-2}}.$$

The number of probe molecules present of the gold-coated nanostructures can be discerned by means of the surface density of MMC, contained in the parentheses in equation 5.3, multiplied by the surface area of interest A_{surf}:

$$N_{surf} = \left(\frac{m_{S_{MMC}}}{A} \cdot \frac{N_A}{w_S}\right) \cdot A_{surf}. \tag{5.3}$$

The surface density of MMC is obtained by multiplying $m_{S_{MMC}}/A$ to the total number of atoms per unit mass. The latter is expressed by means of the ratio between the Avogadro number N_A and the atomic weight of sulphur $w_S = w_{MMC} \cdot f_S$, where w_{MMC} is the molecular weight of MMC and f_S is the weight fraction of sulphur.

By considering the probed surface area delimited by the laser spot is taken equal to $A_{surf} = (2.4 \pm 0.4) \cdot 10^6\ \mathrm{nm^2}$ in section 5.2, the number of molecular units estimated on the SERS substrate NW1 is estimated:

$$N_{surf} = (1.5 \pm 0.3) \cdot 10^8\ \text{molecules}.$$

The obtained value is 40 times larger than the one found by geometrical reasoning in section 5.2. The quantities used for the calculation of the number N_{surf} all contribute to the uncertainty, except for the Avogadro number, which is fixed exactly

to the constant value $6.02214076 \cdot 10^{23}\text{mol}^{-1}$, and the atomic weight of sulphur, which was selected from IUPAC reference value without an uncertainty [166]. The major component of the uncertainty is carried by the surface area.

It is possible to attain a new evaluation of the enhancement factor on the substrate, considering that it is sustained by a reliable quantification measurement:

$$EF_{NW_1} = (3.5 \pm 0.8) \cdot 10^4.$$

This value indicates that the evaluation of the number of molecules through geometrical reasoning produced an overestimation of the enhancement factor. The absolute value of EF is often provided as a parameter to evaluate and compare the performances of SERS substrates. However, the detailed indication on the method of calculation are repeatedly left out of scientific publications together with the many assumptions to evaluate the number of molecules contributing to the SERS signal and the surface area. This hinders the comparison of the EF among different substrates. The value of the EF, obtained through the measurement of the amount of analytes by X-ray spectrometry method with calibrated instrumentation and physical traceability to the SI, is to be considered more accurate and close to its true value. Despite the fact that this technique relies on the extremely specialised synchrotron radiation facility with radiometrically calibrated instrumentation present at PTB beamline in BESSY II, it could be extended to laboratory instrumentation and it can become a candidate technique contributing to solve the problem of accurate molecule quantification.

5.4 Sensitivity of analyte detection

The performances of gold-coated flexible SiNWs as SERS substrate were further characterised in terms of the dynamic range of detection to obtain a calibration curve for the analyte quantification and to determine the detection and quantification limits. For this purpose, melamine was used as probe molecule. Melamine is a nitrogen-rich compound widely used for the production of plastics, paints and fire retardants [167]. Unfortunately, it is also added to milk to falsely increase the protein count and its misuse in adulterated milk and child formula caused serious concerns when it caused the hospitalisation or death of several children in China [168]. In accordance to the joint evaluation on food additives provided by the Food and Agriculture Organisation (FAO) and the World Health Organisation (WHO), the limit of melamine in dairy products for infants and other food or animal feed is $1\,\text{mg}\,\text{l}^{-1}$ and $2.5\,\text{mg}\,\text{l}^{-1}$, respectively [169].

The substrates were drop-coated with different concentrations of melamine solution ranging from $100\,\text{mg}\,\text{l}^{-1}$ to 1×10^{-5} $\text{mg}\,\text{l}^{-1}$ and characterised by Raman mapping after the post-leaning configuration was induced by solvent evaporation.

At least 50 spectra were collected and used for statistical analysis. An average relative standard deviation of 10 % of the Raman signal at 712 cm^{-1} was calculated for each concentration value. The average Raman spectra for each melamine concentration are reported in figure 5.4(a). This graph shows that very low concentrations of melamine such as 1×10^{-5} mg l^{-1} and 1×10^{-3} mg l^{-1} can be easily detected and distinguished from the blank signal (0 mg l^{-1}). The intensity of the ring-breathing II mode at 712 cm^{-1} tends to increase proportionally with the melamine concentration in the range from 1×10^{-3} mg l^{-1} to 1 mg l^{-1}. For higher concentrations (10 mg l^{-1} and 100 mg l^{-1}), the intensity of the SERS peak at 712 cm^{-1} decreases. Correspondingly, at the same concentrations, it is possible to observe an increase of the classical Raman band around 680 cm^{-1} with the normalisation of the Raman spectra to the intensity of the peak at 712 cm^{-1} in figure 5.4(b). Since the highest intensity of the signal at 712 cm^{-1} is recorded with the melamine concentration of 1 mg l^{-1}, we can infer that the surface coverage of the gold-coated tips by this melamine concentration could be approximated to a quasi-monolayer morphology, which represents the best condition for the enhancement of its Raman signal. By increasing the concentration, the analyte molecules accumulate in a few layers at the top of the gold-coated tips saturating the clustered hot spots and reducing the number of excitation photons that reach the molecule-gold interface. The deposition by drop coating can lead to some accumulation by the coffee stain effect as observed in reference 125.

Despite the surplus surface coverage of the metallic nanostructures, the relative intensity ratio between the specific peaks at 680 cm^{-1} and 712 cm^{-1} can be exploited to build a calibration curve in the range of concentrations between 1×10^{-8} mg l^{-1} and 10 mg l^{-1}. The logarithm of relative intensity ratio at 680 cm^{-1} is plotted with respect to the melamine concentration in figure 5.5. A linear regression model was applied for the calibration and the goodness of the fit was confirmed by the adjusted R^2 value close to 1.

The limit of detection (LOD), as defined from the Eurachem [170], establishes the lowest concentration of the analyte present in a sample that can be detected with a specified level of confidence of substance and that can be distinguished from a null concentration. The LOD is experimentally determined by means of the calibration curve as the value of the concentration corresponding to a certain intensity of the signal given by equation 5.4:

$$\text{LOD} \rightarrow M + 3\sigma, \tag{5.4}$$

where M is the mean normalised intensity at 680 cm^{-1} and σ is the standard deviation of 10 %. The limit of quantification (LOQ) is defined by Eurachem [170] as the lower limit of the measurement at which two distinct values of the concentration can be reasonably discerned. The value of the LOQ is above the LOD. Its value was estimated by the calibration curve by the equation 5.5:

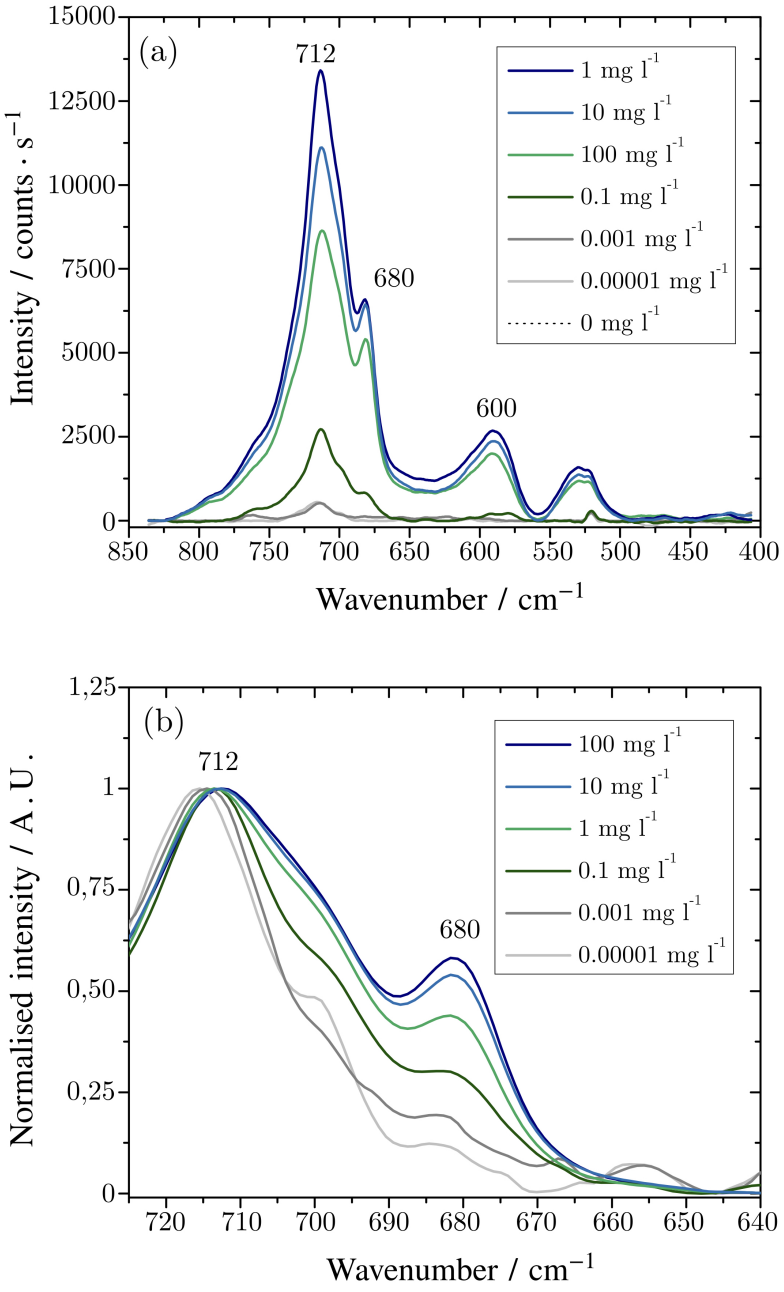

Figure 5.4: (a) Graphs reporting the Raman spectra recorded on the leaning gold-coated SiNWs trapping the molecules. Each graph corresponds to a 1 µl droplet of a solution with melamine concentration ranging from 100 mg l^{-1} to 0.000 01 mg l^{-1}. (b) The spectra were normalised to the intensity of the peak at 712 cm^{-1}. The intensity ratio at 680 cm^{-1} tends to increase proportionally to the melamine concentration.

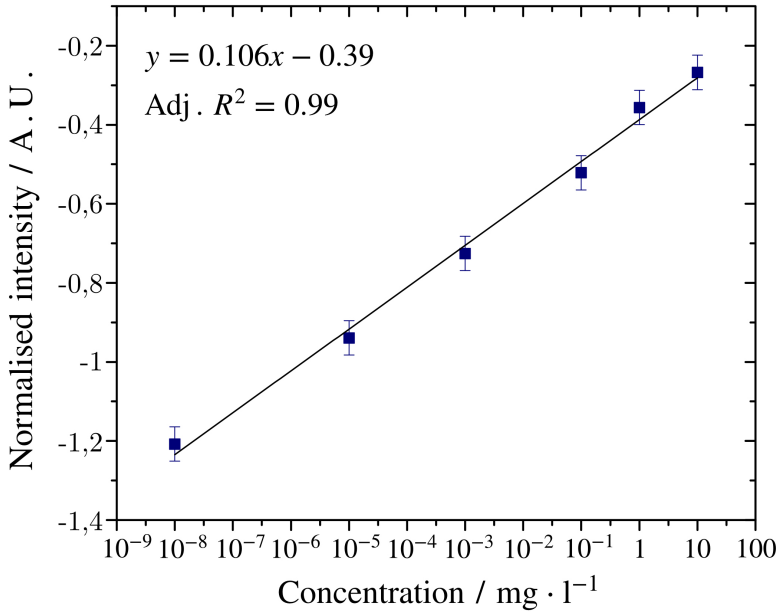

Figure 5.5: Scatter plot of the logarithm of the ratio of the peak intensity at $680\,\mathrm{cm}^{-1}$ and at $720\,\mathrm{cm}^{-1}$ as a function of the melamine concentration in the range from 1×10^{-8} to $10\,\mathrm{mg\,l}^{-1}$. The error bars are obtained by the standard propagation of uncertainty for a logarithmic function.

$$\mathrm{LOQ} \rightarrow M + 10\sigma. \tag{5.5}$$

According to equations 5.4 and 5.5 and to the equation of the linear fit of the calibration curve in figure 5.5, the detection limit is 2.3×10^{-7} $\mathrm{mg\,l}^{-1}$ and the limit of quantification is 1.3×10^{-5} $\mathrm{mg\,l}^{-1}$. The present methodology is then suitable for melamine quantification in the concentration range of 1.3×10^{-5} $\mathrm{mg\,l}^{-1}$ and $10\,\mathrm{mg\,l}^{-1}$ in accordance with the law limits. This result promotes the application of the presented SERS substrate in several fields such as food safety, diagnostic and pharmaceutical.

In this chapter the results concerning the homogeneity of the SERS signal across large area were discussed for the optimised substrate. In addition, the enhancement factor of the substrate was evaluated by means of geometrical assumptions on the number of probe molecules contributing to the SERS signal. A method for a metrological quantification of the amount of analyte was proposed to obtain a more reliable evaluation of the enhancement factor. Furthermore, the gold-coated SiNWs substrate was tested to establish the limit of detection and quantitation with a food contaminant model molecule, melamine.

Chapter 6

Towards future SERS substrates

The work presented in this chapter finds its motivation in the necessity to expand the applicability of the bottom-up lithographic fabrication based on NSL over large area. This is achieved by directing the process of self-assembly through topographical constraint in the substrate to overcome the common drawbacks of NSL. The capabilities of direct laser-writing lithography and conventional reactive ion etching were exploited to build hexagonal and linear topographical structures with modulated shape, lateral size, and depth. Thanks to its wide availability and easy implementation, the spin coating was adopted to deposit the NSs on the structured substrates. The most effective dynamic parameters for the deposition inside the templates were investigated starting from the insights on the correlation length of the NSs monolayer obtained by spin coating on a flat substrate, acquired from the experiments discussed in reference 136 and section 4.4. Scanning electron microscopy was coupled with atomic force microscopy to study the best conditions for the confinement process and to understand the generation of defects inside the templates. Moreover, a method was proposed for the quantitative analysis of the ordering process based on the evaluation of the orientation of hexagonally close-packed domains by means of the Delaunay triangulation of SEM micrographs. An introduction on the shortcomings of NSL and the employment of directed self-assembly is reported in section 6.1, followed by the study of the confinement process by SEM and AFM in section 6.2. The quantitative evaluation of the ordering process inside the templates is reported in section 6.3.

The content of this chapter is subject matter of a paper just submitted for publication.

6.1 Fundamental aspects of directed self-assembly

One of strongest limitation if the use of NSL for advanced applications is given by the formation of defects and loss of the HCP periodicity of the nanoparticles

together with randomness in the orientation and shape of the domains. In the fabrication of a substrate for SERS, for instance, these details hinder the uniformity of the nanostructures and the reproducibility of the measurement. The design of an experimental procedure with controllable output is demanded to extend the size of well-ordered and regularly-shaped domains and to increase the level of uniformity of the nanostructured arrays.

A possible solution allowing to overcome the intrinsic variability of the NSL process is represented by the use of external fields or surface modifications to aid the formation of single-layer crystals of NSs in the process known as directed self-assembly (DSA). This has already been adopted for block copolymers (BCPs) and has received great consideration so far due to its wide application in the micro-electronic field [171, 172, 173]. The substrate modification can consist either in a chemical functionalisation [174, 175] or in the design of topographical templates [176]; the latter is constituted by any structure serving as a guide for the DSA of macromolecular units [177]. The in-plane geometrical dimensions of the topographical structures can be tailored to be commensurate to the characteristic length of the building blocks (diameter of the NSs or width and centre-to-centre distance for BCPs).

The employment of physical patterns to conduct the aggregation process of spherical colloids in well-defined configurations is often referred as *template-assisted self-assembly* (TASA), coined by Xia and co-workers [178]. It has been particularly studied to address the necessities of the development of novel devices for photonics [179], chemical sensing [180], data storage [181] and electronics [182]. The main works focused on the strong geometrical confinement inside long and narrow trenches [183] or small templates containing only a few nanoparticles forming complex aggregates in annular, spiral, zigzag and polygonal shapes [184]. The application of TASA to achieve size separation of polydispersed NSs was also studied in reference 185. The use of pre-patterned substrates is well suited to control the shape of the nanostructures [78] and to grow both two-dimensional colloidal crystals and three-dimensional stacks [94, 186]; for this reason, another term in use to describe this method is *graphoepitaxy*. The last term has been borrowed from the realm of BCPs lithography in which physical confinements were used with the purpose of enlarging the size of well-ordered domains of the copolymers nanophases [187, 188, 189].

6.2 Nanospheres confinement

After the definition of the linear and hexagonal graphoepitaxy structures with different widths and depths, the deposition of NSs was performed by spin coating. The deposition parameters were selected according to previous experiments concerning the NSs ordering maximisation, expressed in terms of correlation length ξ on flat

non-templated substrates [136]. Contrary to the expectations, the self-assembly of the NSs on the patterned substrate is dramatically different from the one found on the flat substrate. Figure 6.1(a) shows a low-magnification SEM image of the flat and patterned area on the substrate and in the detail in figure 6.1(b) the formation of large grains with a low defectivity is observed on the flat portion of the sample. Inside the graphoepitaxy structures, the use of the same deposition parameters resulted in the formation of multiple layers as shown in figure 6.1(c).

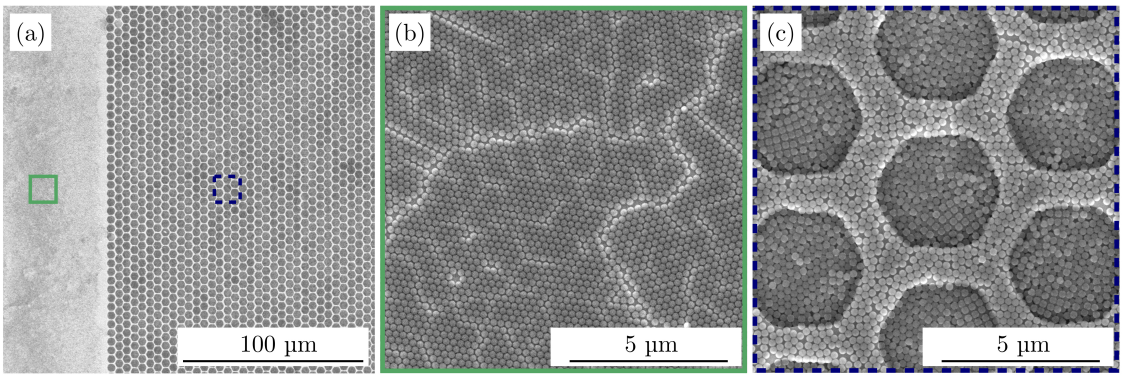

Figure 6.1: (a) Low-magnification SEM micrograph reporting a preliminary comparison between the outcome of self-assembly of NSs on the flat and patterned area of the substrate after spin coating with $\omega = 1250\,\text{rpm}$ and $\alpha = 410\,\text{rpm/s}$. The green (solid) and blue (dashed) frames correspond to the high-magnification SEM images (b) and (c), respectively.

This preliminary result suggests a different self-assembly process with respect to the flat substrate. In literature, the self-assembly process of NSs on flat substrates has been described as the interaction of capillary forces $\overrightarrow{F}_c$ between adjacent spheres, responsible for the hexagonal packing. The presence of a geometrical constraint, such as the graphoepitaxy structures, introduces a perturbation of the conventional self-assembly process since the capillary force acts both on the flat part of the substrate and within the graphoepitaxy [183, 72, 190]. During the deposition, the NSs are spread on the substrate and interact with the physical graphoepitaxy barriers, thus the confinement optimisation requires a fine tuning of both the dynamic spin coating parameters and the height of the graphoepitaxy sidewalls, H. To this goal, a set of samples was prepared by systematically varying both the spinning speed (1250 rpm and 2500 rpm) and H (between 50 nm and 200 nm), as specified in section 3.4.2. The SEM micrographs of the nanospheres assemblies on the patterned substrates are reported for each trial in figure 6.2. Since the effectiveness of the geometrical constraint is proportional to the NSs dimensions, the height of the graphoepitaxy structures is expressed as a fraction of the NSs diameter, D. The tabular form allows making a first qualitative comparison on the confinement effect of the graphoepitaxy on the NSs self-assembly.

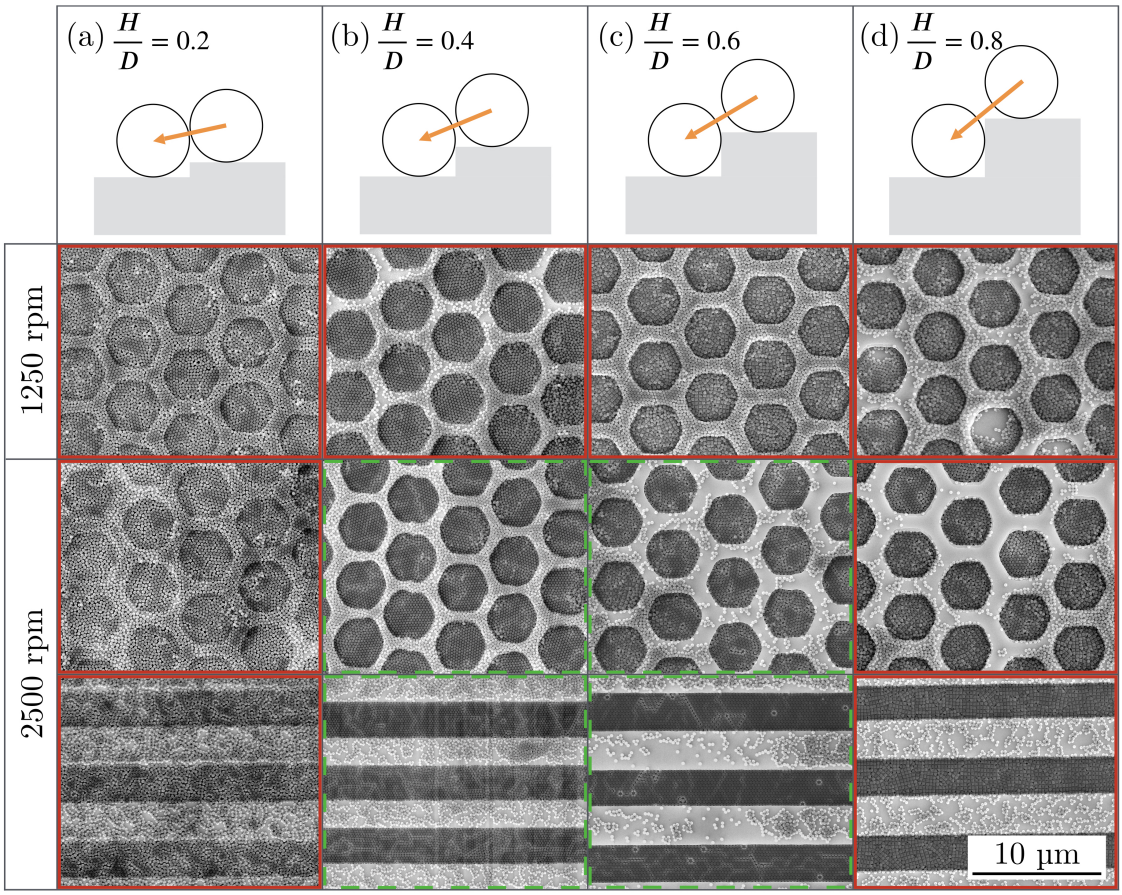

Figure 6.2: Tabular comparison of the SEM images of nanospheres assemblies inside linear and hexagonal templates. The ratio H/D between the height of the constraining walls and the sphere diameter is varied from 0.2 to 0.8 across the columns from (a) to (d). The spin coating speed is varied in the rows from 1250 rpm to 2500 rpm. The red (solid) frames highlight the SEM images of double layers of nanospheres or irregular assemblies. The green (dashed) frames highlight the monolayers with well-ordered domains obtained with suitable dynamic conditions of deposition and geometrical parameters.

The SEM micrographs in column (a) in figure 6.2 describe the self-assembly process inside graphoepitaxy structures with H/D ratio of 0.2 (i.e. depth of 50 nm) deposited at both 1250 rpm and 2500 rpm. Irrespective of the deposition speed, the NSs self-assemble into monolayers in which the orientation of domains seems to be unaffected by the presence of the graphoepitaxy structures. On the contrary, by increasing the H/D ratios the self-assembly process presents a marked dependence on the spinning conditions. The SEM images reported in columns (b) and (c) of figure 6.2 describe the arrangement of the NSs deposited in graphoepitaxy structures having H/D = 0.4 and H/D = 0.6, respectively. When a rotation speed of

1250 rpm is applied, the formation of multiple layers occurred inside the templates, preventing the lithographic use of the confined NSs. However, the increase of the spin coating speed up to 2500 rpm allows the NSs in excess to flow over the physical constraints, resulting in the confinement of a monolayer inside graphoepitaxy structures. The main difference between the self-assembly process at H/D = 0.4 and 0.6 concerns the presence of NSs on the mesa zones in between adjacent graphoepitaxy structures. While for H/D = 0.4 the mesas are completely covered by a monolayer of NSs, at H/D = 0.6 only a small portion of the mesa is occupied by NSs aggregates. In both cases, the monolayer no longer presents domains continuously ordered across the borders of the templates. A further increase of H/D to 0.8 (i.e. depth of 200 nm) results in the formation of multiple layers of NSs regardless of the spin coating speed, as shown in the SEM micrographs in the column (d) of figure 6.2. The structures with H/D ratios of 0.2 and 0.8 result to be inadequate to produce proper confinement of the NSs because they are too shallow or too deep, respectively; the corresponding SEM images are framed in red (solid line) in figure 6.2. These observations indicate that structures with H/D equal to 0.4 or 0.6 facilitate the formation of ordered monolayers; the SEM images corresponding to suitable deposition and geometrical parameters able to direct the self-assembly are framed in green (dashed line) in figure 6.2.

Looking closely to the SEM micrographs reported in figure 6.2(c), it is possible to recognise that even a small amount of residual NSs on the mesas can be very close to the edge of the template. In the interest of understanding whether these NSs can affect the self-assembly of the confined ones, atomic force microscopy was employed. Scans of the nanospheres were acquired on the mesas and inside the structures in both hexagonal and linear ones with H/D = 0.6. Figure 6.3(a) reports an AFM micrograph acquired on the hexagonal template: the colour bar represents the height variation of the topographic image. The blue line indicates the height profile measurement shown in the graph in figure 6.3(b). This profile includes 16 nanospheres aligned inside the hexagonal template without any neighbouring sphere on the mesa; they lay at the same height overcoming the mesa by 100 nm. The AFM image in figure 6.3(c) is acquired in the area highlighted by the square in figure 6.3(a). The green line marks the scan including some nanoparticles sitting on the mesa; the NSs are numbered to simplify the following discussion, and the corresponding height profile is reported in figure 6.3(d). The confined nanospheres are no longer located 100 nm higher than the mesa. In particular, it is possible to note that the nanosphere #2, closest to the confining wall, is at a higher level compared to the nanospheres #3 and #4; the difference in height, namely Δ_{hex}, between the top parts of the nanospheres #1 and #2 is 95 nm.

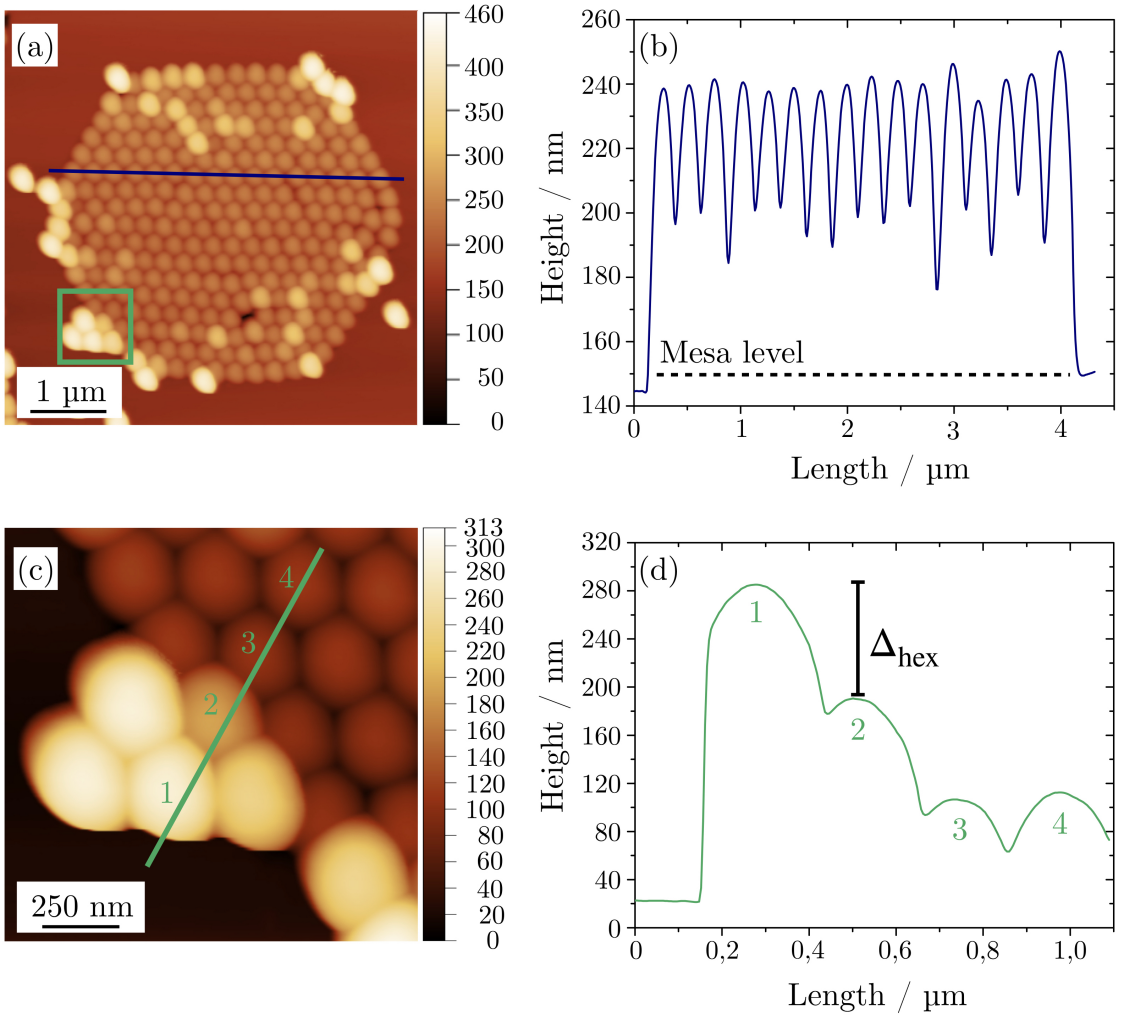

Figure 6.3: (a) AFM micrograph acquired on a hexagonal confining structure filled with a monolayer of nanospheres. The blue line marks the height profile in the line graph (b), where the mesa level is indicated. (c) The second AFM topographic image is acquired in the framed area in (a) and the line profile and nanospheres numbers are indicated. (d) The corresponding height profile reports a difference in the height of NS #1 and #2 equal to $\Delta_{\text{hex}} = 95\,\text{nm}$.

Figure 6.4(a) and (b) report the AFM micrograph acquired on a linear template and the corresponding height profile, respectively; the nanospheres inside the trench numbered as #4 and #5 lay at the same level, 100 nm above the mesa, while nanosphere #3 is at a higher level attracted by nanosphere #2, resulting in a Δ_{lin} of 120 nm.

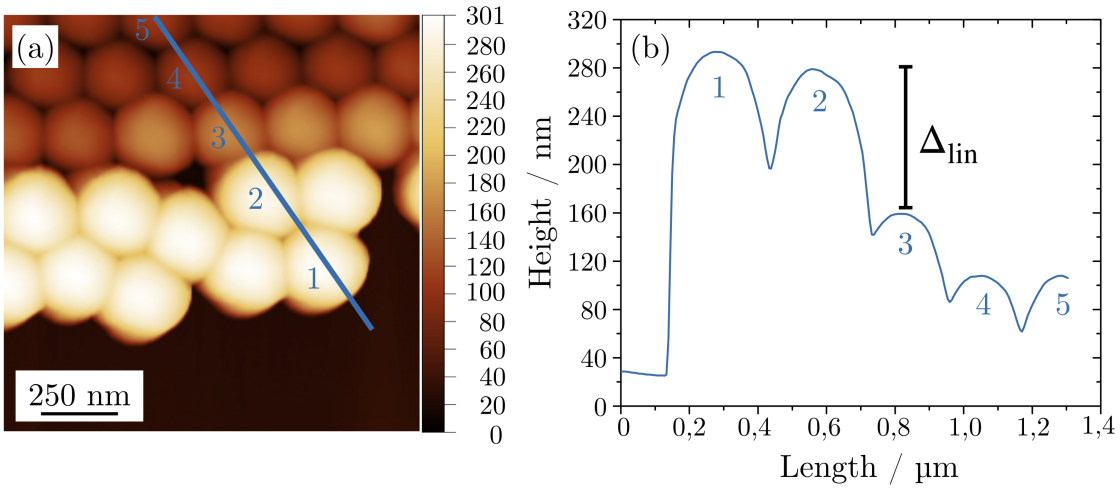

Figure 6.4: (a) AFM micrograph acquired on the NSs monolayer inside a linear graphoepitaxy structure. The coloured line indicates the height profile evaluated on the topographic image. (b) The corresponding line graph presents the height variation as a function of lateral displacement. The value of the distance between NSs #2 and #3 is reported as $\Delta_{\text{lin}} = 120\,\text{nm}$.

The reason why the boundary nanoparticles do not lay at bottom of the graphoepitaxy structure could be sought in the presence of structural defects on the walls. The limited anisotropy in the non-ICP reactive ion etching process causes the wall profile to have a moderate slope rather than high steepness. This feature is much more pronounced in the hexagonal shapes (wherein the etching is influenced by an angular geometry) rather than in the linear trenches. Consequently, the internal NS closest to the edge is sitting above the other confined NSs, thus interacting with the spheres on the mesa. Moreover, the NSs interaction inside and outside the template is stronger in the hexagonal structures rather than in the linear trenches, accordingly with a lower separation of the two examined nano-objects, being the Δ_{hex} parameter smaller than Δ_{lin} (95 nm vs 120 nm).

6.3 Nanospheres ordering

Starting from this preliminary assessment of the DSA process, it is possible to rule out the inefficient conditions for the confinement of the NSs inside the patterned structures and to highlight the suitable ratios H/D. However, further tests are required to be able to investigate the role of the shape of the topographical structures in the confinement process. Some applications may require different template geometries for instance, hexagonal or circular structures can serve in site-specific incubation for different analytes in SERS substrates, while linear templates can be exploited as microfluidic channels in multiplexed analyses [191].

The orientation of the HCP NSs domains was highlighted as the parameter to evaluate the confinement and the ordering process in the two tested shapes. The proposed method is based on the image processing of SEM micrographs by means of the software using Delaunay triangulation, able to recognise the domains and their possible rotations in the angular range between $-30°$ and $30°$. The graphs in figure 6.5 report the normalised distribution of nanoparticles evaluated on the SEM images of the NSs monolayer on the flat area (no templates) and in hexagonal and linear shapes framed in green (dashed line) in figure 6.2. The integral of the curves in the full angular range is always 1, giving the percentage of occurrence of the domains orientation values.

The analysed portion of the non-templated substrate presents a finite number of domains, each with a random shape and orientation. Consequently, the angular distribution varies randomly and there is no favourite orientation angle as shown in figure 6.5(a) (green line). This is an intrinsic characteristic of the self-assembly process on the non-templated substrate resulting in the formation of distinct HCP domains with random orientations and shapes. This can be also observed in the SEM image in figure 6.1(b) where, in each separate domain, the lattice is rotated with respect to the neighbouring grain. On the other hand, the angular distribution in the presence of templates is centred on $0°$ with slight deviations in the orientation indicated by the broadness of the distribution. As shown in figure 6.5(a) and (b), the distribution of the orientation of domains in the sample with hexagonal templates (light-blue line) presents broad bell shapes. The percentage of HCP domains with orientation in the range between $-5°$ and $5°$ is calculated by the integral of the curve and is equal to 32.2 % for structures with H/D = 0.4 and increases up to 46.5 % in those with H/D = 0.6. The linear templates induce a finer orientation constraint between $-5°$ and $5°$ leading to a narrower peak (dark-blue line) including 76.3 % of domains for the case of H/D = 0.4 and 87 % of domains for the structures with H/D = 0.6.

According to this quantitative analysis, the presence of the graphoepitaxy structures contributes to initiating the self-assembly where the NSs tend to align to the confining walls up to forming a uniform angular distribution. The optimal confinement conditions are provided by graphoepitaxy structures with a wall height 0.6 times the diameter D of the nanospheres and linear shape. The linear templates direct the formation of a single-grain monolayer extended to the whole trench with length of tens of micrometres with controlled shape and orientation. In fact, up 96.2 % of domains is oriented in the angular range from $-10°$ to $10°$ as shown in the high-magnification SEM image and the corresponding colour map of orientation in figure 6.6.

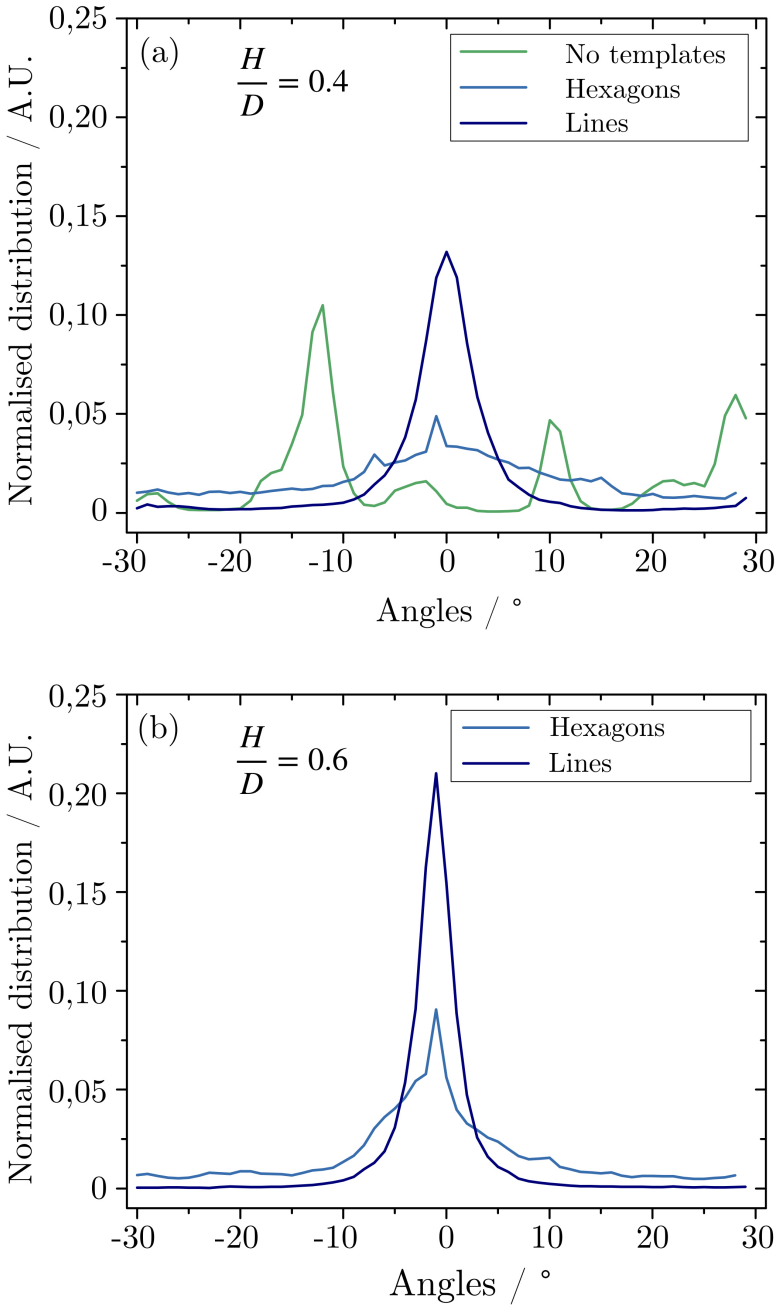

Figure 6.5: Line graphs reporting the normalised distribution of orientation of the domains inside the graphoepitaxy structures with (a) H/D = 0.4 and (b) H/D = 0.6. The orientations are evaluated in the angular range between −30° and 30°. The green line is referred to the flat substrate, while the light-blue and dark-blue lines refer to the substrate patterned with hexagonal and linear structures, respectively.

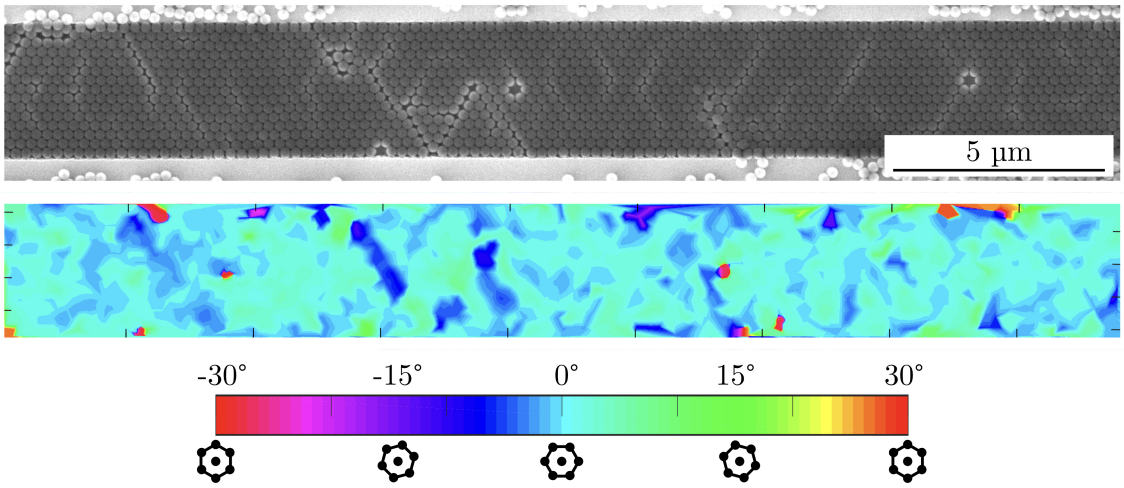

Figure 6.6: The SEM image of the nanospheres inside the linear template is processed by masking the mesas and performing the Delaunay triangulation. The analysis yields a colour map depicting the orientation of the NSs assemblies with a clear prevalence of unit HCP cells oriented at 0° with only some small deviations.

Some defects and deviations may still appear and can be traced back to the outcome of the lithographic process. Additional improvements in the DLW lithography are required in order to have straight edges and to produce a suitable mask for the RIE process, so to obtain confining walls with high steepness and smoothness. This would facilitate the separation of the NSs inside and outside the templates during the spin coating deposition and thus reduce the number of residual particles on the mesas. These are not present in NSs deposition by doctor blading [192] due to a mechanical removal of excess nanoparticles; however, the use of spin coating is motivated by the need to develop proper protocols for the deposition of NSs inside the topographical templates to promote the applicability of DSA processing in industrial nanomanufacturing already relying on spin coating.

6.4 Implications on the fabrication of SERS substrates

Despite some limitations in the lithography process and the interaction with the NSs on the mesas, the employment of patterned substrates allowed to overcome the common problems of NSL arising on flat substrates and to produce a regular pattern of colloids with designed domains shape and orientation over square centimetres area. The results presented so far allow moving forward in the fabrication procedure described in section 2.3.2 to obtain SiNWs inside the graphoepitaxy structures to be used as SERS substrate.

Since the templates were carved in the SiO_2, the remaining mesas and the gold patterned by the NSs on top of them could be removed by soaking the substrate in HF prior to the etching process. So in the favour of performing MACE on the wafer, the patterned gold mask would result to have hexagonal or linear shapes and it would be ready for the catalysis of the electroless etching process. A representative scheme is shown in figure 6.7 as an extension of the fabrication protocol reported in figure 3.8.

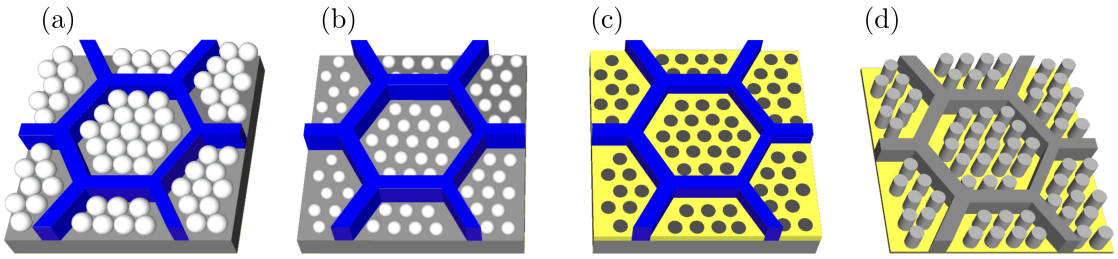

Figure 6.7: (a) The polystyrene NSs are deposited inside the SiO_2 trenches (blue). (b) The size of the NSs can be reduced by plasma etching in the same way as in the non-patterned substrate. (c) The usual patterned gold layer is prepared for MACE. (d) The SiO_2 layer can be removed by soaking the sample in HF and the MACE process can be conducted with the appropriate recipe.

This sample would constitute an upgraded version of the one presented in the previous chapters of this dissertation because of the augmented long-range order and regularly-shaped and oriented domains. Moreover, its employment would facilitate the deposition of the analyte in specific sites and the alignment of the laser beam to the nanostructures for the selection of the area of investigation, thanks to the presence of micrometre-sized trenches easy to locate with the 10× microscope objective installed in the Raman microscope.

Part IV

Conclusion

Final remarks

This thesis has been devoted to the study and development of a fabrication protocol, relying on bottom-up lithography and wet deep etching, especially tailored for the realisation of plasmonic nanostructures for surface-enhanced Raman spectroscopy.

The first part of the work, reported in chapter 4, was devoted to the study and optimisation of the morphology of the silicon nanostructures, in terms of their geometrical and mechanical features. The approach to fabrication based on NSL and MACE represents a low-cost alternative to EBL and RIE and gave promising results for the realisation of the HCP-ordered matrix of flexible SiNWs. It offers multiple degrees of freedom in the design of relevant morphological features. The surface patterning was achieved by NSL tuning the lateral dimension of the plasmonic nanostructures while fixing the inter-wire spacing. The etching process by MACE allowed selecting proper values of the aspect ratio for flexible nanostructures. The formation of bundles of leaning nanowires led to the generation of hot spots assemblies. Different bending configurations were tested to find the optimum flexible nanowires. Nanowires with an aspect ratio of 10:1 were found to self-close driven by the capillary force under exposure to water and trap the molecules at their metallic coated tips. Furthermore, it is desirable to master the fabrication protocol to obtain large enhancement together with homogeneity. Other than the location of hot spots, their distribution and density across large areas are relevant matters. To maximise the order of the nanospheres and so the density of the plasmonic nanostructures, a quantitative analysis of the SEM micrographs of the monolayer was carried out to quantify the degree of order through the correlation length ξ. This analysis offered an important understanding of the ordering process in NSL together with the possibility to tune the degree of order to the optimal conditions. Small nanoparticles of 250 nm in diameter were arranged in HCP lattice with long-range order with ξ of more than 1 µm. The gold-coated nanostructures were tested to discern the influence of the degree of order on the intensity of the SERS signal. The highest order resulted in the largest SERS intensity coherently with an ordered and dense distribution of hot spots.

The second part of the thesis, discussed in chapter 5, was centred on the evaluation of the SERS performance of the substrate. The large coherence in the nanostructures distribution produced a remarkable homogeneity with inter-maps

RSD of 8% calculated on 600×600 µm^2. The performance of the substrate was evaluated by means of the enhancement factor. The calculation was conducted by using a common formula for the average SERS EF reported in equation 1.2. The common difficulties associated with the determination of the EF were highlighted. Particularly, the evaluation of the number of analytes N_{surf} contributing to the SERS signal, usually carried out by means of geometrical assumptions, was identified as a large source of uncertainty in the computation of the EF. A method, based on reference-free X-ray fluorescence, was proposed in order to address the issue of evaluating N_{surf} and contribute to the extensive scientific discussion on the subject. Reference-free XRF may support the determination of the EF since its application provides quite straightforward information on the amount of SERS-active molecules on the substrate. The complexity of the substrate morphology does not undermine the results of the technique which is only sensitive to the photon count of the X-ray fluorescence signal emitted by the elements present on the sample. In principle, this analytical technique could be applied to any molecular species with the only constraints to have a target element, which may be excited to fluorescence by the available excitation energy. Through the selection of sulphur as the target element in MMC probe molecules, the accurate evaluation of the average enhancement factor led to a value of $(3.5 \pm 0.8) \cdot 10^4$. Furthermore, the gold-coated silicon nanowires SERS substrate was tested for analytical chemistry applications by the detection of a common food contaminant, melamine. Particularly, the substrate demonstrated significantly high sensitivity for melamine with a limit of detection of 2.3×10^{-7} mg l^{-1} and limit of quantification of 1.3×10^{-5} mg l^{-1} corresponding to picomolar concentrations of the analyte.

The final part of the dissertation, presented in chapter 6, is focused on the study of the process of directed self-assembly to further upgrade the fabrication process for the SERS substrate. The realisation of topographical patterns was implemented to set a constraint in the confinement and ordering process of the colloidal nanoparticles in NSL. The aim of the graphoepitaxy structures is to overcome the common drawbacks of NSL concerning randomly oriented and shaped domains, thus preventing the formation of grain boundaries and other irregularities that may weaken the homogeneity of the substrate over large area. The combination of direct laser-writing lithography and RIE was adopted for the fabrication of templates with linear and hexagonal shapes having different widths and depths. The efficiency of the confinement process was evaluated by means of systematic SEM and AFM analyses finding the key parameters to control the DSA process. These are the spin coating speed affecting the distribution of the NSs across the substrate, the depth H and width of the templates with respect to the size D of the nanospheres as well as the shape and quality of the sidewalls. The ordering process was evaluated in the graphoepitaxy structures displaying the best confinement, the hexagonal and linear templates with H/D ratio of 0.4 and 0.6, through a quantitative Delaunay

triangulation analysis of the orientation of the confined HCP crystals of NSs. The use of a patterned substrate allowed to govern the self-assembly. It guaranteed the extension of the correlated domains of nanoparticles to the area of tens of micrometres of the graphoepitaxy structures, the distribution in patterns with regular shape and uniform orientation over square centimetres areas. This was especially observed in the linear shape with height 0.6 times the diameter of the nanospheres, where 96.2 % of the domains were aligned to the template within $-10°$ and $10°$.

The nearest perspective to the experiments reported in this dissertation in the framework of the metrological project MetVBadBugs is the employment of the gold-coated SiNWs substrate for the SERS analysis of biological systems of interest, such as bacteria grown on the substrate and treated with antibiotics. The design of SERS-active substrates, in terms of geometrical parameters and materials choice, can be optimised by means of numerical simulations of the electromagnetic enhancement. Different methods can be adopted to solve Maxwell's equations, e.g. the discrete-dipole approximation (DDA) method [130, 193] or the finite difference time domain (FTDT) method [194]. Moreover, computational methodologies, such as molecular dynamics simulations, could be implemented to complement the experimental results by providing a significant understanding of the local mechanism of molecular adsorption and interaction on the metallic surface [195]. Benefiting from these additional simulations, the fabrication protocol, comprehensive of the directed self-assembly process, could provide new optimised plasmonic substrates for sensitive detection of a variety of SERS-active analytes for pharmaceutical, food quality and environmental analyses. The extensive knowledge gained on NSL and the expertise on MACE could be applied separately or together for the realisation of advanced materials, nanostructures or devices for several fields of application, encompassing sensing, optoelectronics, micro and nanoelectronics, energy storage and conversion.

Bibliography

[1] C. V. Raman and K. S. Krishnan. "A new type of secondary radiation". In: *Nature* 121.3048 (1928), p. 501.

[2] K. M. Baek et al. "Sequentially self-assembled rings-in-mesh nanoplasmonic arrays for surface-enhanced Raman spectroscopy". In: *Chemistry of Materials* 27.14 (2015), pp. 5007–5013.

[3] D. L. Jeanmaire and R. P. Van Duyne. "Surface Raman spectroelectrochemistry Part I. Heterocyclic, aromatic, and aliphatic amines adsorbed on the anodized silver electrode". In: *Journal of Electroanalytical Chemistry* 84.1 (1977), pp. 1–20.

[4] S.-Y. Ding et al. "Electromagnetic theories of surface-enhanced Raman spectroscopy". In: *Chemical Society Reviews* 46.13 (2017), pp. 4042–4076.

[5] M.-L. Xu et al. "Detection of pesticide residues in food using surface-enhanced Raman spectroscopy: a review". In: *Journal of agricultural and food chemistry* 65.32 (2017), pp. 6719–6726.

[6] A. M. Giovannozzi et al. "Rapid and sensitive detection of melamine in milk with gold nanoparticles by Surface Enhanced Raman Scattering". In: *Food Chemistry* 159 (2014), pp. 250–256.

[7] L. Mandrile et al. "Rapid and sensitive detection of pyrimethanil residues on pome fruits by Surface Enhanced Raman Scattering". In: *Food chemistry* 244 (2018), pp. 16–24.

[8] R. S. Golightly, W. E. Doering, and M. J. Natan. *Surface-enhanced Raman spectroscopy and homeland security: a perfect match?* 2009.

[9] X. Li et al. "Surface Enhanced Raman Spectroscopy (SERS) for the Multiplex Detection of Braf, Kras, and Pik3ca Mutations in Plasma of Colorectal Cancer Patients". In: *Theranostics* 8.6 (2018), p. 1678.

[10] C. L. Brosseau, F. Casadio, and R. P. Van Duyne. "Revealing the invisible: using surface-enhanced Raman spectroscopy to identify minute remnants of color in Winslow Homer's colorless skies". In: *Journal of Raman Spectroscopy* 42.6 (2011), pp. 1305–1310.

[11] L. H. Oakley et al. “Identification of organic materials in historic oil paintings using correlated extractionless surface-enhanced Raman scattering and fluorescence microscopy”. In: *Analytical chemistry* 83.11 (2011), pp. 3986–3989.

[12] W. F. Paxton et al. “Surface-enhanced Raman spectroelectrochemistry of TTF-modified self-assembled monolayers”. In: *The journal of physical chemistry letters* 2.10 (2011), pp. 1145–1149.

[13] K. Kneipp et al. “Ultrasensitive chemical analysis by Raman spectroscopy”. In: *Chemical reviews* 99.10 (1999), pp. 2957–2976.

[14] C. L. Haynes, A. D. McFarland, and R. P. V. Duyne. *Surface-enhanced Raman spectroscopy*. 2005.

[15] S. D. Christesen. “Raman Cross Sections of Chemical Agents and Simulants”. In: *Appl. Spectrosc.* 42.2 (1988), pp. 318–321.

[16] R. Aggarwal et al. “Measurement of the absolute Raman scattering cross section of the 1584-cm- 1 band of benzenethiol and the surface-enhanced Raman scattering cross section enhancement factor for femtosecond laser-nanostructured substrates”. In: *Journal of Raman Spectroscopy: An International Journal for Original Work in all Aspects of Raman Spectroscopy, Including Higher Order Processes, and also Brillouin and Rayleigh Scattering* 40.9 (2009), pp. 1331–1333.

[17] M. Fleischmann, P. J. Hendra, and A. J. McQuillan. “Raman spectra of pyridine adsorbed at a silver electrode”. In: *Chemical Physics Letters* 26.2 (1974), pp. 163–166.

[18] H. Seki. “Raman spectra of molecules considered to be surface enhanced”. In: *Journal of electron spectroscopy and related Phenomena* 39 (1986), pp. 289–310.

[19] M. Moskovits. “Surface roughness and the enhanced intensity of Raman scattering by molecules adsorbed on metals”. In: *The Journal of Chemical Physics* 69.9 (1978), pp. 4159–4161.

[20] M. G. Albrecht and J. A. Creighton. “Anomalously intense Raman spectra of pyridine at a silver electrode”. In: *Journal of the american chemical society* 99.15 (1977), pp. 5215–5217.

[21] S. Boujday et al. “Enhanced vibrational spectroscopies as tools for small molecule biosensing”. In: *Sensors* 15.9 (2015), pp. 21239–21264.

[22] N. Guillot and M. L. de la Chapelle. “The electromagnetic effect in surface enhanced Raman scattering: Enhancement optimization using precisely controlled nanostructures”. In: *Journal of Quantitative Spectroscopy and Radiative Transfer* 113.18 (2012), pp. 2321–2333.

[23] K. A. Willets and R. P. Van Duyne. "Localized surface plasmon resonance spectroscopy and sensing". In: *Annu. Rev. Phys. Chem.* 58 (2007), pp. 267–297.

[24] K. Kneipp et al. "Surface-enhanced Raman scattering and biophysics". In: *Journal of Physics: Condensed Matter* 14.18 (2002), R597.

[25] M. J. Natan. "Concluding remarks surface enhanced Raman scattering". In: *Faraday discussions* 132 (2006), pp. 321–328.

[26] E. Le Ru et al. "Surface enhanced Raman scattering enhancement factors: a comprehensive study". In: *The Journal of Physical Chemistry C* 111.37 (2007), pp. 13794–13803.

[27] D. Lin et al. "Large-area Au-nanoparticle-functionalized Si nanorod arrays for spatially uniform surface-enhanced Raman spectroscopy". In: *ACS nano* 11.2 (2017), pp. 1478–1487.

[28] M. Fan, G. F. Andrade, and A. G. Brolo. "A review on the fabrication of substrates for surface enhanced Raman spectroscopy and their applications in analytical chemistry". In: *Analytica chimica acta* 693.1-2 (2011), pp. 7–25.

[29] A. B. Zrimsek, A.-I. Henry, and R. P. Van Duyne. "Single molecule surface-enhanced Raman spectroscopy without nanogaps". In: *The Journal of Physical Chemistry Letters* 4.19 (2013), pp. 3206–3210.

[30] J. F. Betz et al. "Simple SERS substrates: powerful, portable, and full of potential". In: *Physical Chemistry Chemical Physics* 16.6 (2014), pp. 2224–2239.

[31] M. Fränzl et al. "Interaction of One-Dimensional Photonic Crystals and Metal Nanoparticle Arrays and Its Application for Surface-Enhanced Raman Spectroscopy". In: *The Journal of Physical Chemistry C* 122.18 (2018), pp. 10153–10158.

[32] E. Le Ru and P. Etchegoin. *Principles of Surface-Enhanced Raman Spectroscopy: and related plasmonic effects*. Elsevier, 2008.

[33] S. A. Maier. *Plasmonics: fundamentals and applications*. Springer Science & Business Media, 2007.

[34] B. Sharma et al. "SERS: Materials, applications, and the future". In: *Materials today* 15.1-2 (2012), pp. 16–25.

[35] G. McNay et al. "Surface-enhanced Raman scattering (SERS) and surface-enhanced resonance Raman scattering (SERRS): a review of applications". In: *Applied spectroscopy* 65.8 (2011), pp. 825–837.

[36] S. Tian et al. "Aluminum nanocrystals: a sustainable substrate for quantitative SERS-based DNA detection". In: *Nano letters* 17.8 (2017), pp. 5071–5077.

[37] M. F. Cardinal et al. “Expanding applications of SERS through versatile nanomaterials engineering”. In: *Chemical Society Reviews* 46.13 (2017), pp. 3886–3903.

[38] C. L. Lay et al. “Aluminum nanostructures with strong visible-range SERS activity for versatile micropatterning of molecular security labels”. In: *Nanoscale* 10.2 (2018), pp. 575–581.

[39] F. W. King, R. P. Van Duyne, and G. C. Schatz. “Theory of Raman scattering by molecules adsorbed on electrode surfaces”. In: *The Journal of Chemical Physics* 69.10 (1978), pp. 4472–4481.

[40] T. M. Cotton, S. G. Schultz, and R. P. Van Duyne. “Surface-enhanced resonance Raman scattering from cytochrome c and myoglobin adsorbed on a silver electrode”. In: *Journal of the American Chemical Society* 102.27 (1980), pp. 7960–7962.

[41] H. Lin et al. “Surface-enhanced Raman scattering from silver-plated porous silicon”. In: *The Journal of Physical Chemistry B* 108.31 (2004), pp. 11654–11659.

[42] F. Giorgis et al. “Porous silicon as efficient surface enhanced Raman scattering (SERS) substrate”. In: *Applied Surface Science* 254.22 (2008), pp. 7494–7497.

[43] C. Novara et al. “SERS active silver nanoparticles synthesized by inkjet printing on mesoporous silicon”. In: *Nanoscale research letters* 9.1 (2014), p. 527.

[44] L. Mikac et al. “Preparation and characterization of SERS substrates: From colloids to solid substrates”. In: *2015 38th International Convention on Information and Communication Technology, Electronics and Microelectronics (MIPRO)*. IEEE. 2015, pp. 9–11.

[45] M. Gómez and M. Lazzari. “Reliable and cheap SERS active substrates”. In: *Materials Today* 7.17 (2014), pp. 358–359.

[46] F. Tian et al. “Surface enhanced Raman scattering with gold nanoparticles: effect of particle shape”. In: *Analytical Methods* 6.22 (2014), pp. 9116–9123.

[47] F. Benz et al. “SERS of individual nanoparticles on a mirror: size does matter, but so does shape”. In: *The journal of physical chemistry letters* 7.12 (2016), pp. 2264–2269.

[48] K. Kneipp et al. “Single molecule detection using surface-enhanced Raman scattering (SERS)”. In: *Physical review letters* 78.9 (1997), p. 1667.

[49] S. Nie and S. R. Emory. “Probing single molecules and single nanoparticles by surface-enhanced Raman scattering”. In: *science* 275.5303 (1997), pp. 1102–1106.

[50] A. Virga et al. “Silver nanoparticles on porous silicon: approaching single molecule detection in resonant SERS regime”. In: *The Journal of Physical Chemistry C* 117.39 (2013), pp. 20139–20145.

[51] S. L. Kleinman et al. “Creating, characterizing, and controlling chemistry with SERS hot spots”. In: *Physical Chemistry Chemical Physics* 15.1 (2013), pp. 21–36.

[52] R. Tantra, R. J. Brown, and M. J. Milton. “Strategy to improve the reproducibility of colloidal SERS”. In: *Journal of Raman Spectroscopy: An International Journal for Original Work in all Aspects of Raman Spectroscopy, Including Higher Order Processes, and also Brillouin and Rayleigh Scattering* 38.11 (2007), pp. 1469–1479.

[53] A. Lamberti et al. “Ultrasensitive Ag-coated TiO2 nanotube arrays for flexible SERS-based optofluidic devices”. In: *Journal of Materials Chemistry C* 3.26 (2015), pp. 6868–6875.

[54] M. De Jesus et al. “Nanofabrication of densely packed metal–polymer arrays for surface-enhanced Raman spectrometry”. In: *Applied spectroscopy* 59.12 (2005), pp. 1501–1508.

[55] Q. Yu et al. “Inverted size-dependence of surface-enhanced Raman scattering on gold nanohole and nanodisk arrays”. In: *Nano letters* 8.7 (2008), pp. 1923–1928.

[56] J. Theiss et al. “Plasmonic nanoparticle arrays with nanometer separation for high-performance SERS substrates”. In: *Nano letters* 10.8 (2010), pp. 2749–2754.

[57] J. D. Caldwell et al. “Plasmonic nanopillar arrays for large-area, high-enhancement surface-enhanced Raman scattering sensors”. In: *ACS nano* 5.5 (2011), pp. 4046–4055.

[58] S. M. Wells et al. “Efficient disc on pillar substrates for surface enhanced Raman spectroscopy”. In: *Chemical Communications* 47.13 (2011), pp. 3814–3816.

[59] M. M. Greve and B. Holst. “Optimization of an electron beam lithography instrument for fast, large area writing at 10 kV acceleration voltage”. In: *Journal of Vacuum Science & Technology B, Nanotechnology and Microelectronics: Materials, Processing, Measurement, and Phenomena* 31.4 (2013), p. 043202.

[60] N. A. Abu Hatab, J. M. Oran, and M. J. Sepaniak. “Surface-enhanced Raman spectroscopy substrates created via electron beam lithography and nanotransfer printing”. In: *ACS nano* 2.2 (2008), pp. 377–385.

[61] L. Liu et al. "A high-performance and low cost SERS substrate of plasmonic nanopillars on plastic film fabricated by nanoimprint lithography with AAO template". In: *AIP Advances* 7.6 (2017), p. 065205.

[62] V. Suresh et al. "Fabrication of Large-Area Flexible SERS Substrates by Nanoimprint Lithography". In: *ACS Applied Nano Materials* 1.2 (2018), pp. 886–893.

[63] T. Gao et al. "High performance surface-enhanced Raman scattering substrates of Si-based Au film developed by focused ion beam nanofabrication". In: *Nanoscale research letters* 7.1 (2012), p. 399.

[64] J. Smolsky et al. "Surface-enhanced Raman scattering-based immunoassay technologies for detection of disease biomarkers". In: *Biosensors* 7.1 (2017), p. 7.

[65] C. Fang et al. "Preparation of a SERS substrate and its sample-loading method for point-of-use application". In: *Nanotechnology* 20.40 (2009), p. 405604.

[66] F. S. Bates and G. Fredrickson. "Block copolymers-designer soft materials". In: *Physics today* 52 (2000).

[67] P. Colson, R. Cloots, and C. Henrist. "Experimental design applied to spin coating of 2D colloidal crystal masks: a relevant method?" In: *Langmuir* 27.21 (2011), pp. 12800–12806.

[68] J. A. Pelesko. *Self assembly: the science of things that put themselves together*. Chapman and Hall/CRC, 2007.

[69] G. M. Whitesides and B. Grzybowski. "Self-assembly at all scales". In: *Science* 295.5564 (2002), pp. 2418–2421.

[70] R. A. Jones. *Soft condensed matter*. Vol. 6. Oxford University Press, 2002.

[71] N. Denkov et al. "Mechanism of formation of two-dimensional crystals from latex particles on substrates". In: *Langmuir* 8.12 (1992), pp. 3183–3190.

[72] N. Denkov et al. "Two-dimensional crystallization". In: *Nature (London)* 361 (1993), p. 26.

[73] K. Nagayama. "Two-dimensional self-assembly of colloids in thin liquid films". In: *Colloids and Surfaces A: Physicochemical and Engineering Aspects* 109 (1996), pp. 363–374.

[74] C. Zhang, S. Cvetanovic, and J. M. Pearce. "Fabricating ordered 2-D nanostructured arrays using nanosphere lithography". In: *MethodsX* 4 (2017), pp. 229–242.

[75] B. Cipra. *Packing challenge mastered at last*. 1998.

[76] M. Parchine et al. "Large area 2D and 3D colloidal photonic crystals fabricated by a roll-to-roll Langmuir–Blodgett method". In: *Langmuir* 32.23 (2016), pp. 5862–5869.

[77] L. Zhang and Y. Xiong. "Rapid self-assembly of submicrospheres at liquid surface by controlling evaporation and its mechanism". In: *Journal of colloid and interface science* 306.2 (2007), pp. 428–432.

[78] P. Colson, C. Henrist, and R. Cloots. "Nanosphere lithography: a powerful method for the controlled manufacturing of nanomaterials". In: *Journal of Nanomaterials* 2013 (2013), p. 21.

[79] R. Micheletto, H. Fukuda, and M. Ohtsu. "A simple method for the production of a two-dimensional, ordered array of small latex particles". In: *Langmuir* 11.9 (1995), pp. 3333–3336.

[80] Z. Zhong et al. "Fabrication of submicron magnetic oxide antidot arrays by combining nanosphere lithography with sputtering technology". In: *Physica E: Low-dimensional Systems and Nanostructures* 40.3 (2008), pp. 516–519.

[81] L. Mikac et al. "Surface-enhanced Raman spectroscopy substrate based on Ag-coated self-assembled polystyrene spheres". In: *Journal of Molecular Structure* 1146 (2017), pp. 530–535.

[82] H. Yang and P. Jiang. "Large-scale colloidal self-assembly by doctor blade coating". In: *Langmuir* 26.16 (2010), pp. 13173–13182.

[83] C. Brodehl, S. Greulich-Weber, and J. K. Lindner. "Fabrication of tailored nanoantennas on large areas for plasmonic devices". In: *Materials Today: Proceedings* 4 (2017), S44–S51.

[84] X. Zhang et al. "Advances in contemporary nanosphere lithographic techniques". In: *Journal of Nanoscience and Nanotechnology* 6.7 (2006), pp. 1920–1934.

[85] N. Li et al. "Window-assisted nanosphere lithography for vacuum micro-nano-electronics". In: *AIP Advances* 5.4 (2015), p. 047101.

[86] M. Wang et al. "CVD growth of large area smooth-edged graphene nanomesh by nanosphere lithography". In: *Scientific reports* 3 (2013), p. 1238.

[87] D.-G. Choi et al. "Nanopatterned magnetic metal via colloidal lithography with reactive ion etching". In: *Chemistry of materials* 16.22 (2004), pp. 4208–4211.

[88] Q. Yu et al. "Filtration-assembling colloidal crystal templates for ordered macroporous nanoparticle films". In: *Journal of Materials Chemistry* 21.44 (2011), pp. 18089–18094.

[89] D.-G. Choi et al. "Particle arrays with patterned pores by nanomachining with colloidal masks". In: *Journal of the American Chemical Society* 127.6 (2005), pp. 1636–1637.

[90] J. H. Moon et al. “Multiscale Nanopatterns Templated from Two-Dimensional Assemblies of Photoresist Particles”. In: *Advanced Materials* 17.21 (2005), pp. 2559–2562.

[91] J. Wang et al. “Wet etching-assisted colloidal lithography: a general strategy toward nanodisk and nanohole arrays on arbitrary substrates”. In: *ACS applied materials & interfaces* 6.12 (2014), pp. 9207–9213.

[92] K. Chen et al. “Moiré nanosphere lithography”. In: *ACS nano* 9.6 (2015), pp. 6031–6040.

[93] B. Gates, D. Qin, and Y. Xia. “Assembly of nanoparticles into opaline structures over large areas”. In: *Advanced Materials* 11.6 (1999), pp. 466–469.

[94] G. A. Ozin and S. M. Yang. “The race for the photonic chip: colloidal crystal assembly in silicon wafers”. In: *Advanced Functional Materials* 11.2 (2001), pp. 95–104.

[95] V. Morandi et al. “Colloidal photonic crystals doped with gold nanoparticles: spectroscopy and optical switching properties”. In: *Advanced Functional Materials* 17.15 (2007), pp. 2779–2786.

[96] H. Deckman and J. Dunsmuir. “Natural lithography”. In: *Applied Physics Letters* 41.4 (1982), pp. 377–379.

[97] J. C. Hulteen and R. P. Van Duyne. “Nanosphere lithography: A materials general fabrication process for periodic particle array surfaces”. In: *Journal of Vacuum Science & Technology A: Vacuum, Surfaces, and Films* 13.3 (1995), pp. 1553–1558.

[98] T. R. Jensen et al. “Nanosphere lithography: tunable localized surface plasmon resonance spectra of silver nanoparticles”. In: *The Journal of Physical Chemistry B* 104.45 (2000), pp. 10549–10556.

[99] C. L. Haynes and R. P. Van Duyne. “Nanosphere lithography: a versatile nanofabrication tool for studies of size-dependent nanoparticle optics”. In: *Journal of Physical Chemistry* 105.24 (2001), pp. 5599–5611.

[100] A. J. Haes et al. “Plasmonic materials for surface-enhanced sensing and spectroscopy”. In: *MRS bulletin* 30.5 (2005), pp. 368–375.

[101] C. L. Haynes et al. “Angle-resolved nanosphere lithography: manipulation of nanoparticle size, shape, and interparticle spacing”. In: *The Journal of Physical Chemistry B* 106.8 (2002), pp. 1898–1902.

[102] G. Zhang and D. Wang. “Fabrication of heterogeneous binary arrays of nanoparticles via colloidal lithography”. In: *Journal of the American Chemical Society* 130.17 (2008), pp. 5616–5617.

[103] L. A. Dick et al. "Metal film over nanosphere (MFON) electrodes for surface-enhanced Raman spectroscopy (SERS): Improvements in surface nanostructure stability and suppression of irreversible loss". In: *The Journal of Physical Chemistry B* 106.4 (2002), pp. 853–860.

[104] S. S. Masango et al. "High-resolution distance dependence study of surface-enhanced Raman scattering enabled by atomic layer deposition". In: *Nano letters* 16.7 (2016), pp. 4251–4259.

[105] M. C. Giordano et al. "SERS amplification from self-organized arrays of plasmonic nanocrescents". In: *ACS applied materials & interfaces* 8.10 (2016), pp. 6629–6638.

[106] C. Fang et al. "Templated silver nanocube arrays for single-molecule SERS detection". In: *Rsc Advances* 3.13 (2013), pp. 4288–4293.

[107] P. Jiang and M. J. McFarland. "Wafer-scale periodic nanohole arrays templated from two-dimensional nonclose-packed colloidal crystals". In: *Journal of the American Chemical Society* 127.11 (2005), pp. 3710–3711.

[108] S. H. Lee et al. "Self-assembled plasmonic nanohole arrays". In: *Langmuir* 25.23 (2009), pp. 13685–13693.

[109] J. Chen et al. "Surface-enhanced Raman scattering of rhodamine 6G on nanowire arrays decorated with gold nanoparticles". In: *Nanotechnology* 19.27 (2008), p. 275712.

[110] M. Hu et al. "Gold nanofingers for molecule trapping and detection". In: *Journal of the American Chemical Society* 132.37 (2010), pp. 12820–12822.

[111] W. Wu et al. "Cones fabricated by 3D nanoimprint lithography for highly sensitive surface enhanced Raman spectroscopy". In: *Nanotechnology* 21.25 (2010), p. 255502.

[112] T. Li et al. "Wafer-Scale Nanopillars Derived from Block Copolymer Lithography for Surface-Enhanced Raman Spectroscopy". In: *ACS applied materials & interfaces* 8.24 (2016), pp. 15668–15675.

[113] M. S. Schmidt, J. Hubner, and A. Boisen. "Large area fabrication of leaning silicon nanopillars for Surface Enhanced Raman Spectroscopy". In: *Advanced Materials* 24.10 (2012), pp. 11–18.

[114] N. Bontempi et al. "Probing the spatial extension of light trapping-induced enhanced Raman scattering in high-density Si nanowire arrays". In: *Nanotechnology* 25.46 (2014), p. 465705.

[115] E. Garnett and P. Yang. "Light trapping in silicon nanowire solar cells". In: *Nano letters* 10.3 (2010), pp. 1082–1087.

[116] M. Shao, D. D. D. Ma, and S.-T. Lee. "Silicon nanowires–synthesis, properties, and applications". In: *European Journal of Inorganic Chemistry* 2010.27 (2010), pp. 4264–4278.

[117] Z. Huang et al. "Metal-Assisted Chemical Etching of Silicon: A Review: In memory of Prof. Ulrich Gösele". In: *Advanced materials* 23.2 (2011), pp. 285–308.

[118] R. A. Lai et al. "Schottky barrier catalysis mechanism in metal-assisted chemical etching of silicon". In: *ACS applied materials & interfaces* 8.14 (2016), pp. 8875–8879.

[119] N. Geyer et al. "Model for the mass transport during metal-assisted chemical etching with contiguous metal films as catalysts". In: *The journal of physical chemistry C* 116.24 (2012), pp. 13446–13451.

[120] B. P. Azeredo et al. "Direct Imprinting of Porous Silicon via Metal-Assisted Chemical Etching". In: *Advanced Functional Materials* 26.17 (2016), pp. 2929–2939.

[121] G. Yuan et al. "Understanding the origin of the low performance of chemically grown silicon nanowires for solar energy conversion". In: *Angewandte Chemie* 123.10 (2011), pp. 2382–2386.

[122] K. Peng et al. "Silicon nanowires for rechargeable lithium-ion battery anodes". In: *Applied Physics Letters* 93.3 (2008), p. 033105.

[123] A. I. Hochbaum et al. "Enhanced thermoelectric performance of rough silicon nanowires". In: *Nature* 451.7175 (2008), p. 163.

[124] K.-Q. Peng, X. Wang, and S.-T. Lee. "Gas sensing properties of single crystalline porous silicon nanowires". In: *Applied Physics Letters* 95.24 (2009), p. 243112.

[125] S. Kara et al. "Fabrication of flexible silicon nanowires by self-assembled metal assisted chemical etching for surface enhanced Raman spectroscopy". In: *RSC Advances* 6.96 (2016), pp. 93649–93659.

[126] C. Minelli et al. "Measuring the size and density of nanoparticles by centrifugal sedimentation and flotation". In: *Analytical Methods* 10.15 (2018), pp. 1725–1732.

[127] L. Li et al. "Controlling the Geometries of Si Nanowires through Tunable Nanosphere Lithography". In: *ACS applied materials & interfaces* 9.8 (2017), pp. 7368–7375.

[128] D. A. Vega et al. "Ordering mechanisms in two-dimensional sphere-forming block copolymers". In: *Physical Review E* 71.6 (2005), p. 061803.

[129] C.-C. Liu et al. "Practical implementation of order parameter calculation for directed assembly of block copolymer thin films". In: *Journal of Polymer Science Part B: Polymer Physics* 48.24 (2010), pp. 2589–2603.

[130] F. S. Ou et al. "Hot-spot engineering in polygonal nanofinger assemblies for surface enhanced Raman spectroscopy". In: *Nano letters* 11.6 (2011), pp. 2538–2542.

[131] M. Frisch et al. *Gaussian 03, revision C. 02*. 2004.

[132] A. D. Becke. "Density-functional thermochemistry. III. The role of exact exchange". In: *The Journal of chemical physics* 98.7 (1993), pp. 5648–5652.

[133] G. Socrates. *Infrared and Raman characteristic group frequencies: tables and charts*. John Wiley & Sons, 2004.

[134] J. Lubeck et al. "A novel instrument for quantitative nanoanalytics involving complementary X-ray methodologies". In: *Review of Scientific Instruments* 84.4 (2013), p. 045106.

[135] M. Müller et al. "Characterization of high-k nanolayers by grazing incidence X-ray spectrometry". In: *Materials* 7.4 (2014), pp. 3147–3159.

[136] E. Cara et al. "Influence of the long-range ordering of gold-coated Si nanowires on SERS". In: *Scientific reports* 8.1 (2018), p. 11305.

[137] H. Namatsu et al. "Dimensional limitations of silicon nanolines resulting from pattern distortion due to surface tension of rinse water". In: *Applied physics letters* 66.20 (1995), pp. 2655–2657.

[138] M. Mura, N. Martsinovich, and L. Kantorovich. "Theoretical study of melamine superstructures and their interaction with the Au (111) surface". In: *Nanotechnology* 19.46 (2008), p. 465704.

[139] F. Silly et al. "Melamine structures on the Au (111) surface". In: *The Journal of Physical Chemistry C* 112.30 (2008), pp. 11476–11480.

[140] E. Koglin, B. J. Kip, and R. J. Meier. "Adsorption and displacement of melamine at the Ag/electrolyte interface probed by surface-enhanced Raman microprobe spectroscopy". In: *The Journal of Physical Chemistry* 100.12 (1996), pp. 5078–5089.

[141] B. Liu, M. Lin, and H. Li. "Potential of SERS for rapid detection of melamine and cyanuric acid extracted from milk". In: *Sensing and Instrumentation for Food Quality and Safety* 4.1 (2010), pp. 13–19.

[142] Z.-Q. Wen, G. Li, and D. Ren. "Detection of trace melamine in raw materials used for protein pharmaceutical manufacturing using surface-enhanced Raman spectroscopy (SERS) with gold nanoparticles". In: *Applied spectroscopy* 65.5 (2011), pp. 514–521.

[143] K. Wu et al. "Plasmon resonances of Ag capped Si nanopillars fabricated using mask-less lithography". In: *Optics express* 23.10 (2015), pp. 12965–12978.

[144] D. T. Toolan et al. "On the mechanisms of colloidal self-assembly during spin-coating". In: *Soft Matter* 10.44 (2014), pp. 8804–8812.

[145] A. Chandramohan et al. "Model for large-area monolayer coverage of polystyrene nanospheres by spin coating". In: *Scientific reports* 7 (2017), p. 40888.

[146] F. Ferrarese Lupi et al. "Rapid thermal processing of self-assembling block copolymer thin films". In: *Nanotechnology* 24.31 (2013), p. 315601.

[147] T. J. Giammaria et al. "Micrometer-Scale Ordering of Silicon-Containing Block Copolymer Thin Films via High-Temperature Thermal Treatments". In: *ACS applied materials & interfaces* 8.15 (2016), pp. 9897–9908.

[148] S.-M. Hur et al. "Molecular pathways for defect annihilation in directed self-assembly". In: *Proceedings of the National Academy of Sciences* 112.46 (2015), pp. 14144–14149.

[149] J. Chen et al. "Controllable fabrication of 2D colloidal-crystal films with polystyrene nanospheres of various diameters by spin-coating". In: *Applied Surface Science* 270 (2013), pp. 6–15.

[150] V. Sortur et al. "Vibrational assignments for 7-methyl-4-bromomethylcoumarin, as aided by RHF and B3LYP/6-31G* calculations". In: *Spectrochimica Acta Part A: Molecular and Biomolecular Spectroscopy* 71.2 (2008), pp. 688–694.

[151] H. Luo et al. "Surface-enhanced Raman spectroscopy coupled with gold nanoparticles for rapid detection of phosmet and thiabendazole residues in apples". In: *Food Control* 68 (2016), pp. 229–235.

[152] J. M. Caridad et al. "Hot-volumes as uniform and reproducible sers-detection enhancers in weakly-coupled metallic nanohelices". In: *Scientific reports* 7 (2017), p. 45548.

[153] C. Wang et al. "Orientation-dependent nanostructure arrays based on anisotropic silicon wet-etching for repeatable surface-enhanced Raman scattering". In: *Nanoscale* 8.8 (2016), pp. 4672–4680.

[154] H.-Y. Chen et al. "Large-scale hot spot engineering for quantitative SERS at the single-molecule scale". In: *Journal of the American Chemical Society* 137.42 (2015), pp. 13698–13705.

[155] J.-A. Huang et al. "Ordered Ag/Si nanowires array: wide-range surface-enhanced Raman spectroscopy for reproducible biomolecule detection". In: *Nano letters* 13.11 (2013), pp. 5039–5045.

[156] Q. Fu et al. "Highly reproducible and sensitive SERS substrates with Ag inter-nanoparticle gaps of 5 nm fabricated by ultrathin aluminum mask technique". In: *ACS applied materials & interfaces* 7.24 (2015), pp. 13322–13328.

[157] V. Peksa et al. "Testing gold nanostructures fabricated by hole-mask colloidal lithography as potential substrates for SERS sensors: sensitivity, signal variability, and the aspect of adsorbate deposition". In: *Physical Chemistry Chemical Physics* 18.29 (2016), pp. 19613–19620.

[158] A. K. Jamil et al. "A homogeneous surface-enhanced Raman scattering platform for ultra-trace detection of trinitrotoluene in the environment". In: *Analytical Methods* 7.9 (2015), pp. 3863–3868.

[159] C. Novara et al. "SERS-active Ag nanoparticles on porous silicon and PDMS substrates: a comparative study of uniformity and Raman efficiency". In: *The Journal of Physical Chemistry C* 120.30 (2016), pp. 16946–16953.

[160] Z. Luo et al. "Net-like assembly of Au nanoparticles as a highly active substrate for surface-enhanced Raman and infrared spectroscopy". In: *The Journal of Physical Chemistry A* 113.11 (2009), pp. 2467–2472.

[161] G. Aprile et al. "Toward Lateral Length Standards at the Nanoscale Based on Diblock Copolymers". In: *ACS applied materials & interfaces* 9.18 (2017), pp. 15685–15697.

[162] Y. S. Hu et al. "Enhanced raman scattering from nanoparticle-decorated nanocone substrates: A practical approach to harness in-plane excitation". In: *Acs Nano* 4.10 (2010), pp. 5721–5730.

[163] B. Beckhoff. "Reference-free X-ray spectrometry based on metrology using synchrotron radiation". In: *Journal of Analytical Atomic Spectrometry* 23.6 (2008), pp. 845–853.

[164] F. Scholze and M. Procop. "Modelling the response function of energy dispersive X-ray spectrometers with silicon detectors". In: *X-Ray Spectrometry: An International Journal* 38.4 (2009), pp. 312–321.

[165] T. Schoonjans et al. "The xraylib library for X-ray–matter interactions. Recent developments". In: *Spectrochimica Acta Part B: Atomic Spectroscopy* 66.11-12 (2011), pp. 776–784.

[166] M. E. Wieser et al. "Atomic weights of the elements 2011 (IUPAC Technical Report)". In: *Pure and Applied Chemistry* 85.5 (2013), pp. 1047–1078.

[167] Y. Liu et al. "Recent developments in the detection of melamine". In: *Journal of Zhejiang University Science B* 13.7 (2012), pp. 525–532.

[168] B. M. Kuehn. "Melamine scandals highlight hazards of increasingly globalized food chain". In: *JAMA* 301.5 (2009), pp. 473–475.

[169] J. F. E. C. on Food Additives. Meeting and W. H. Organization. *Evaluation of Certain Food Additives: Seventy-first Report of the Joint FAO/WHO Expert Committee on Food Additives*. Vol. 71. World Health Organization, 2010.

[170] V. Barwick and E. Prichard. "Eurachem guide: Terminology in analytical measurement - Introduction to VIM 3". In: 31 (2011).

[171] C.-C. Liu et al. "Directed self-assembly of block copolymers for 7 nanometre FinFET technology and beyond". In: *Nature Electronics* 1.10 (2018), p. 562.

[172] M. P. Stoykovich et al. "Directed assembly of block copolymer blends into nonregular device-oriented structures". In: *Science* 308.5727 (2005), pp. 1442–1446.

[173] L. Wan et al. "The limits of lamellae-forming PS-b-PMMA block copolymers for lithography". In: *ACS nano* 9.7 (2015), pp. 7506–7514.

[174] G. Liu et al. "Integration of Density Multiplication in the Formation of Device-Oriented Structures by Directed Assembly of Block Copolymer–Homopolymer Blends". In: *Advanced Functional Materials* 20.8 (2010), pp. 1251–1257.

[175] F. Ferrarese Lupi et al. "Hierarchical Order in Dewetted Block Copolymer Thin Films on Chemically Patterned Surfaces". In: *ACS nano* 12.7 (2018), pp. 7076–7085.

[176] M. Perego et al. "Collective behavior of block copolymer thin films within periodic topographical structures". In: *Nanotechnology* 24.24 (2013), p. 245301.

[177] M. Grzelczak et al. "Directed self-assembly of nanoparticles". In: *ACS nano* 4.7 (2010), pp. 3591–3605.

[178] Y. Yin et al. "Template-assisted self-assembly: a practical route to complex aggregates of monodispersed colloids with well-defined sizes, shapes, and structures". In: *Journal of the American Chemical Society* 123.36 (2001), pp. 8718–8729.

[179] C. López. "Materials aspects of photonic crystals". In: *Advanced Materials* 15.20 (2003), pp. 1679–1704.

[180] J. H. Holtz and S. A. Asher. "Polymerized colloidal crystal hydrogel films as intelligent chemical sensing materials". In: *Nature* 389.6653 (1997), p. 829.

[181] I. Gourevich et al. "Multidye nanostructured material for optical data storage and security labeling". In: *Chemistry of materials* 16.8 (2004), pp. 1472–1479.

[182] Y. Huang et al. "Directed assembly of one-dimensional nanostructures into functional networks". In: *Science* 291.5504 (2001), pp. 630–633.

[183] M. Rycenga, P. H. Camargo, and Y. Xia. "Template-assisted self-assembly: a versatile approach to complex micro-and nanostructures". In: *Soft Matter* 5.6 (2009), pp. 1129–1136.

[184] Y. Xia et al. "Template-assisted self-assembly of spherical colloids into complex and controllable structures". In: *Advanced Functional Materials* 13.12 (2003), pp. 907–918.

[185] B. Varghese et al. "Size selective assembly of colloidal particles on a template by directed self-assembly technique". In: *Langmuir* 22.19 (2006), pp. 8248–8252.

[186] Y. Xia et al. "Monodispersed colloidal spheres: old materials with new applications". In: *Advanced Materials* 12.10 (2000), pp. 693–713.

[187] S. O. Kim et al. "Epitaxial self-assembly of block copolymers on lithographically defined nanopatterned substrates". In: *Nature* 424.6947 (2003), p. 411.

[188] M. Perego et al. "Collective behavior of block copolymer thin films within periodic topographical structures". In: *Nanotechnology* 24.24 (2013), p. 245301.

[189] S.-J. Jeong et al. "Soft graphoepitaxy of block copolymer assembly with disposable photoresist confinement". In: *Nano letters* 9.6 (2009), pp. 2300–2305.

[190] P. A. Kralchevsky and N. D. Denkov. "Capillary forces and structuring in layers of colloid particles". In: *Current opinion in colloid & interface science* 6.4 (2001), pp. 383–401.

[191] K. R. Strehle et al. "A reproducible surface-enhanced Raman spectroscopy approach. Online SERS measurements in a segmented microfluidic system". In: *Analytical chemistry* 79.4 (2007), pp. 1542–1547.

[192] K. Brassat et al. "Self-organization of nanospheres in trenches on silicon surfaces". In: *Physica Status Solidi (A)* 210.8 (2013), pp. 1485–1489.

[193] B. T. Draine and P. J. Flatau. "Discrete-dipole approximation for scattering calculations". In: *JOSA A* 11.4 (1994), pp. 1491–1499.

[194] Z. Yang et al. "FDTD for plasmonics: Applications in enhanced Raman spectroscopy". In: *Chinese Science Bulletin* 55.24 (2010), pp. 2635–2642.

[195] S. Monti, V. Carravetta, and H. Ågren. "Simulation of gold functionalization with cysteine by reactive molecular dynamics". In: *The journal of physical chemistry letters* 7.2 (2016), pp. 272–276.

Index

This Ph.D. thesis has been typeset by means of the TEX-system facilities. The typesetting engine was pdfLATEX. The document class was `toptesi`, by Claudio Beccari, with option `tipotesi=scudo`. This class is available in every up-to-date and complete TEX-system installation.